

**PRECISION INTERFEROMETRY IN A NEW SHAPE:  
HIGHER-ORDER LAGUERRE-GAUSS MODES FOR  
GRAVITATIONAL WAVE DETECTION**

by  
**PAUL FULDA**

A thesis submitted to the  
University of Birmingham  
for the degree of  
**DOCTOR OF PHILOSOPHY**

**Astrophysics and Space Research Group  
School of Physics and Astronomy  
College of Engineering and Physical Sciences  
University of Birmingham  
June 2012**

UNIVERSITY OF  
BIRMINGHAM

**University of Birmingham Research Archive**

**e-theses repository**

This unpublished thesis/dissertation is copyright of the author and/or third parties. The intellectual property rights of the author or third parties in respect of this work are as defined by The Copyright Designs and Patents Act 1988 or as modified by any successor legislation.

Any use made of information contained in this thesis/dissertation must be in accordance with that legislation and must be properly acknowledged. Further distribution or reproduction in any format is prohibited without the permission of the copyright holder.

## Abstract

The sensitivity of the next generation of interferometric gravitational wave detectors will be limited in part by thermal noises of the optics. It has been proposed that using higher-order Laguerre-Gauss (LG) beams in the interferometers can reduce this noise [MTV06]. This thesis documents the progress made in assessing the compatibility of higher-order LG beam technology with the existing precision interferometry framework used in the gravitational wave detector community.

A numerical study into the interferometric performance of the LG<sub>33</sub> mode [CHF09] showed that the LG<sub>33</sub> mode is compatible with the Pound-Drever-Hall (PDH) longitudinal control scheme [DHK<sup>+</sup>83], and the Ward technique for alignment control [MRWM94a]. A sensitivity study was performed for the LG<sub>33</sub> mode in an Advanced-Virgo-like detector, with the result that the LG<sub>33</sub> mode could offer a potential increase in the observed gravitational wave event rate by over a factor of 2.

A numerical investigation was made into techniques for generating higher-order LG modes with a phase modulating surface. The optimal conditions for mode conversion were determined using fast Fourier transform (FFT) simulations, and predictions were made for the mode purity achievable with this method.

Table-top experiments performed at Birmingham demonstrated the generation of higher-order LG modes using a spatial light modulator, and showed for the first time the feedback control of an optical cavity on resonance for higher-order LG modes. An increase in the purity of LG<sub>33</sub> modes from 51 % to over 99 % upon transmission through a mode cleaner cavity was shown. The incompatibility of helical LG modes with three-mirror optical cavities was also experimentally demonstrated.

Investigations were carried out at the Glasgow 10 m prototype detector into the performance of the LG<sub>33</sub> mode in a suspended 10 m cavity. This work has provided useful insights into the compatibility of LG modes with larger scale interferometer systems, highlighting the issue of LG mode degeneracy within high-finesse cavities. This remains the main difficulty to be overcome before the LG mode technology can be implemented in full scale detectors.

## Statement of originality

This thesis represents research work carried out at the University of Birmingham between September 2008 and June 2012.

**Chapter 1** gives an introduction to the topic of gravitational wave detection. This includes a brief description of the theoretical basis for gravitational waves, a short history of gravitational wave detection experiments, a description of some of the leading interferometric gravitational wave detectors, and the principal noise sources that limit their sensitivity.

**Chapter 2** provides an explanation of the technique of using higher-order laser modes to reduce the levels of test mass thermal noise in gravitational wave detectors. This includes an overview of the relevant test mass thermal noise processes, a description of Laguerre-Gauss (LG) modes and Hermite-Gauss (HG) modes, and the noise reduction factors for a range of LG and HG modes.

**Chapter 3** describes the results of simulation investigations into the use of higher-order LG modes in gravitational wave interferometers. The first section of this chapter describes simulation work led by Simon Chelkowski at the University of Birmingham, using the interferometer simulation software FINESSE [FHL<sup>+</sup>04] to investigate the interferometric performance of LG modes in gravitational wave detectors. Many of the results shown in this section are also presented in

S. Chelkowski, S. Hild and A. Freise, *Prospects of higher-order Laguerre-Gauss modes in future gravitational wave detectors*, Physical Review D, **79**(12):122002, (2009).

Although I was not directly involved in this work, much of the work described in chapter 4 was aimed at experimentally verifying the results of these simulations. As a result I have reproduced several of the results, and become very familiar with the simulation code used. The code is included in the appendix B.1.

The second section of this chapter describes simulations investigating the means of LG mode generation by interaction with a phase modulating surface. I wrote several scripts and functions in Matlab to produce these results, some of which are included in the appendix B.2. The phase profiles that I designed during this work were used to produce higher-order LG modes using a spatial light modulator, as described in chapter 4.

**Chapter 4** reports on the work that I led and carried out in table-top laboratory

---

investigations of LG mode interferometry. This work included the first demonstration of an optical cavity feedback controlled for resonance of higher-order LG modes, as well as a demonstration of the decomposition of a helical LG<sub>33</sub> mode into two sinusoidal LG<sub>33</sub> modes by interaction with a triangular optical cavity. The main results of the work described in this chapter were published in

P. Fulda, K. Kokeyama, S. Chelkowski, A. Freise, *Experimental demonstration of higher-order Laguerre-Gauss mode interferometry*, Physical Review D, **82**(1):012002, (2010).

**Chapter 5** describes the work carried out towards a demonstration of LG<sub>33</sub> mode technology at the Glasgow 10 m gravitational wave detector prototype. The first section explains the crucial issue of higher-order LG mode degeneracy in optical cavities, which we aimed to investigate with the prototype experiments. The results of simulation work into the mode degeneracy issue in which I was involved, but which was led by Charlotte Bond, are briefly reported in this section, and more fully in

C. Bond, P. Fulda, L. Carbone, K. Kokeyama, A. Freise, *Higher-order Laguerre-Gauss mode degeneracy in realistic, high finesse cavities*, Physical Review D, **84**(10):102002, (2011).

Section two of this chapter describes the design of the etched diffractive optic used for generation of LG<sub>33</sub> modes for the prototype experiment, as well as for the high-power LG mode experiments recently carried out at the AEI in Hanover. These designs were made in collaboration between myself and the company Jenoptik.

Section three of this chapter describes the LG<sub>33</sub> mode generation optical path that I designed and installed for the experiments at the 10 m prototype in Glasgow.

Section four reports on the methods and results of the investigation into the performance of the LG<sub>33</sub> mode in a 10 m suspended optical cavity at the Glasgow prototype. This work was performed in a collaboration between members of the interferometry groups in the University of Birmingham and Glasgow University. I was heavily involved from both sides, spending several weeks at the facility in Glasgow, as well as assisting in simulation efforts from Birmingham. The work described here is also reported in a paper recently submitted for publication by Borja Sorazu.

**Appendix A** consists of reduction factors for higher-order modes test-mass thermal noises other than coating Brownian noise. The bulk of the calculations are from references [Vin09] and [Vin10], but are presented here after scaling to account for the

---

different clipping losses associated with each mode.

**Appendix B** consists of the FINESSE master input file written initially by Simon Chelkowski for producing many of the plots shown in the first section of chapter 3, as well as the Matlab scripts and functions written by myself and others for producing the results shown in the second section of chapter 3.

# Contents

<b>Abstract</b>	<b>i</b>
<b>Statement of originality</b>	<b>ii</b>
<b>Table of Contents</b>	<b>v</b>
<b>List of Figures</b>	<b>ix</b>
<b>List of Tables</b>	<b>xiii</b>
<b>Glossary</b>	<b>xv</b>
<b>1. Introduction</b>	<b>1</b>
1.1. Project background . . . . .	1
1.2. Gravitational wave theory . . . . .	2
1.3. History of gravitational wave detection . . . . .	4
1.4. Michelson interferometer type gravitational wave detectors . . . . .	6
1.5. Noise sources in interferometric gravitational wave detectors . . . . .	8
1.6. First generation ground-based gravitational wave detectors . . . . .	11
1.7. Second generation ground-based detectors . . . . .	13
1.8. Future gravitational wave detectors . . . . .	15
1.9. Structure of this thesis . . . . .	15
<b>2. Laguerre-Gauss beams for test mass thermal noise reduction</b>	<b>17</b>
2.1. Test mass thermal noise . . . . .	17
2.2. Thermal noise reduction techniques . . . . .	22
2.3. The mode picture for laser beams . . . . .	25
2.4. The Hermite-Gauss mode set . . . . .	28
2.5. The Laguerre-Gauss mode sets . . . . .	29

2.6.	Reduction in thermal noise for higher-order LG beams . . . . .	34
2.7.	Coating Brownian thermal noise reduction factors for higher-order modes	36
2.7.1.	Helical Laguerre-Gauss modes . . . . .	36
2.7.2.	Hermite-Gauss modes . . . . .	39
2.8.	Thermal lensing . . . . .	40
<b>3.</b>	<b>Simulation study into LG<sub>33</sub> mode interferometry and production</b>	<b>43</b>
3.1.	Interferometric performance simulation study of the LG <sub>33</sub> mode . . . . .	44
3.1.1.	Longitudinal control signals . . . . .	45
3.1.2.	Alignment control signals . . . . .	46
3.1.3.	Coupling of cavity mirror tilt to longitudinal phase . . . . .	50
3.1.4.	Coupling of differential arm cavity misalignment to dark port power	51
3.1.5.	Coupling to unwanted modes due mode mismatch . . . . .	53
3.1.6.	Sensitivity improvements for Advanced Virgo . . . . .	55
3.2.	Numerical investigation into LG <sub>33</sub> beam generation by LG <sub>00</sub> phase profile modulation . . . . .	56
3.2.1.	Overview of previous work in Laguerre-Gauss beam production .	57
3.2.2.	Phase modulation profile design . . . . .	57
3.2.3.	Simulations of conversion from LG <sub>00</sub> beam to a LG <sub>33</sub> beam . . .	61
3.2.4.	Converted beam parameter estimation . . . . .	62
3.2.5.	Optimum conversion beam size ratio . . . . .	67
3.2.6.	Theoretical purities of generated LG modes . . . . .	69
<b>4.</b>	<b>Tabletop demonstrations of LG mode production and cleaning</b>	<b>73</b>
4.1.	Characterising the spatial light modulator . . . . .	74
4.2.	Higher-order LG modes generated using a spatial light modulator . . . .	79
4.2.1.	Mode conversion results . . . . .	79
4.2.2.	Blazing angle tests . . . . .	84
4.3.	Mode cleaning higher-order LG modes . . . . .	85
4.3.1.	The mode cleaner effect . . . . .	86
4.3.2.	Design and characterisation of the triangular and linear mode cleaners . . . . .	89
4.3.3.	Operation of the linear mode cleaner with higher-order LG modes	92
4.4.	Helical LG mode interaction with a 3-mirror cavity . . . . .	103

<b>5. Prototype experiments with the LG<sub>33</sub> mode</b>	<b>109</b>
5.1. Degeneracy of higher-order Laguerre-Gauss modes . . . . .	110
5.2. Design and manufacture of an etched diffractive optic for mode conversion	112
5.3. LG <sub>33</sub> conversion bench at the Glasgow 10 m prototype . . . . .	114
5.4. 10 m cavity performance with the LG <sub>33</sub> mode . . . . .	118
<b>6. Summary and conclusions</b>	<b>127</b>
6.1. Summary . . . . .	127
6.2. Conclusions and outlook . . . . .	128
<b>A. Thermal noise scaling factors for higher-order modes</b>	<b>131</b>
A.1. Laguerre-Gauss mode thermal noise scaling factors . . . . .	131
A.2. Hermite-Gauss mode thermal noise scaling factors . . . . .	133
<b>B. Simulation code for results presented in chapter 3</b>	<b>137</b>
B.1. FINESSE input files . . . . .	137
B.2. Matlab FFT scripts . . . . .	147
<b>Bibliography</b>	<b>165</b>
<b>Acknowledgments</b>	<b>175</b>



# List of Figures

1.1. The influence of both + and $\times$ polarisation gravitational waves on a ring of test mass particles. . . . .	3
1.2. The influence of both + and $\times$ polarisation gravitational waves on a Michelson interferometer . . . . .	7
1.3. Three different optical layouts for Michelson type gravitational wave detectors . . . . .	12
2.1. Advanced LIGO projected sensitivity curves . . . . .	19
2.2. A cartoon picture of an optical cavity . . . . .	25
2.3. Intensity patterns for Hermite-Gauss modes up the order 6. The intensity patterns are normalised to have the same peak intensity, for visibility. . . . .	29
2.4. Amplitude cross sections of a HG <sub>00</sub> mode, a HG <sub>10</sub> mode, and the sum of both. . . . .	30
2.5. Intensity patterns for helical LG modes up to order 9. . . . .	31
2.6. Intensity patterns for sinusoidal LG modes up to order 9. . . . .	32
2.7. Amplitude cross sections of a LG <sub>00</sub> mode, a LG <sub>10</sub> mode, and the sum of both. . . . .	33
2.8. LG <sub>00</sub> mode and LG <sub>33</sub> radial intensity profile comparison. . . . .	35
3.1. PDH longitudinal error signals for a 3 km cavity. . . . .	46
3.2. Two optical layouts used in the alignment analysis simulations. . . . .	47
3.3. Alignment error signals for a 3 km cavity. . . . .	48
3.4. Coupling mechanism between misalignment and longitudinal phase in a plane-concave cavity. . . . .	51
3.5. Intra cavity power as a function of cavity end mirror tilt angle $\beta$ and longitudinal tuning $\phi$ . . . . .	52
3.6. Dark port power as a function of differential arm cavity misalignment. . . . .	53
3.7. Coupling of beam waist size mismatch to power in different mode orders. . . . .	54

3.8. Two phase modulation profiles to convert a $LG_{00}$ mode to a cosine $LG_{33}$ mode and a helical $LG_{33}$ mode . . . . .	58
3.9. Example of blazed phase modulation profiles for generating sinusoidal and helical $LG_{33}$ modes. . . . .	59
3.10. Example of amplitude contoured blazed phase modulation profiles for generating sinusoidal and helical $LG_{33}$ modes. . . . .	60
3.11. Intensity and phase profiles of an ideal helical $LG_{33}$ mode and a helical $LG_{33}$ mode generated by interaction of a $LG_{00}$ with the phase modulation profile shown in figure 3.8. . . . .	62
3.12. Normalised amplitude and intensity for cross sections through the optic axis of the simulated converted $LG_{33}$ beam and the ideal $LG_{33}$ beam. . .	63
3.13. Comparison between theoretical and numerical results for post-phase modulation profile interaction beam parameters. . . . .	68
3.14. Simulated converted $LG_{33}$ mode purity as a function of the ratio between input $LG_{00}$ beam size and $LG_{33}$ phase modulation profile beam size. . .	69
3.15. Amplitude transmission masks for the sinusoidal and helical $LG_{33}$ modes. . . . .	70
4.1. Holoeye LCR-2500 liquid crystal on silicon spatial light modulator . . .	74
4.2. Optical layout for characterising the SLM . . . . .	75
4.3. Measured fringe pattern from the setup shown in figure 4.2. . . . .	76
4.4. Fitting results for the left and right sides of the CCD image shown in figure 4.3. . . . .	77
4.5. Phase modulation from the LCR-2500 SLM as a function of applied greyscale value. . . . .	78
4.6. Initial setup for generating and observing LG modes with the SLM. . .	79
4.7. Helical LG modes up to $LG_{33}$ , as generated using the SLM without and with amplitude contouring. . . . .	81
4.8. Setup for measuring the interference between SLM generated LG modes and the $LG_{00}$ mode. . . . .	82
4.9. Measured $LG_{33}$ mode interferograms, compared with simulations. . . . .	83
4.10. Phase modulation profiles and the corresponding diffraction patterns. . .	85
4.11. Results of a FINESSE simulation for a mode cleaner cavity. . . . .	88
4.12. Photograph of the linear mode cleaner cavity. . . . .	90
4.13. Triangular mode cleaner cavity scan. . . . .	91
4.14. Calibration curve for the triangular mode cleaner PZT . . . . .	92

4.15. Triangular mode cleaner scan after compensation for the non-linearity of the PZT . . . . .	93
4.16. Non-linear fitting results for the calibrated scan data. . . . .	94
4.17. Experimental layout for the LG mode conversion and cleaning path. . .	95
4.18. Photograph of the LG mode conversion and cleaning setup. . . . .	96
4.19. Comparison between theoretical and measured length error signal for the LG <sub>33</sub> mode in the linear mode cleaner. . . . .	97
4.20. Intensity profiles of LG <sub>33</sub> beams input to and transmitted through the linear mode cleaner. . . . .	98
4.21. Residuals from best fits between three intensity profiles and a theoretically ideal sinusoidal LG <sub>33</sub> intensity pattern. . . . .	100
4.22. Higher-order sinusoidal and helical LG modes transmitted through a linear mode cleaner . . . . .	103
4.23. Interferogram of the LG <sub>33</sub> mode transmitted through a linear mode cleaner.	104
4.24. Transverse phase distributions of the helical, vertically symmetric sinusoidal and vertically anti-symmetric sinusoidal LG <sub>33</sub> modes. . . . .	105
4.25. Triangular mode cleaner scans with helical and vertically symmetric sinusoidal LG <sub>33</sub> input beams. . . . .	106
4.26. Experimental setup for investigating the interaction of a helical LG <sub>33</sub> mode with a triangular mode cleaner. . . . .	107
5.1. Schematic of the laser mode conversion path on the Glasgow 10 m prototype input optics bench. . . . .	115
5.2. Photograph of the laser mode conversion path on the Glasgow 10 m prototype input optics bench. . . . .	116
5.3. Data points and fit for the beam waist size and position of the LG <sub>33</sub> after the linear mode cleaner. . . . .	117
5.4. Images of the LG <sub>33</sub> beam along the path before entering the 10 m cavity.	122
5.5. Scans of the 10 m cavity with the LG <sub>00</sub> mode and the LG <sub>33</sub> mode. . . .	123
5.6. A closer look at the dominant peaks in the cavity scans shown in figure 5.5.	124
5.7. The dominant peaks of four successive FSRs of the 10 m cavity when scanned with the LG <sub>33</sub> mode. . . . .	125
5.8. Mode shapes recorded with the high-speed camera, overlaid on the split LG mode resonance peak. . . . .	125
5.9. Astigmatic cavity simulations with four different cavity input modes. . .	126



# List of Tables

2.1. Coating Brownian noise scaling factors for $LG_{pl}$ modes. . . . .	37
2.2. Beam size scaling factors for $LG_{pl}$ modes. . . . .	38
2.3. Coating Brownian noise power spectral density improvement factors for $LG_{pl}$ modes. . . . .	38
2.4. Beam size scaling factors for HG modes. . . . .	39
2.5. Coating Brownian noise power spectral density improvement factors for $HG_{nm}$ modes. . . . .	40
3.1. Cavity parameters for each of the three different configurations used in the $LG_{33}$ interferometric performance simulation study. . . . .	45
3.2. Results of the GWINC calculation for detection ranges of two standard gravitational wave sources with the Advanced Virgo reference design. . .	55
3.3. Optimum ratio between input $LG_{00}$ beam size and $LG_{pl}$ phase image beam size, for LG modes up to the order 9. . . . .	70
4.1. Cavity parameters for some gravitational wave detector input mode cleaners, as well as for cavities used in this work. . . . .	89
4.2. Mode decomposition of the numerical model of the sinusoidal $LG_{33}$ beam transmitted through the linear mode cleaner. . . . .	101
4.3. Purities of the generated $LG_{33}$ modes, and efficiencies of the SLM $LG_{33}$ mode conversion process. . . . .	102
5.1. Design specifications for the DOE used on the LG mode conversion bench at the Glasgow 10 m prototype. . . . .	113
5.2. Table showing the power present in LG modes of order 9 in the simulation of DOE $LG_{33}$ conversion, for three different off axis designs. . . . .	114
5.3. Relevant parameters of the 10 m suspended cavity in Glasgow. . . . .	118

*List of Tables*

---

A.1. Substrate Brownian noise power spectral density improvement factors for LG <sub>pl</sub> modes. . . . .	132
A.2. Substrate thermoelastic noise power spectral density improvement factors for LG <sub>pl</sub> modes. . . . .	133
A.3. Substrate Brownian noise power spectral density improvement factors for HG <sub>nm</sub> modes. . . . .	134
A.4. Substrate thermoelastic noise power spectral density improvement factors for HG <sub>nm</sub> modes. . . . .	135

## Glossary

<b>CCD</b>	Charge coupled device
<b>DOE</b>	Diffractive optical element
<b>EOM</b>	Electro-optic modulator
<b>FDT</b>	Fluctuation dissipation theorem
<b>FFT</b>	Fast-Fourier transform
<b>FSR</b>	Free spectral range
<b>FWHM</b>	Full width half maximum
<b>HG</b>	Hermite-Gauss
<b>IMC</b>	Input mode cleaner
<b>LG</b>	Laguerre-Gauss
<b>LMC</b>	Linear mode cleaner
<b>PDH</b>	Pound-Drever-Hall
<b>PZT</b>	Piezoelectric transducer
<b>QPD</b>	Quadrant photodetector
<b>RF</b>	Radio Frequency
<b>SLM</b>	Spatial light modulator
<b>TMC</b>	Triangular mode cleaner



# Chapter 1.

## Introduction

### 1.1. Project background

Highly sensitive laser interferometers are currently at the forefront of the scientific field of gravitational wave detection. Despite being extremely low noise instruments, these interferometers are yet to reach the sensitivity required to reliably make gravitational wave detections. Several limiting noise sources have been identified, and much of the work in the field of gravitational wave detection goes into reducing their effects. Thermal noise of the interferometer test masses is expected to be a limiting noise source in future detectors, unless new techniques are used to reduce this noise. Presented in this report is an investigation into a new method for reducing the level of thermal noise in ground-based interferometric gravitational wave detectors using higher-order Laguerre-Gauss (LG) beam shapes in place of the heretofore used fundamental Gaussian beam [MTV06].

There is great scientific interest in detecting gravitational waves for two main reasons. The first of these is that the existence of gravitational waves remains an unverified prediction of Einstein's theory of General Relativity, and thus to prove their existence would be another confirmation of the adequacy of the theory as a model for spacetime. The second reason is that information from astrophysical gravitational wave sources is likely to be very valuable in the fields of astronomy and cosmology. The development of gravitational wave astronomy in the foreseeable future would open up a whole new spectrum for observation, and thus give astronomers and cosmologists another vital tool for distinguishing between competing theories on the nature of the universe.

The nature of gravitational waves is such that they interact very weakly with matter; an advantageous property for astronomy in that it means gravitational wave signals

from distant objects are not absorbed or scattered to the extent that electromagnetic signals are. Gravitational waves therefore carry well preserved information about their sources [MTW73]. The weak nature of gravitational waves unfortunately also makes them very difficult to detect directly. Although no conclusive direct detections of gravitational waves have been made, indirect evidence for their existence was discovered by R. A. Hulse and J. H. Taylor in their 1975 Nobel Prize winning paper [HT75]. In this paper they described the shortening orbital period of a binary neutron star system, and concluded that the shortening of the period was due to the radiation of energy from the system in the form of gravitational waves. The rate of decrease of the orbital period due to gravitational radiation which was predicted by Einstein's theory of General Relativity was found to closely match that observed by Hulse and Taylor. These results provide strong evidence for the existence of gravitational waves, yet direct detections remain elusive.

A number of so called 'first generation' interferometric ground-based detectors have already been built and have recorded data. To this date the sensitivity of all these detectors has been limited to the extent that they have not conclusively detected gravitational waves. Groups around the world are working on ways to increase the sensitivity of gravitational wave detectors in order to make the first conclusive gravitational wave detection. The long term aim in the field is to build detectors that are capable of acting as gravitational wave observatories. Such observatories could in the future be used to greatly increase our knowledge about the structure and formation history of the universe and the astrophysical objects which inhabit it.

## 1.2. Gravitational wave theory

This section is by no means intended as a treatise on gravitational wave theory, but merely as a basic introduction to the concepts involved. For a more in depth description of gravitational wave theory, I would point the interested reader towards [Sau94]. Gravitational waves are often described as ripples in spacetime created by accelerating masses, and are wave-like solutions to Einstein's field equations. Their existence solves the problem of causality that Sir Isaac Newton identified in his own theory of gravitation; that gravitational information cannot be instantaneously transferred across the universe, but must travel at the speed of light.

Using Einstein's field equations from General Relativity, it is possible to predict the amplitude, polarisation and frequency of gravitational waves emitted by a range of astrophysical sources [CT02]. These include sources such as compact binary star systems, black hole and neutron star coalescences, and supernova explosions [Fin96, ZM97]. The generation mechanism of gravitational waves is quadrupole in nature. This fact, combined with the weakness of the gravitational force, means that the amplitude of gravitational waves is expected to be very small.

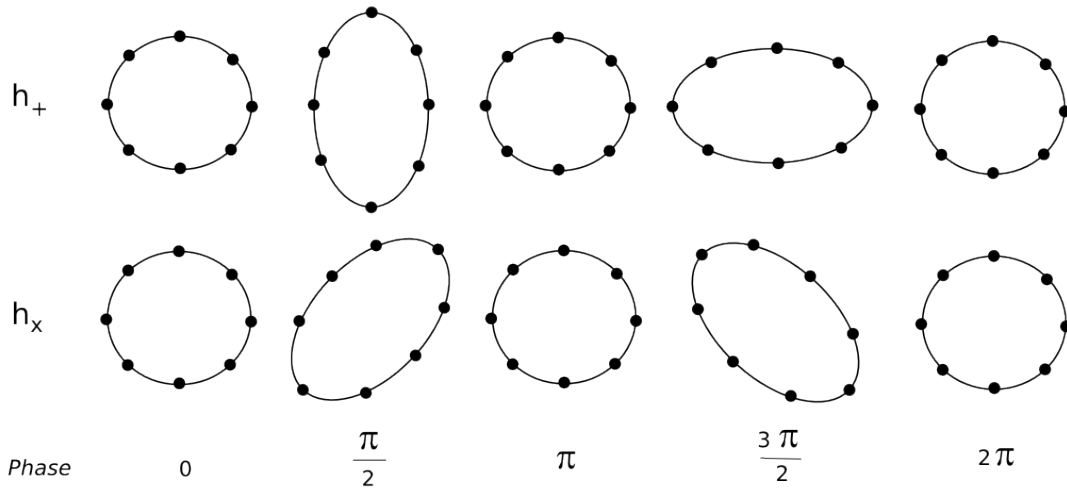


Figure 1.1.: The influence of both + and x polarisation gravitational waves on ring of test mass particles. The incident gravitational wave is travelling perpendicular to the plane of the ring of test mass particles.

The gravitational wave amplitude, often referred to as the strain in spacetime,  $h$ , that is observed at a distance  $r$  away from a source, is given by

$$h(r) = \frac{2G}{c^4} \frac{1}{r} \frac{d^2 I}{dt^2}, \quad (1.1)$$

where  $G$  is the gravitational constant,  $c$  is the speed of light in a vacuum and  $I$  is the quadrupole moment of the source. The second time derivative of the quadrupole moment can be thought of as an asymmetric acceleration term. From this equation it can be seen that the amplitude of gravitational waves is likely to be small due to the factor  $\frac{G}{c^4}$ . Even for large scale cosmic events such as supernovae, the predicted amplitude of gravitational waves at the Earth is extremely small. The influence of a gravitational

wave of amplitude  $h$  on a region of spacetime is characterised by

$$h = \frac{\delta l}{l}, \tag{1.2}$$

where  $l$  is the proper distance between two spacetime events and  $\delta l$  is the change in this distance caused by the gravitational wave. From this expression it can be seen that for gravitational wave detectors which rely upon measuring an induced length change  $\delta l$ , it is preferable to have a large separation between any test masses in the detector so as to maximise the measurable effect.

Gravitational waves, like their electromagnetic counterparts, are expected to exist in a whole spectrum of frequencies. The frequency of gravitational waves is determined by the acceleration that generates them. For example, the frequency of gravitational waves emitted by two large masses orbiting one another is simply twice the frequency of the rotation [MTW73]. In the case of an inspiral binary system, such as the aforementioned Hulse-Taylor binary star system, the gravitational waves radiated increase in frequency as the period of the orbiting objects decreases. Gravitational waves are described by a linear combination of two orthogonal polarisations; + polarisation and  $\times$  polarisation. Figure 1.1 shows how gravitational waves of both polarisations interact with a ring of test mass particles.

### 1.3. History of gravitational wave detection

The history of experimental gravitational wave detection began in earnest in the late 1950s with Joseph Weber's development of a resonant bar detector. Resonant bar detectors are designed to work in a small frequency bandwidth by measuring resonant vibrations in a metal bar caused by passing gravitational waves [BM72]. Although Weber claimed to have detected a gravitational wave with his resonant bar detectors, the result was not accepted within the scientific community due to its lack of reproducibility. Subsequent designs of resonant bar detectors included the use of cryogenic cooling systems to reduce thermally induced excitations of the resonant modes of the bars and improve upon the sensitivity of the early detectors [SM04]. However, in recent years the scientific community has been more focussed on the development of interferometric gravitational wave detectors.

The design of interferometric gravitational wave detectors is based on the idea that

an interferometer can be used to measure the tiny changes in the separations of test masses that are caused by the influence of a gravitational wave. The first generation of ground-based interferometric detectors has been built and used to collect data in the latter part of the 1990s, and the 2000s. The most well known first generation detectors include the American LIGO detectors [BW99], the French-Italian detector Virgo [AAA<sup>+</sup>08], the German-British detector GEO600 [Hi106] and the Japanese detector TAMA300 [KKF<sup>+</sup>95]. These detectors were designed to detect gravitational waves in a band roughly equal to the audio frequency band; about 20 Hz to 20 kHz. However, the first generation of interferometric gravitational wave detectors were not sensitive enough at any frequencies to distinguish any possible gravitational wave signals from noise sources. The designs of the first generation interferometric detectors are described in section 1.6 of this report.

Work is currently under way towards upgrading some of the first generation detectors in a bid to increase their sensitivities by a factor of around 10 in the most sensitive frequency region. These upgraded detectors are known as second generation detectors, and will include Advanced LIGO [ABHK08], Advanced Virgo [FFG<sup>+</sup>05] and GEO-HF [WAA<sup>+</sup>06]. A new Japanese second generation detector called KAGRA is also currently under development [KLC06]. Much of the design of the second generation detectors is expected to be based around techniques developed for the GEO600 detector, which was able to achieve a high frequency sensitivity similar to LIGO despite its considerably shorter baseline length. Some of these new techniques are described in section 1.7 of this thesis.

The nature of gravitational wave detection is such that new techniques and technologies often take many years to refine and implement. This being the case, work has already begun on the third generation interferometric detector designs. The aspiration of the gravitational wave community is that by the end of the science runs of the second generation detectors, proposals which are now only in their earliest formative stages may be fully fledged designs for interferometric gravitational wave detectors that are capable of operating at sensitivities some 100 times that of the first generation detectors. The use of higher-order LG modes is one such new technology, and this thesis represents my work towards bringing this technology closer to a state of readiness for implementation in future gravitational wave detectors.

## 1.4. Michelson interferometer type gravitational wave detectors

There are currently a number of ground-based interferometric gravitational wave detectors that are either actively taking data, or have done so in the past. At present most of the currently favoured detectors use interferometric methods to detect the changes in the separations of test masses. All of the currently operating interferometric gravitational wave detectors are based on the Michelson interferometer design [MM87].

A Michelson interferometer has two main light paths. One path propagates through each of its two so called ‘arms’. Light from a laser is made incident upon a beam-splitter, which reflects half of the light along one arm while transmitting the rest of the light along the other arm. Mirrors are positioned at the ends of the two arms in order to reflect the light back to the beam-splitter. Light from both of the arms is then recombined at the beam-splitter, causing interference in accordance with the superposition principle. Some of the recombined light incident upon the beam-splitter propagates back towards the laser, and some propagates towards the output of the detector. How much light propagates in each of these directions is dependent upon the phase difference between the beams from the two arms of the detector.

A photodetector placed at the output of a Michelson interferometer can be used to measure the interference of the light from the two arms. The mirrors at the ends of the arms act as the test masses in Michelson type gravitational wave detectors, since any change in their positions causes a change in the interference at the beam-splitter which can then be measured at the output of the detector. Michelson type gravitational wave detectors are configured so that in the absence of any gravitational wave signal, the interference of light from both arms of the detector is destructive in the output port, resulting in all the light being reflected back towards the laser and none being observed at the photodetector.

According to the theory of General Relativity, a gravitational wave will cause a strain in the spacetime through which it passes, and in orthogonal directions these induced strains are 180 degrees out of phase. The result of this effect for a Michelson interferometer is that one arm increases in length while the other arm decreases in length, as depicted in figure 1.2. The differential length change of the two arms of a Michelson type gravitational wave detector which is caused by an incident gravitational wave results in

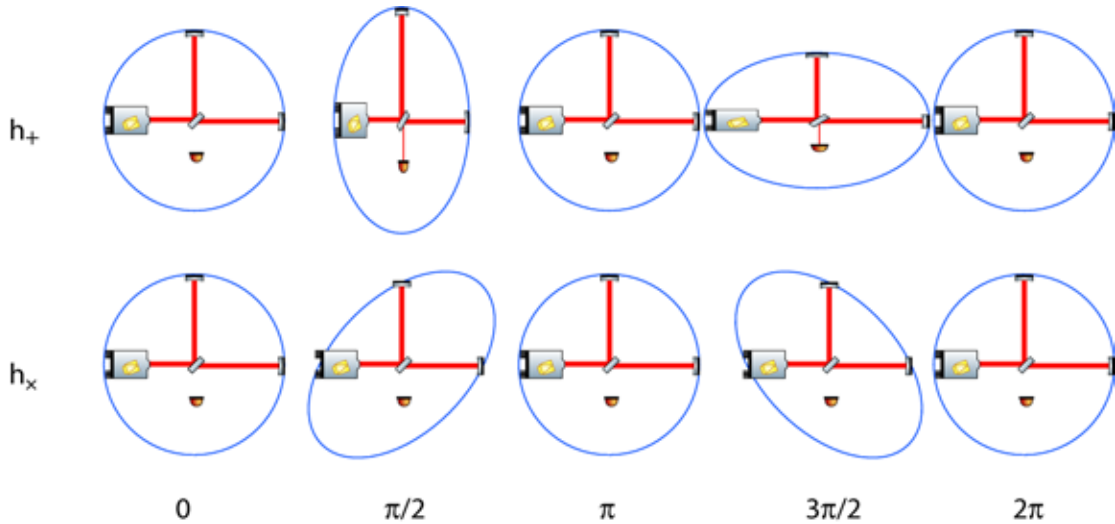


Figure 1.2.: The influence of both + and  $\times$  polarisation gravitational waves on a Michelson interferometer. The incident gravitational wave is travelling perpendicular to the plane of the interferometer arms. Note the insensitivity of the interferometer to the  $\times$  polarised gravitational wave. Image courtesy of S. Chelkowski.

a change of phase of the beams in both arms. The relative phase change between both arms,  $\delta\phi$ , which is caused by a change in arm length  $\delta l$  is given by

$$\delta\phi = \frac{4\pi}{\lambda} \delta l, \quad (1.3)$$

where  $\lambda$  is the wavelength of light in the interferometer. The relative phase change caused by a gravitational wave will cause a change in the interference at the beam-splitter, which will be observed as a change in the light intensity detected by the photodetector at the output port. It must be noted however that the strength of this effect is dependent upon the orientation of the polarisation vector of the gravitational wave relative to the arms, as well as the orientation of the gravitational wave propagation vector relative to the arms.

The change in spatial separation  $\delta l$  of two test masses caused by a gravitational wave is proportional to the proper distance between them,  $l$ . Thus it can be seen that for an interferometric detector which attempts to measure a  $\delta l$  caused by a gravitational wave, a large initial spatial separation of test masses (base-line) is advantageous. This is the reason why all of the first generation ground-based interferometric gravitational wave

detectors utilise such large base-lines, in two cases 4 km in length.

## 1.5. Noise sources in interferometric gravitational wave detectors

The reason that gravitational waves have not been reliably detected thus far is because of the difficulty associated with isolating detectors from noise sources. The expected strains induced at the Earth by gravitational waves from even the largest astrophysical sources are so small that detectors must be able to limit the strain equivalent noise in the observation band to  $10^{-22}$  or lower in order to reliably detect them. There are many noise sources which have to be considered in the design of ground-based interferometric gravitational wave detectors. A brief description of some of these is provided in this section.

### Seismic noise

Seismic noise originates from the vibrations that are ever present across the surface of the Earth. Disturbances in the ground position at the detector site can couple to the positions of the test masses, thus generating noise in the detector output. In order to minimise this coupling, the test masses are isolated from the ground motions by means of multi-stage pendulum suspensions such as described in [Goß04]. For the first generation of gravitational wave detectors, mechanically coupled seismic noise was the dominant noise contribution at frequencies below about 10 Hz. Seismic motion can also couple to noise in the interferometer gravitationally, an effect known as Newtonian noise, or gravity gradient noise [Sau84]. Though this coupling is typically much weaker than the mechanical coupling, there is no known effective way to isolate the test masses from it, so it is expected to become a more pressing concern in the design of future detectors.

### Shot noise

Shot noise originates from the quantum nature of light. It can be interpreted in many different ways, but most commonly it is understood as a photon counting noise. The total amount of energy transferred to a photodetector from an incident laser beam within

a given time is dependent upon the number of discrete photons that hit it during that time. There is a statistical fluctuation in the number of photons from a laser beam that will hit a photodetector in a given time, characterised by a Poissonian distribution. This statistical fluctuation is what produces the shot noise. The shot noise is proportional to  $\sqrt{P}$ , where  $P$  is the light power present in the arms of the interferometer. The signal intensity in laser interferometers, however, is proportional to  $P$ , and thus it can be seen that the signal to shot noise ratio can be improved by increasing the light power in the arms of the interferometer [Cav81].

### **Radiation pressure noise**

A well known outcome of the quantum nature of light is that photons carry momentum. When a photon is reflected from a mirror surface, this momentum is imparted to the mirror. The combined effect of many photons interacting with a mirror surface is known as the radiation pressure on the mirror. Due to the same statistical fluctuation in the number of photons interacting with a mirror as described for shot noise, this pressure also fluctuates statistically, thus leading to a fluctuation in the position of the mirror. This is currently not a limiting factor for the sensitivity of gravitational wave detectors. However, the level of radiation pressure noise increases with the intensity of light within the arms of an interferometer. Therefore in future detectors, which are expected to have circulating light powers some orders of magnitude larger than current detectors in order to reduce the effects of shot noise, radiation pressure noise may become a limiting noise source [Cav80]. Research is currently under way into possible ways in which the effects of radiation pressure can be used to amplify the signals created by a small bandwidth of gravitational waves within an interferometer. The use of so called ‘optical springs’ may even be incorporated into future detectors to increase their sensitivity within a certain bandwidth [HCC<sup>+</sup>03].

### **Thermal noise**

Thermal noise in interferometric gravitational wave detectors can be broadly separated into two categories; test mass thermal noise and suspension thermal noise. The dominant component of test mass thermal noise arises due to the Brownian motions of the molecules which make up the test masses and their reflective coatings. These vibrations

create an uncertainty in the position of the reflecting surfaces of the mirrors, and thus create a changing output signal from the detector which can obscure any gravitational wave signals. It is the reduction of test mass thermal noises in detectors that is the goal of this work; consequently a significant portion of chapter 2 is devoted to discussing this noise source in greater detail.

As previously mentioned, the core optics of all the leading gravitational wave interferometers are suspended in a manner such as to reduce the coupling of ground vibrations to the optics. The Advanced LIGO suspensions, for example, consist of multi-stage pendulums hung from blade-springs [CBB<sup>+</sup>12]. The pendulum reduces the coupling of horizontal ground vibrations to the optics, and the springs reduce coupling of vertical ground vibrations to the optics. Suspension thermal noise arises from the Brownian motion of the atoms within the suspension wires exciting the resonant modes of the suspension. At around 1 Hz, the frequencies of these resonant modes are typically below the detector observation band. However, if the suspension is lossy, some of the energy in the resonant modes dissipates and causes displacements at higher frequencies within the observation band.

The best way to reduce the effect of suspension thermal noise is to implement a suspension system with a very low mechanical dissipation (i.e. a very high Q-factor) as such a suspension confines the vibrations to a very narrow band near the resonant frequencies. The final stage of the Advanced LIGO test mass suspensions are made from monolithic fused-silica, due primarily to its high Q-factor. Losses in the suspension material are inevitable however, and these set the suspension thermal noise lower limit.

### **Technical noises**

In this context, technical noises include all non fundamental sources of noise in detectors, which in principle could be eliminated. Some main technical noise sources include laser amplitude and frequency noise, beam pointing or ‘jitter’ noise, and residual gas pressure noise. Fluctuations of the laser amplitude can couple to noise, as these fluctuations may be detected at the output of the interferometer. The coupling of these fluctuations to the detector output is drastically reduced by operating the interferometers at a ‘dark fringe’ working point, where in the absence of any signal the interferometer output is null. In an interferometer with exactly matched arms, fluctuations in the laser frequency do not couple to the detector output. However, in reality small differences between the

two arms inevitably exist, and so the laser frequency must be stabilised by means of a feedback loop using a high-finesse optical cavity as a reference [DHK<sup>+</sup>83].

Beam jitter noise arises from a coupling of fluctuating beam alignment to power in the detector output. If the beams from the two arms do not spatially overlap perfectly at the beam splitter, the superposition will be incomplete and the interferometer output will no longer be null. The most common way to reduce the beam jitter to acceptable levels is by passing the beam through one or more *mode cleaner* cavities, which filter out the higher-order modes which are equivalent to misalignments [RSS<sup>+</sup>81].

Residual gas pressure noise arises from the difference in refractive indices of volumes of different gas pressure within the arms of an interferometer. The phase of light in the arms of an interferometer is dependent upon the refractive index of the medium which fills the arms. Therefore if the medium in one arm is of a higher refractive index than the medium in another arm, the interference at the beam-splitter will be affected. This very effect is used to measure refractive indices of materials in Michelson interferometers. In an interferometric gravitational wave detector however, any changes in these refractive indices will be observed at the output as noise. In order to reduce the effect of residual gas pressure noise, the arms of all interferometric gravitational wave detectors are kept in a state of high vacuum.

## 1.6. First generation ground-based gravitational wave detectors

In the 1990s and the 2000s a number of large-scale interferometric gravitational wave detectors were built; these are classed as members of the ‘first generation’ of interferometric gravitational wave detectors. Figure 1.3 shows the optical topology of a basic Michelson interferometer, along with the topologies of some of these first generation detectors. These detectors were designed to reach broadband strain sensitivities on the order of  $10^{-22}\sqrt{\text{Hz}}$ , and they achieved this goal in the late 2000s. Even with such unprecedented levels of sensitivity, the rate of detectable events was expected to be low - on the order of 0.2 events per year for the most optimistic prediction for the most common sources [AAA<sup>+</sup>10]. Despite the lack of a detection, the work that went into designing and building these detectors has pushed back the boundaries of what is achievable with interferometers. In building the detectors a wealth of knowledge has been built up about

the noise sources present in interferometric detectors and the ways in which they can be reduced. Pioneering work on the GEO600 detector in particular has led to the development of many new techniques which are likely to be used in the second-generation detectors which are approaching the commissioning stage.

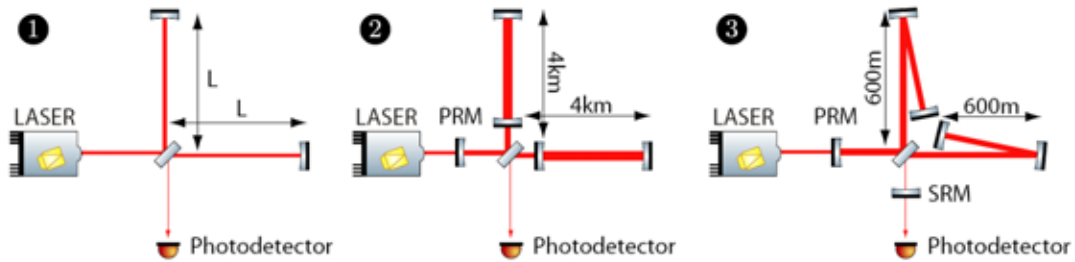


Figure 1.3.: Three different optical layouts for Michelson type gravitational wave detectors. Layout 1 is the basic Michelson topology. Layout 2 includes a power recycling mirror and Fabry-Perot arm cavities, and is similar to the topologies of the LIGO, Virgo and TAMA300 detectors. Layout 3 includes a power recycling mirror, a signal recycling mirror and delay lines. This is similar to the topology of the GEO600 detector. Image used courtesy of S. Chelkowski.

The GEO600 detector, situated in Ruthe, Germany is a 600 m arm length interferometer built as the result of a collaboration between interferometry groups from Glasgow in Scotland, and Hannover in Germany [WAA<sup>+</sup>04]. This detector has served as a test-bed for a range of advanced interferometric techniques, such as dual recycling [GLSC08], the DC readout method [HGD<sup>+</sup>09], and squeezed light injection [KVL<sup>+</sup>11]. Dual recycling is a combination of two techniques; power recycling and signal recycling. Power recycling is a method whereby a mirror placed between the laser source and the beam-splitter is used to create an enhanced light power within the detector. The power recycling technique is feasible in gravitational wave detectors because the interferometer is kept on a dark fringe in the absence of gravitational wave signals. As a result, little light escapes from the output in the absence of a signal, instead being reflected towards the input. By placing a mirror at the interferometer output it is possible to keep the light circulating in the interferometer, thus enabling very high light powers to be reached in the arms and improving the signal to shot noise ratio. Signal recycling may be considered

a second generation technique, and so is described briefly in section 1.7. GEO600 also makes use of so-called delay lines in the arms to increase the effective arm length.

The LIGO, Virgo and TAMA detectors are all very similar in the principle of their design. They are essentially large scale Michelson interferometers, with the addition of the aforementioned power recycling mirror, and Fabry-Perot arm cavities. The arm cavities increase the effective length of the arms in a similar manner to delay lines; light circulates many times within the cavities before recombining at the beam-splitter. The American LIGO detector consists of three interferometers; two based in Hanford, Washington, and one based in Livingston, Louisiana [BW99]. Two of these interferometers have arm lengths of 4 km, and the other has arms of length 2 km. The Virgo detector situated near Pisa in Italy, is the result of a French-Italian collaboration and has arms of length 3 km [AAA+08]. The Japanese TAMA300 detector has arms of length 300 m, and is situated near Tokyo [KKF+95].

## 1.7. Second generation ground-based detectors

The first generation detectors have recently completed their period of scientific data recording. Work has now begun on upgrading them to second generation detectors, which are expected to reach sensitivities around 10 times greater than their previous incarnations. This increase in sensitivity will have a strong impact on the expected rates of observable events, due to the cubic dependence of the searchable volume of space on the sensitivity. The optimistic event rate for the most common source, neutron star - neutron star binary inspiral systems, increases from 0.2 events per year to 400 events per year with the increase in sensitivity from the first generation of detectors to the second generation [AAA+10].

An upgrade of two of the LIGO detectors is nearly complete; the upgraded detector will be known as Advanced LIGO, or aLIGO. The updates will include the implementation of the signal recycling technique as well as advanced suspensions for the optics and a new laser with higher power [ABHK08]. The go-ahead was also recently given to move one of the aLIGO interferometers to India, where the geographical separation will improve the sky localisation abilities of the detector network, as described for the slightly different case of moving one interferometer to Australia in [AFK+11]. The Virgo detector will undergo similar changes to its layout and will be known in the future as Advanced Virgo

[FFG<sup>+</sup>05]. The Japanese gravitational wave detection community is currently working on a new detector called KAGRA. This detector will use cryogenic methods to cool the optical components of the interferometer to very low temperatures in a bid to reduce the effects of thermal noise [KLC06]. Some of the second generation techniques, along with the benefits they offer, are described here.

### **Signal recycling**

Signal recycling is a technique whereby the signal sidebands of the electromagnetic field, which are created when a gravitational wave passes through the detector, are recycled back into the arms of the interferometer by means of a mirror placed at the output [Bar97]. The light can then interact many times with gravitational waves propagating through the detector, and for a small frequency band this effect will be resonant, resulting in amplification of the gravitational wave signal. A tunable signal recycling technique may be a viable option for second generation detectors, whereby the frequency of optimum sensitivity can be adjusted in order to search for gravitational waves at different frequencies.

### **Schemes to increase circulating light power**

The power recycling technique has already led to an improvement in the level of light power which can be obtained within interferometers. Further research into new laser technology has also led to the development of lasers with higher output powers, helping to further reduce the effects of shot noise in interferometric gravitational wave detectors [WPK<sup>+</sup>11]. As the light powers in detectors gets higher, the effects of radiation pressure and thermal lensing become increasingly serious problems. It is conceivable that a maximum feasible light power will be reached, until the effects of radiation pressure and thermal lensing are reduced.

## 1.8. Future gravitational wave detectors

### Third generation ground-based detectors

There are a number of interferometry techniques which are so new that they are not being considered for inclusion in the majority of second generation gravitational wave detectors. These techniques are described as third generation techniques, and it is expected that their implementation in future detectors will enable them to reach sensitivities roughly 100 times those of current detectors. One example of such a technique is the use of ‘squeezed light’ interferometers [Che07]. The use of cryogenically cooled optical components in order to reduce the effects of thermal noise may be a common feature of third generation detectors. These techniques may include the use of so called ‘quantum non-demolition’ interferometry to surpass the standard quantum limit on interferometer sensitivity [DK12]. Higher-order LG mode interferometry, the technique with which this project is chiefly concerned, may also feature among the new technologies present in third generation gravitational wave detectors.

## 1.9. Structure of this thesis

The goal of this thesis is to present a motivation for my studies on higher-order LG mode interferometry in the context of improving the sensitivity of future gravitational wave detectors, and then to describe the work carried out during my PhD. The aim is also to provide the necessary background to understand the work described, as well as its implications for future research on this topic.

In this thesis I will focus first on the thermal noise of the test masses in ground-based interferometric gravitational wave detectors, and then discuss the potential of higher-order modes to reduce the effects of this noise in chapter 2. Next I will discuss some initial theoretical and numerical investigations into the generation of higher-order LG modes, as well as their interferometric performance in chapter 3. In chapter 4 I will describe the table-top experiments I performed at Birmingham to investigate the generation of higher-order LG modes with a spatial light modulator, and their interactions with optical resonators. I will then discuss the issue of higher-order LG mode degeneracy in high-finesse optical cavities, and describe my work carried out in collaboration with the interferometry group at the University of Glasgow on the 10 m prototype de-

tector facility with the goal of assessing the impact of the mode degeneracy issue on the feasibility of using LG modes in future detectors in chapter 5. Finally, a summary of the work and the conclusions drawn from it, as well as the outlook and future prospects of the topic will be presented in chapter 6.

## Chapter 2.

# Laguerre-Gauss beams for test mass thermal noise reduction

Test mass thermal noise was not a dominant noise source in the first generation of gravitational wave detectors. However, with the upgrade to second generation detectors, a factor of 10 increase in sensitivity in the whole frequency band is aimed for, and at such improved sensitivities thermal noise *is* expected to be one of the major limiting noise sources. The Brownian thermal noise in particular is expected to be of sufficient magnitude to obscure gravitational wave signals around the 100 Hz region in the advanced detectors, unless new techniques are employed to reduce the effect. This point is illustrated in the projected sensitivity of the Advanced LIGO detector, shown in figure 2.1. From the second generation onwards therefore, advancements in other areas of the interferometers, such as the implementation of higher laser powers, will make a limited impact in the 100 Hz region unless the thermal noise of the test masses can be reduced. Research into methods for reducing the effects of this noise source is therefore of paramount importance to the gravitational wave community.

### 2.1. Test mass thermal noise

The total thermal noise of the test masses is commonly considered as a sum of four different sources of thermal noise in the phase of light reflected from the test mass. First of all, contributions from the coating and the substrate are dealt with separately, as a result of different approximations being appropriate for each of these two components of the test mass. For each of the coating and the substrate, the total thermal noise is

considered as an incoherent sum of *Brownian* noise and *thermo-optic* noise contributions<sup>1</sup>.

A rigorous description and analysis of Brownian noise, and thermoelastic and thermorefractive noises (the two components of thermo-optic noise), as well as thermal deformation of substrates in the context of higher-order LG beams in gravitational wave detectors can be found in [Vin09]. For a coherent treatment of thermo-optic noise for the LG<sub>00</sub> mode see [EBF<sup>+</sup>08]. As yet a coherent analysis of thermo-optic noise for higher-order LG modes is not available.

### Brownian thermal noise

This noise source arises due to excitations of the elastic modes of mirrors and their coatings caused by Brownian motion of their constituent atoms. These excitations lead to an uncertainty in the position of the reflecting surface. The fluctuation in the phase of the reflected light that results is indistinguishable from a phase change in the light that would be caused by gravitational waves, and thus appears as noise at the detector output. As with the suspensions, the effect of the thermal excitations can be minimised by using materials with very high Q-factors. Using high Q materials confines the fluctuations due to each resonant mode of the mirror or coating to a very narrow band around the resonance frequency. Since the resonant frequencies of the modes of oscillation lie above the observation band of the detector (>6 kHz) [Lev98], the amplitude of oscillations within the observation band are significantly suppressed.

Brownian noise of the test mass substrates was initially calculated by summing the contributions from many normal-modes of the substrate until convergence was reached [GR95]. Levin showed in [Lev98], however, that a more computationally efficient solution could be found by implementing the fluctuation dissipation theorem (FDT) [CW51]. Levin also showed that the FDT method calculated contributions from surface losses more accurately than the normal-mode decomposition method, which relies on the assumption of homogeneously distributed sources of friction within the material. It should be kept in mind when using the results of the FDT treatment of Levin that they also have assumptions inherent; in particular, the assumption that one is only interested in calculating the thermal noise at frequencies well below the lowest eigenfrequency of the

---

<sup>1</sup>Previously, the thermo-optic noise had been considered as an incoherent sum of *thermoelastic* noise and *thermorefractive* noise. This view has been revised however, in light of the fact that thermoelastic and thermorefractive effects are not necessarily incoherent processes [EBF<sup>+</sup>08].

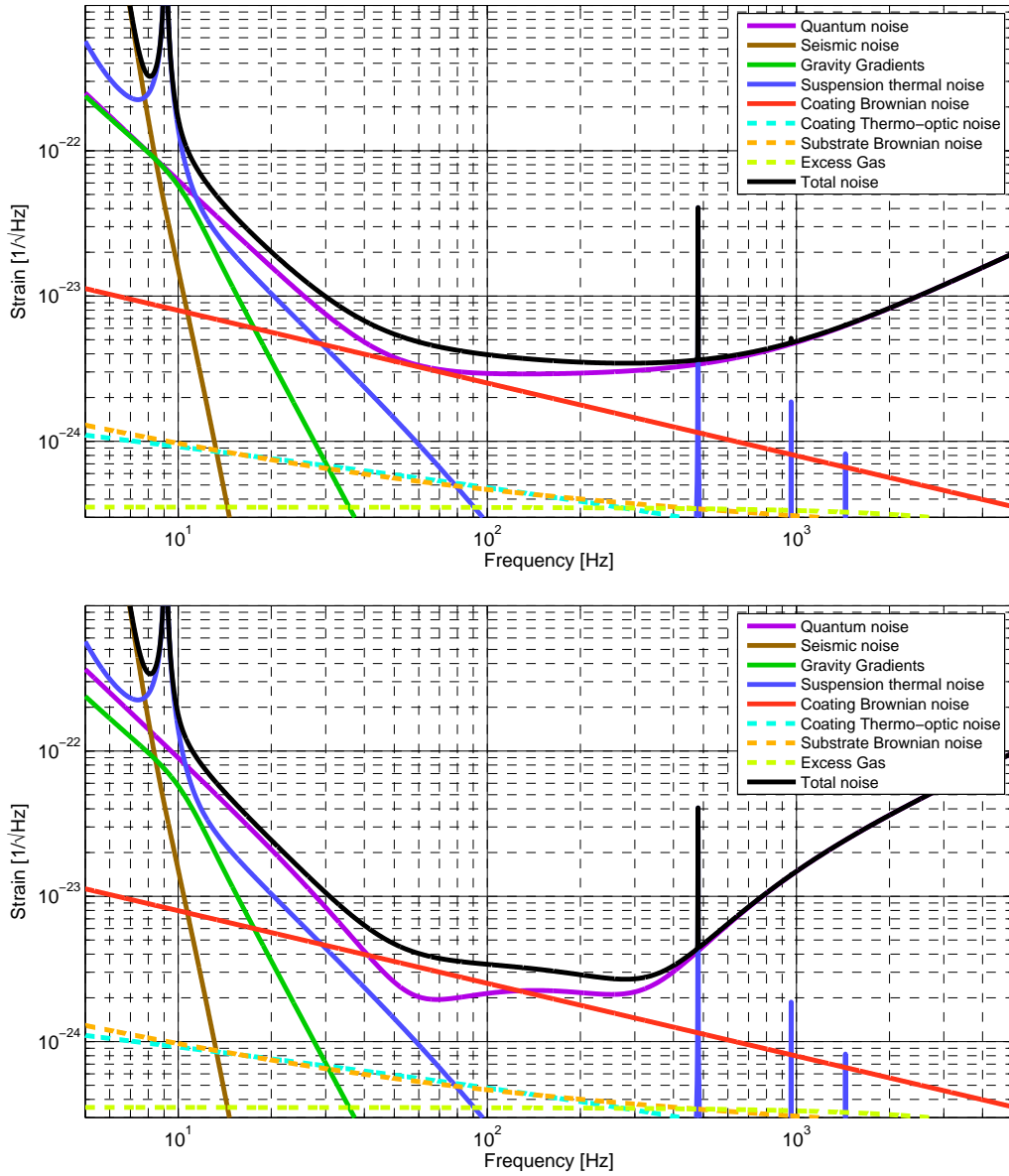


Figure 2.1.: The Advanced LIGO noise budget, in tuned signal recycling configuration for optimal broadband sensitivity (upper plot) and detuned signal recycling configuration for optimal sensitivity to binary neutron star sources (lower). The contributions of the individual noise sources are shown by the coloured lines. The quantum noise shown is the sum of shot noise and radiation pressure noise, as described in section 1.5.

system. While this may be a valid assumption for current designs, this should be re-evaluated for different test masses in the future, which if larger than current test masses may have resonant frequencies closer to the detection band.

Using the method described in [Lev98], the spectral density of Brownian thermal noise is given by

$$S_x(f) = \frac{4k_B T}{\pi f} \phi U, \quad (2.1)$$

where  $T$  is the temperature of the relevant material,  $\phi$  is known as the ‘loss angle’ and represents the retardation effect associated with dissipation in the material, and  $U$  is the strain energy at static pressure normalised for 1 N [Lev98]. The factor  $U$  has some dependence on the material properties, but interestingly also depends on the intensity distribution of the readout beam. This is where the advantage of higher-order LG beams manifests itself, as shall be discussed in more detail later on in this chapter.

For the Brownian noise in the substrate, in the case of an infinite sized mirror where the beam radius is considered much less than the mirror radius,

$$U = \frac{1 - \sigma^2}{2\sqrt{\pi} Y w}, \quad (2.2)$$

where  $\sigma$  is the Poisson ratio of the material,  $Y$  is the Young’s modulus of the material, and  $w$  is the  $1/e^2$  radius of the fundamental Gaussian mode readout beam [BHV98]. For the Brownian noise in the coating, under the same infinite mirror approximation, Vinet showed that

$$U = \delta_C \frac{(1 + \sigma)(1 - 2\sigma)}{\pi Y w^2} \Omega_1, \quad (2.3)$$

where  $\delta_C$  is the coating thickness, and  $\Omega_1$  is a factor which includes higher order corrections due to differences between the coating material parameters and the substrate parameters [Vin09]. It should be noted that the coating Brownian noise level, which in the second generation detectors is expected to be the leading test mass thermal noise contribution, scales with the inverse square of the readout beam size. The substrate Brownian noise level, on the other hand, scales inversely with the beam size. This dependence of the thermal noise level on beam size was the driving factor for the Advanced LIGO design to use significantly larger beam sizes on the test masses than in initial LIGO [HLSC10].

### Thermo-optic noise

Thermo-optic noise arises from the fluctuating temperature field within a material. The changes in temperature couple to the phase of light reflected from the test mass in two ways; via the thermal expansion of the test mass, and the change in refractive index of the coating. Previously, these two couplings of temperature fluctuations to readout beam phase have been referred to as thermoelastic noise and thermorefractive noise respectively, as discussed in for example [LT00] and [BV03].

Thermoelastic noise is caused when the thermodynamic fluctuations cause strain fluctuations within the material as the hotter volumes expand and the colder volumes contract. These strain fluctuations then cause an additional excitation of the elastic modes of the materials, leading to uncertainties in the surface position as in the case of Brownian thermal noise. The spectral density for thermoelastic noise in the low frequency limit is given by

$$S_x(f) = \frac{k_B T}{\pi^2 f^2} W \quad (2.4)$$

where the variables are as previously defined for Brownian noise except for  $W$ , which is the average energy dissipated by the coupling of the temperature field to strain in the material [Vin09]. This is effectively equivalent to equation 2.1, except this time we consider  $W$  as the energy dissipated through coupling between the strain and the temperature field in the material. The thermal expansion coefficient  $\alpha$  effectively determines the coupling of temperature fluctuations to strain fluctuations, and appears later in calculations of the  $W$  factor. In fused silica,  $\alpha$  is relatively small at room temperature, and so the predicted thermoelastic noise level in gravitational wave interferometers is orders of magnitude lower than the Brownian thermal noise level. This may not always be the case however. Sapphire has been proposed as another candidate substrate material, largely due to its good Brownian noise performance. However, the thermal expansion coefficient of sapphire is significantly higher than that of fused silica and so thermoelastic noise may be the limiting thermal noise if sapphire test masses are used in the future [RHC05]. The choice of new substrate materials for reducing thermal noise is further discussed in section 2.2.

Thermorefractive noise is similar to thermoelastic noise in that it arises from the temperature fluctuations within the material, but the coupling to phase noise is in this case via the  $\frac{\partial n}{\partial T}$  coefficient; the rate of change of refractive index with temperature [EBF<sup>+</sup>08].

The level of thermorefractive noise is also expected to be orders of magnitude lower than the Brownian noise contribution for the currently used test masses, although as with thermoelastic noise, this may change in the future. Preliminary investigations have shown a very low  $\frac{\partial n}{\partial T}$  coefficient for silicon at cryogenic temperatures. As is discussed in the next section, this may be an important factor in the choice of materials for the mirror substrates in future detectors.

Since these two noise sources share the same origin, however, the simple treatment of them as incoherent is not necessarily adequate. In [EBF<sup>+</sup>08], Evans demonstrates a rigorous coherent treatment of thermoelastic and thermorefractive noise, and shows that the incoherent treatment leads to an overestimation of the thermo-optic noise at 100 Hz in Advanced LIGO of around a factor of 4.

The power spectrum of the thermal fluctuations that give rise to the thermo-optic noise is given by

$$S_{TO} = \frac{2}{\pi^{\frac{3}{2}}} \frac{k_B T^2}{w^2 \sqrt{\kappa C f}}, \quad (2.5)$$

where  $w$  is the beam spot size,  $\kappa$  is the thermal conductivity of the material, and  $C$  is the heat capacity per unit volume of the material. Estimates for the coating thermo-optic noise level in aLIGO using this treatment put it at around a factor of 8 below the coating Brownian noise level, as shown in figure 2.1. As a result, Evans states that this noise source should not be considered a driving force in the design of aLIGO [EBF<sup>+</sup>08]. However, this result should be re-evaluated for designs of future detectors, which may use different materials and may operate in different temperature regimes, both of which may give rise to different  $\alpha$  and  $\frac{\partial n}{\partial T}$  coefficients, as well as a different coherence level between the two dissipation processes.

## 2.2. Thermal noise reduction techniques

### Cryogenic interferometry

Perhaps the most obvious technique that can be employed to reduce the level of thermal noise in gravitational wave detectors is to cool the optics and final stage suspensions to cryogenic temperatures. The noise spectral density of *most* of the aforementioned

thermal noises reduces with temperature in *most* cases, although there is the possibility for exceptions to this rule caused by the variation in  $\alpha$  and  $\frac{\partial n}{\partial T}$  with temperature.

There are unfortunately some difficulties associated with implementing cryogenic test-masses in large scale interferometers. Firstly, the test-masses are deliberately well isolated, and thus extracting heat from them is difficult. The current suspensions have a high thermal resistance due to their small cross sectional area, large length, and low thermal conductivity. Also, large low temperature baffles known as cryo-shields are required to avoid the heating up of the mirrors due to absorption of thermal radiation from the room temperature beam tubes. Cryogenic interferometry has been demonstrated nonetheless, at the Japanese interferometer CLIO [YUM+08]. A new Japanese cryogenic interferometer, KAGRA, has been funded and will begin construction very soon. This detector will serve well to elucidate the subject of cryogenic interferometry for the gravitational wave community, as well as serving as a highly sensitive detector in its own right [SKC11].

### **New coating methods and materials**

The levels of all thermal noises in mirror coatings depend on the mechanical loss mechanisms of the materials from which they are made. The Q-factor of the material is of primary importance for determining how excitations caused by either the Brownian or the thermoelastic noise mechanisms translate into noise in the detector. Materials with high Q-factors confine the movement of the mirrors caused by these noise mechanisms to narrow frequency bands, and therefore mitigate the effect on the sensitivity. The level of thermo-optic noise is also determined by the  $\alpha$  and  $\frac{\partial n}{\partial T}$  coefficients, so these should be considered when choosing new materials.

Fused silica performs well enough at room temperature in all respects for the first generation of gravitational wave detectors not to be limited by thermal noise. However, the more exacting requirements of the next generation of detectors have triggered a search for better coating methods and materials, as described in for example [IWM10] and [HABT+07]. The possibility of employing cryogenic interferometry must also be considered, as the  $\alpha$  and  $\frac{\partial n}{\partial T}$  coefficients as well as the Q-factor can vary significantly over the temperature range from a few to 300 K, in addition to the obvious gains from reducing  $T$ . Silicon has shown considerable promise as a possibly well performing substrate and coating material at low temperatures, to the extent that it is strongly considered for

inclusion in the third-generation Einstein Telescope design [HAA<sup>+</sup>11].

In addition to the search for new materials, new methods of making high-reflective coatings are also being investigated. The ‘waveguide coating’ technique developed in collaboration between Jena and Hannover has shown promising results so far [FBB<sup>+</sup>11], and crystalline ‘epitaxial coatings’ are also a strong consideration in a potential Advanced LIGO upgrade [BGH<sup>+</sup>12].

### All-reflective interferometers

One way to avoid the thermal problems that result from using very high laser powers is to reduce the number of transmissive optical elements that the main laser travels through. By employing diffractive grating cavities instead of the currently used transmissive ones, all reflective interferometer configurations can be designed [Dre96]. There are two advantages of using all reflective configurations; firstly since the optics are no longer required to be transmissive, a greater selection of materials with potentially better thermal noise characteristics become viable options for substrates. Secondly in all reflective configurations less beam power will be absorbed by the optics, thus making cryogenic operation easier to achieve and reducing the impact of all thermal problems. This technology has encountered some difficulties due to the introduction of additional phase noise due to translation of the gratings [HCF<sup>+</sup>09], but on the positive side investigations into this effect were partially responsible for the development of the waveguide coating technology [FBB<sup>+</sup>11].

### Compound end mirrors - ‘Khalili cavities’

Another idea for reducing the effects of coating thermal noise is to employ compound mirrors in place of the end test masses [Kha05]. The idea is based on the fact that the level of coating Brownian noise scales with the number of coating layers used to make the reflective surface of the test mass. In typical gravitational wave interferometers, most of the coating layers are on the end test mass surfaces, as these are required to have the highest reflectivity. By replacing the single end mirror with a compound mirror made up of two mirrors controlled to a state which is anti-resonant for the carrier light, a high reflectivity can potentially be achieved with significantly fewer coating layers on the first of the two mirrors. Although there will be many coating layers on the

second mirror, a relatively small proportion of the light intensity will actually probe this mirror surface, and so the coupling to the detector output is small. This technology is still in early stages of development, but there are plans to test it at the Hannover 10m prototype facility [GBB<sup>+</sup>10]. The main difficulties in employing this technique are expected to arise from the lack of geometric stability in the short cavity, and the associated problems in controlling the extra degrees of freedom that are introduced.

### Flat readout beams

Spreading the readout beam power over a larger portion of the mirror surface area can reduce the thermal lensing effect and all of the substrate and coating thermal noises. This requires the introduction of so-called flat readout beams, such as higher-order LG beams. As this technology was the main focus of the work comprising this thesis, the thermal noise advantages it may bring are described in more detail in later on in this chapter in section 2.6.

## 2.3. The mode picture for laser beams

Throughout this thesis I will be discussing the properties of different spatial laser modes, so it is fitting to give an introduction to the concept of these modes. In this section I will first describe what is meant by the term spatial laser modes, and then describe two of the mode sets commonly used to describe the transverse properties of laser beams; the Hermite-Gauss (HG) modes and the LG modes.

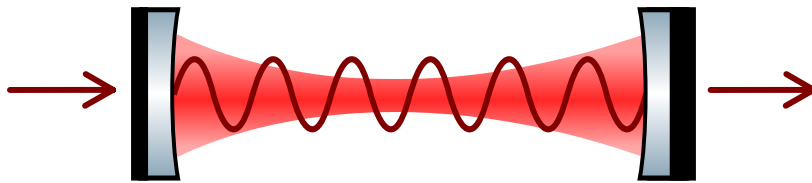


Figure 2.2.: A cartoon picture of an optical cavity. Light enters the cavity through the input mirror from the left, and resonates inside the cavity if its length is divisible by an integer number of half wavelengths. The maroon sinusoid represents the longitudinal mode properties, and the red shaded area represents the transverse mode properties.

The mode picture of laser beams is intimately related to the properties of light within optical resonators. In lasers, an optical resonator, or cavity, is almost always used to predefine the geometric properties and the frequency of the generated laser light. Light produced from the laser transitions in the lasing material circulates in an optical resonator, and the output beam is transmitted through a semi-transparent mirror. For the purposes of this discussion, however, we will consider a two mirror optical cavity, as shown in figure 2.3 with light incident on one mirror. In a similar manner to other resonators, an optical resonator has the potential to produce any of an infinite number of resonant modes. The mode of operation of a laser is defined by both the frequency of the light and the geometric properties of the beam. In the context of optical resonators, these two properties are known as the *longitudinal* and *transverse* and mode orders respectively.

For the longitudinal mode order of an optical resonator, it is instructive to consider the response of an ideal optical resonator in the plane wave approximation, i.e. without considering the transverse properties of the light. The circulating power within an optical resonator for an input power of 1 W is given by

$$P_{circ} = \frac{T_1}{1 + R_1 R_2 - 2r_1 r_2 \cos(2kL)}, \quad (2.6)$$

where  $T_1$  is the power transmissivity of the input mirror,  $R_1$  and  $R_2$  are the power reflectivities of the input and output mirrors respectively,  $L$  is the cavity length, and  $k = 2\pi/\lambda$  is the wavenumber of the light [FS10]. It can be seen that there is an infinite set of discrete light frequencies that give a maximal circulating light power for a given cavity length, wherever  $2kL = n\pi$  ( $n=1,2,3\dots$ ). This can be easily understood if we consider each resonance as a case fulfilling the criterion that an integer number of half wavelengths matches the cavity length exactly, creating a resonant standing wave inside the cavity.

The transverse mode of an optical resonator describes the geometry of the beam cross section, in a plane perpendicular to the propagation vector. An infinite set of transverse modes of an optical resonator with spherically curved mirrors can be found by solving the paraxial wave equation with the boundary conditions given by the cavity parameters, namely the cavity length and the curvatures of the mirrors. The paraxial wave equation is simply the wave equation for the electric field with the additional approximation that the light field is beam-like, i.e. varying much more rapidly along the transverse axes than the propagation axis. We can describe an electric field to be a product of a function describing the spatial properties and the oscillating function in the propagation direction

$z$  as

$$E(x, y, z) = u(x, y, z) \exp(-ikz). \quad (2.7)$$

If we substitute this into the wave equation for the electric field we get

$$\frac{\partial^2 u}{\partial x^2} + \frac{\partial^2 u}{\partial y^2} + \frac{\partial^2 u}{\partial z^2} - 2ik \frac{\partial u}{\partial z} = 0. \quad (2.8)$$

The condition on the variation in beam shape being slower in  $z$  than in  $x$  and  $y$  is formalised as

$$\left| \frac{\partial^2 u}{\partial z^2} \right| \ll \left| \frac{\partial^2 u}{\partial x^2} \right|, \left| \frac{\partial^2 u}{\partial y^2} \right|, \left| 2k \frac{\partial u}{\partial z} \right|, \quad (2.9)$$

leading us to the paraxial form of the wave equation if we neglect the much smaller second derivative in  $z$ :

$$\frac{\partial^2 u}{\partial x^2} + \frac{\partial^2 u}{\partial y^2} - 2ik \frac{\partial u}{\partial z} = 0. \quad (2.10)$$

There exist many solutions to equation 2.10, each representing a transverse mode of the electric field. The lowest order solution is the commonly observed Gaussian beam, with transverse field distribution given by

$$u(x, y, z) = \sqrt{\frac{2}{\pi}} \frac{1}{w(z)} \exp(i\Psi(z)) \exp\left(-ik \frac{x^2 + y^2}{2R_C(z)} - \frac{x^2 + y^2}{w^2(z)}\right), \quad (2.11)$$

where  $w(z)$  is known as the Gaussian spot size parameter<sup>2</sup>,  $\Psi(z)$  is the Gouy phase (which is discussed in more detail in section 4.3), and  $R_C(z)$  is the radius of curvature of the spherical phase front.

There also exist several infinite sets of solutions to the paraxial wave equation, each including the Gaussian mode as well as higher-order solutions. The two sets which are of interest in this work are the LG modes and the Hermite-Gauss (HG) modes. Both of these mode sets are complete, which means that they can be used to construct an orthonormal basis-system in which all solutions to the paraxial wave equation can be represented as linear combinations of the basis modes. Since all beam-like electric fields should satisfy the paraxial wave equation, we can therefore use linear combinations of LG or HG modes to describe *any* beam shape.

One feature that is common to all transverse modes of spherical optical resonators is their self-reproducing intensity patterns; as they propagate, the overall scale of the transverse

<sup>2</sup>The distance from the optical axis at which the beam power is  $1/e^2$  of the power at the optical axis.

field distribution will change, but the shape remains constant. This is to be expected, since in order for a mode to be resonant in an optical cavity it must have the same transverse field distribution after successive round trips of the cavity. The Gaussian mode is an obvious example of a mode with a self-reproducing intensity pattern, since the propagation of a mode may be described by Fourier transforming the initial Gaussian amplitude cross section, and the Fourier transform of a Gaussian function is another Gaussian function. In the next two sections we describe the two aforementioned sets of higher-order solutions to the paraxial wave equation, the HG and LG mode sets.

## 2.4. The Hermite-Gauss mode set

The HG mode set are solutions to the paraxial wave equation in Cartesian coordinates, and exhibit rectangular symmetry. As a result of this, their amplitude profiles can be easily separated into the  $x$  and  $y$  components. The separability in  $x$  and  $y$  means that HG modes can be eigenmodes of astigmatic spherical optical resonators, which is a result of significance for the work described in chapter 5. As a consequence of this separability, the full amplitude profile of HG modes can be expressed as

$$u_{nm}(x, y, z) = u_n(x, z)u_m(y, z). \quad (2.12)$$

The  $u_n(x, z)$  and  $u_m(y, z)$  functions describe the variation of amplitude in the orthogonal  $x, z$  and  $y, z$  planes, and have an identical form. The variation in the  $x, z$  plane is given by

$$u_n(x, z) = \left(\frac{2}{\pi}\right)^{\frac{1}{4}} \exp(i(2n+1)\Psi(z)) \times H_n\left(\frac{\sqrt{2}x}{w(z)}\right) \exp\left(-i\frac{kx^2}{2R_C(z)} - \frac{x^2}{w^2(z)}\right), \quad (2.13)$$

where  $n$  is the relevant mode index,  $H_n$  is the Hermite polynomial of order  $n$ , and the rest of the parameters are as previously defined. The order of a HG mode is simply the sum of the two orthogonal transverse mode indices. The intensity patterns of the HG modes up to the order 6 are shown in figure 2.3.

Although we first described the higher-order HG modes as mathematical solutions to the paraxial wave equation, these modes are readily observed in a table-top optical resonator when the input beam is slightly misaligned. This is because misalignments

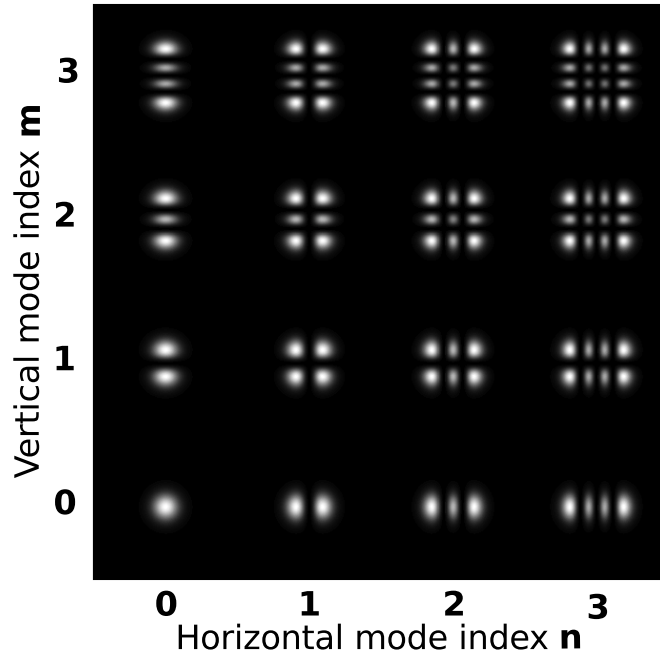


Figure 2.3.: Intensity patterns for Hermite-Gauss modes up to the order 6. The intensity patterns are normalised to have the same peak intensity, for visibility.

or translations of the input beam with respect to the optical axis of the cavity cause coupling from the  $\text{HG}_{00}$  mode into higher-order HG modes. This modal description of misalignments and translations was formalised by Bayer-Helms in [Bay84], and is illustrated in figure 2.4. This plot shows the amplitude cross sections of a  $\text{HG}_{00}$  mode, a  $\text{HG}_{10}$  mode, and the linear combination of both. We can see that to a reasonable approximation, the combination of the two modes appears as a translated  $\text{HG}_{00}$  mode. The addition of higher order modes to the sum, as prescribed by the Bayer-Helms relations published in [Bay84], increases the accuracy of the description of translations in this manner. This modal description of beam shapes is employed in the interferometer simulation package FINESSE [FHL<sup>+</sup>04], which was used for several simulation tasks described in this thesis.

## 2.5. The Laguerre-Gauss mode sets

The LG modes are solutions to the paraxial wave equation in cylindrical polar coordinates, as opposed to in Cartesian coordinates in the case of HG modes. Unlike the HG

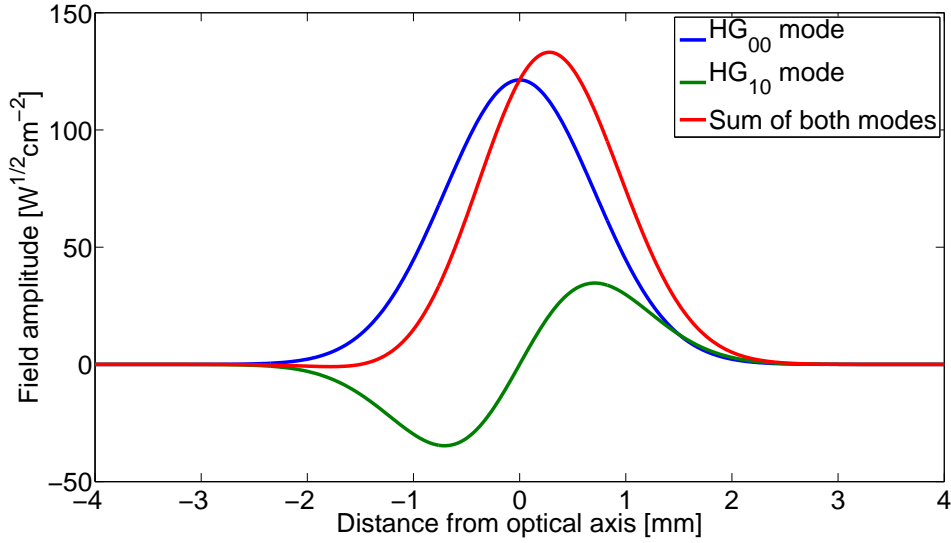


Figure 2.4.: Amplitude cross sections of a  $\text{HG}_{00}$  mode of power 0.9 W, a  $\text{HG}_{10}$  mode of power 0.1 W, and the sum of both with a total power of 1 W. To first order, the combination of  $\text{HG}_{00}$  and  $\text{HG}_{10}$  modes is equivalent to a translated  $\text{HG}_{00}$  mode.

modes therefore, the complex amplitude function for LG modes is not separable in  $x$  and  $y$ , and so LG modes are not eigenmodes of astigmatic optical resonators. LG modes are commonly expressed in two different forms, which I will refer to as the sinusoidal mode set and the helical mode set. While both sets of LG modes have the property of axisymmetry, only the helical set all have circularly symmetric intensity profiles. This property can be useful for reducing the effects of Brownian thermal noise, as is described in further detail later on in section 2.6. Helical LG beams also have the unusual property of carrying orbital angular momentum, which has made them the subject of study by the scientific community in the last two decades or so [ABSW92]. This trait has led to their use as ‘optical spanners’ and ‘optical waveguides’ [HFHRD95] in the bio-photonics and cold atoms fields.

The complex amplitude distribution of the sinusoidal LG mode set is given by

$$\begin{aligned}
 u_{p,l}^{\text{cosine}}(r, \phi, z) &= \frac{2}{w(z)} \sqrt{\frac{2p!}{\pi(|l|+p)!}} \exp(i(2p+|l|+1)\Psi(z)) \\
 &\times \left(\frac{\sqrt{2}r}{w(z)}\right)^{|l|} L_p^l\left(\frac{2r^2}{w(z)^2}\right) \exp\left(-ik\frac{r^2}{2q(z)}\right) \cos(l\phi),
 \end{aligned} \tag{2.14}$$

where all variables are as defined for equation 2.11, except  $p$ ,  $l$  and  $L_p^l$ , which are the radial mode index, the azimuthal mode index, and the associated Laguerre polynomials respectively. The complex amplitude of helical LG modes shown in equation 2.15 is similar in most respects to that for the sinusoidal set, except for the different azimuthal dependence of  $\exp(il\phi)$  instead of  $\cos(l\phi)$ . This azimuthal phase dependence is what gives helical LG modes with non-zero  $l$  orbital angular momentum. The mode order of both sets of LG beams is given by  $2p + l$ .

$$u_{p,l}^{\text{helical}}(r, \phi, z) = \frac{1}{w(z)} \sqrt{\frac{2p!}{\pi(|l| + p)!}} \exp(i(2p + |l| + 1)\Psi(z)) \times \left(\frac{\sqrt{2}r}{w(z)}\right)^{|l|} L_p^{|l|}\left(\frac{2r^2}{w(z)^2}\right) \exp\left(-ik\frac{r^2}{2q(z)} + il\phi\right) \quad (2.15)$$

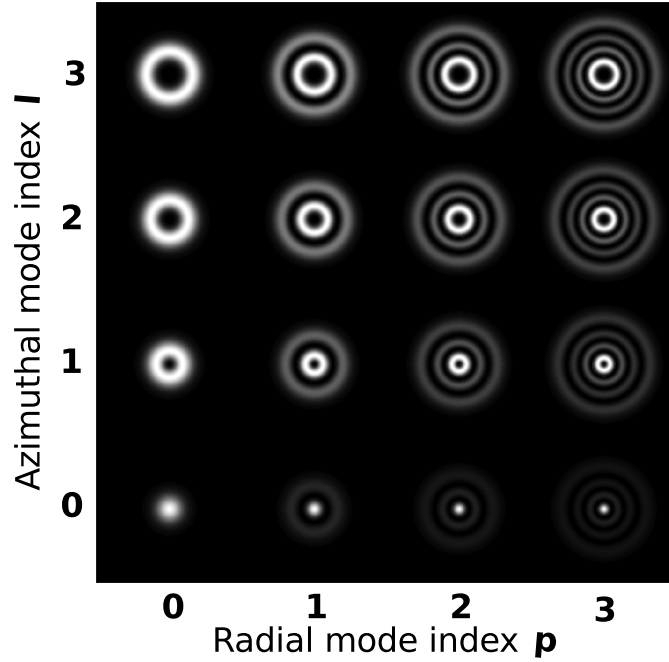


Figure 2.5.: Intensity patterns for helical LG modes up to order 9. The intensity patterns are normalised to have the same peak intensity, for visibility.

The intensity distributions for the modes up to the order 9 of the helical and sinusoidal LG mode sets are shown in figures 2.5 and 2.6 respectively. The radial mode index  $p$  determines the number of radial nodes that appear in the amplitude cross section of the beam and is equivalent for sinusoidal and helical modes. The azimuthal mode index  $l$

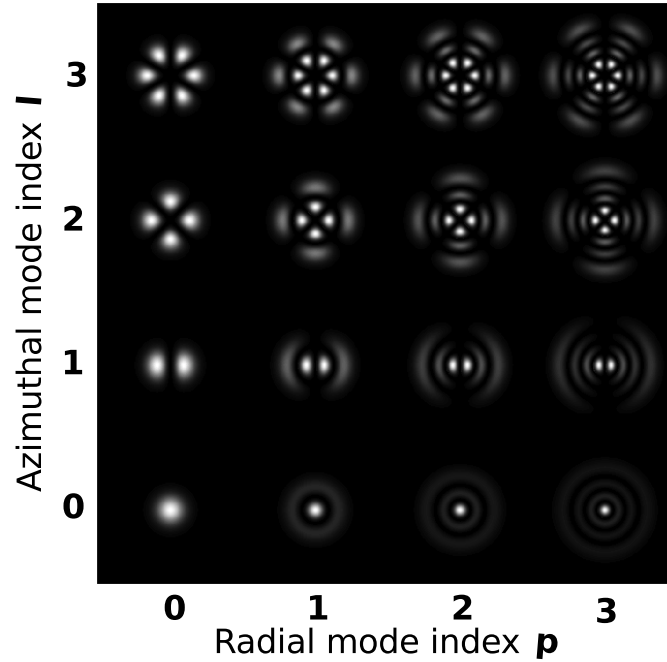


Figure 2.6.: Intensity patterns for sinusoidal LG modes up to order 9. The intensity patterns are normalised to have the same peak intensity, for visibility.

determines the number of azimuthal nodes for the cosine modes. For the helical modes however,  $l$  determines the number of  $2\pi$  phase shifts that appear around a circle of constant  $r$  and consequently the angular momentum per photon in the beam, which is known to be  $l\hbar$  [ABSW92]. One may think of the helical LG modes as being a linear combination of two sinusoidal LG modes with the same mode indices but with a phase shift of  $\pi/2$  between them, since Euler's theorem states that  $\exp(il\phi) = \cos(l\phi) + i\sin(l\phi)$ . This fact is useful in understanding the results reported in section 4.4.

As with the HG modes, the LG modes are often observed in optical resonators as the result of imperfect matching of the input beam to the cavity eigenmode. LG modes tend to appear more as the result of axisymmetric mismatches however, such as the mismatch of the input beam waist position or size to that of the cavity eigenmode, rather than misalignments. This coupling can also be seen in the work of Bayer-Helms in [Bay84]. Figure 2.7 illustrates the connection between a mismatch of beam size or position and the effects of adding higher-order LG modes. We see that to a rough approximation, adding a  $LG_{10}$  mode to a  $LG_{00}$  mode results in another  $LG_{00}$  mode but with a different beam size parameter. As in the case of figure 2.4, the addition of higher order modes to

the sum will increase the accuracy of this approximation.

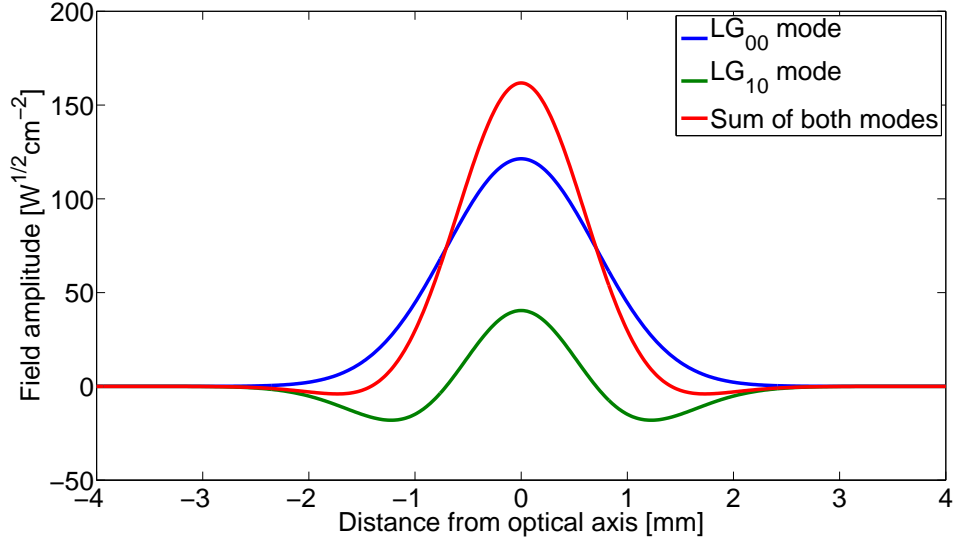


Figure 2.7.: Amplitude cross sections of a  $LG_{00}$  mode of power 0.9 W, a  $LG_{10}$  mode of power 0.1 W, and sum of both with total power 1 W. To a reasonable approximation, the combination of  $LG_{00}$  and  $LG_{10}$  modes is equivalent to a  $LG_{00}$  mode with a smaller beam spot size parameter.

Since both the LG mode sets and the HG mode sets are complete sets of solutions to the paraxial wave equation, it follows that it is possible to describe any LG mode as a linear combination of HG modes, and vice-versa. We can decompose the LG modes into a weighted sum of HG modes by making use of the relations between Laguerre polynomials and Hermite polynomials, as shown in [BAvW93]. The complex amplitude of a LG mode may be given in terms of HG modes by

$$u_{pl}(x, y, z) = \sum_{k=0}^{2p+l} i^k b(l+p, p, k) u_{2p+l-k, k}^{\text{HG}}(x, y, z), \quad (2.16)$$

where  $b(l+p, p, k)$  are the real coefficients given by

$$b(l+p, p, k) = \sqrt{\frac{(2p+l-k)!k!}{2^{(2p+l)}(l+p)!p!}} (-2)^k P_k^{l+p-k, p-k}(0), \quad (2.17)$$

and  $P_n^{\alpha, \beta}(x)$  are the Jacobi polynomials. This transformation between LG and HG mode sets is used to model LG modes with the simulation software FINESSE, which was designed to use the HG mode set to describe beam shapes. The relation between LG

and HG modes demonstrates that it is incorrect to say that HG modes exclusively describe misalignments and translations while LG modes describe exclusively mismatches of beam waist size and position, since both mode sets can describe all four mismatches independently. However, due to the symmetries inherent in the two mode sets, each is a more convenient basis set for describing the mismatches which share their symmetry.

## 2.6. Reduction in thermal noise for higher-order LG beams

The thermal noise equations given in section 2.1 have a dependence on the intensity distribution of the readout beam. This dependence appears in the strain energy factor  $U$  in equation 2.1 for the case of Brownian noise as

$$U = 2\pi \frac{1 - \sigma^2}{Y} \int_0^\infty \tilde{I}(k)^2 dk, \quad (2.18)$$

where  $\sigma$  is the Poisson ratio,  $Y$  is the Young's modulus and  $\tilde{I}(k)$  is the Hankel transform of  $I(r)$ , the normalised intensity of the readout beam [Vin09]:

$$\tilde{I}(k) = \int_0^\infty I(r) J_0(kr) r dr. \quad (2.19)$$

In the case of a fundamental Gaussian mode readout beam, this gives the results for  $U$  shown in equations 2.2 and 2.3, for noise in the substrate and coating respectively. In these equations we see an inverse relationship between  $U_{\text{sub}}$  and the beam spot size,  $w$ , and an inverse square relationship between  $U_{\text{coat}}$  and  $w$ .

The dependence of the Brownian noise on the intensity distribution of the readout beam is best understood in terms of 'averaging' over the fluctuations on the mirror surface. Put simply, the more evenly spread the power in the readout beam is, the better the beam averages over surface distortions, and the less significant the Brownian component of phase noise in the beam becomes. The intensity of fundamental mode beams with very large beam sizes on the mirrors will be very evenly distributed. However, beam sizes on the mirrors cannot be made arbitrarily large due to problems associated with beam clipping losses. This is where so-called flat beams such as mesa-beams and higher-order LG beams have an advantage over the fundamental Gaussian beam, as they can average over the surface better for a given clipping loss.

The clipping loss at an optical component is the fraction of the optical power in the beam that is not incident on the optical surface, i.e. that which is lost beyond its perimeter.

This can be calculated as

$$L_{\text{clip}} = 1 - \int_0^{2\pi} d\phi \int_0^R I(r, \phi) r dr d\phi, \quad (2.20)$$

where  $I(r, \phi)$  is the beam intensity distribution function and  $R$  is the radius of the optical component. In order to make a fair comparison between the thermal noise performances of different mode shapes we must ensure that all the modes compared have the same clipping losses at a mirror of given size. Since higher-order LG beams are more spatially extended it is therefore necessary to compare beams with different spot sizes.

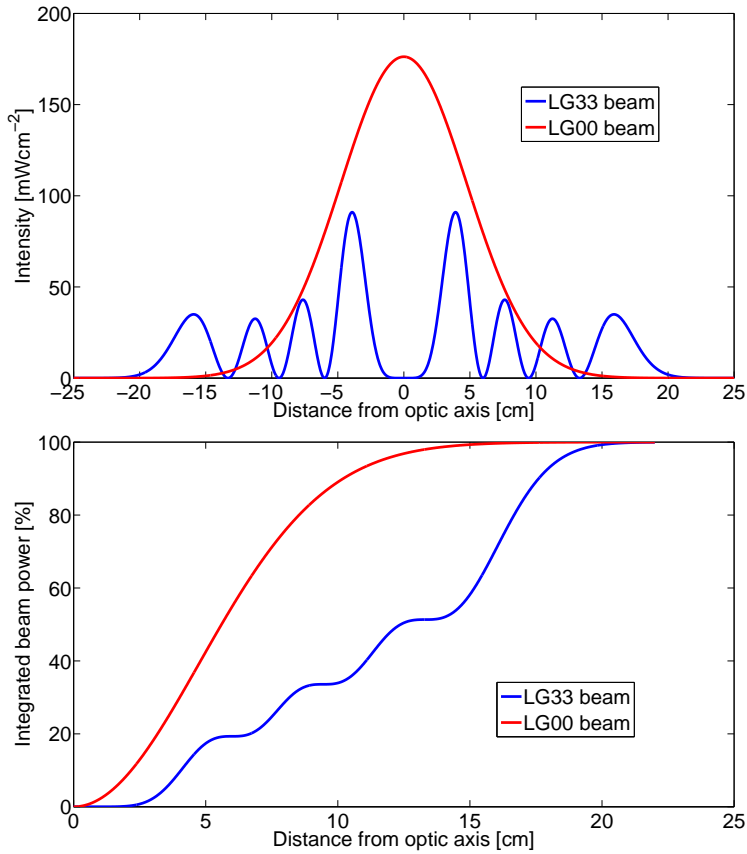


Figure 2.8.: The upper panel shows the intensity as a function of distance from the optic axis for a LG<sub>33</sub> beam and a LG<sub>00</sub> beam, both of which experience a 1 ppm clipping loss on a mirror with a radius of 25 cm and have equal total beam powers of 1 W. The lower panel shows the integrated beam power as a function of distance from optic axis for the same two beams.

For a given amount of clipping loss on a circular<sup>3</sup> mirror face of a given radius, the optical power is distributed more evenly for higher-order LG beams than for the fundamental LG<sub>00</sub> beam. This effect is illustrated in figure 2.8. The upper panel of figure 2.8 is a plot of the intensity profiles of a LG<sub>33</sub> mode and a LG<sub>00</sub> mode, both of which have the same total power, and the same clipping loss of 1 ppm on a fixed optic size. It is clear that the peak intensity of the LG<sub>00</sub> is higher than that of the LG<sub>33</sub>, indicating that more of the total power is concentrated in one region. The lower panel shows the integrated beam power as a function of distance from the optical axis, for the same two beams. The average gradient of the slope for the LG<sub>33</sub> beam is shallower than that of the LG<sub>00</sub> beam, again demonstrating that the beam power is more evenly spread over the surface of the optic for the LG<sub>33</sub> beam.

The idea of using different beam shapes to reduce the thermal noise levels in this way originally came from a proposal to use flat top, or ‘mesa’ beams [DOS<sup>+</sup>04]. However, these beams have the disadvantage of being incompatible with the currently used spherical mirror surfaces. The maturity of the technology to manufacture the ‘Mexican hat’ mirrors that would be required to support such a beam in a cavity is much less than the technology for manufacturing spherical mirrors. Since higher-order LG modes also offer a thermal noise advantage, but are compatible with the currently used spherical mirrors, we found this idea to be more favourable for consideration in the context of gravitational wave interferometers.

## 2.7. Coating Brownian thermal noise reduction factors for higher-order modes

### 2.7.1. Helical Laguerre-Gauss modes

After Mours’ initial paper suggesting the use of higher-order LG modes as a flat beam candidate for thermal noise reduction [MTV06], Vinet published calculations of the thermal noise performance for mesa-beams and higher-order LG modes in [Vin09], and also for higher-order HG modes in [Vin10]. I will summarise these results here for the

---

<sup>3</sup>Only cylindrical mirrors are considered in this discussion because this geometry gives the mirror a high Q factor. This reduces the advantage of using higher-order HG modes, which would average better over the surface of rectangular mirrors.

## 2.7. Coating Brownian thermal noise reduction factors for higher-order modes

---

coating Brownian noise, as this is currently expected to be the dominant test mass thermal noise source in the second generation of gravitational wave detectors. I will also take the additional step of accounting for the different beam sizes required to maintain a fixed clipping loss of 1 ppm for each mode.

In [Vin09] Vinet calculated the advantage of higher-order beams is calculated for coating Brownian noise in the numerical values  $g_{pl}$ , which scale the strain energy as

$$U_{pl}^{\text{CoatBrown}} = \delta_C \frac{(1 + \sigma)(1 - 2\sigma)}{2\sqrt{\pi}Yw^2} g_{pl} \quad (2.21)$$

where all other symbols are as defined in equation 2.3 . Table 2.1 shows some numerical values of  $g_{pl}$ . However, in order to make a fair comparison between the different modes,

l	0	1	2	3	4	5
p						
0	1	0.5	0.34	0.27	0.22	0.19
1	0.5	0.31	0.23	0.19	0.16	0.14
2	0.38	0.25	0.19	0.16	0.14	0.12
3	0.31	0.21	0.17	0.14	0.12	0.11
4	0.27	0.19	0.15	0.13	0.11	0.10
5	0.25	0.17	0.14	0.12	0.11	0.10

Table 2.1.: Coating Brownian noise scaling factors  $g_{pl}$  for  $\text{LG}_{pl}$  modes relative to the  $\text{LG}_{00}$  mode. The same beam size parameter is assumed for each mode.

we should compare beams with the same clipping losses. Table 2.2 shows the beam size scaling factors  $a_{pl}$  for  $\text{LG}_{pl}$  modes relative to the  $\text{LG}_{00}$  mode in order that each mode has the same clipping loss of 1 ppm on an arbitrary sized mirror.

Since the coating Brownian noise scales with the inverse square of the beam size parameter (see equations 2.3 and 2.21), we must take account of the beam size scaling factors when calculating the real thermal noise improvement of higher-order LG modes. We therefore calculate the actual coating Brownian noise power spectral density improvement factor as

$$\Theta_{pl}^{\text{CoatBrown}} = \frac{a_{pl}^2}{g_{pl}}. \quad (2.22)$$

These coating Brownian noise improvement factors for higher-order LG modes, normalised for 1 ppm clipping loss, are shown in table 2.3.

l	0	1	2	3	4	5
p						
0	1.00	0.836	0.741	0.675	0.626	0.587
1	0.920	0.785	0.707	0.650	0.606	0.571
2	0.850	0.747	0.679	0.628	0.589	0.556
3	0.804	0.715	0.655	0.609	0.573	0.544
4	0.768	0.689	0.634	0.593	0.559	0.535
5	0.737	0.666	0.616	0.578	0.547	0.529

Table 2.2.: Beam size scaling factors  $a_{pl}$  between  $LG_{00}$  and  $LG_{pl}$  modes that give 1 ppm clipping loss on an arbitrary sized circular mirror [Vin10].

l	0	1	2	3	4	5
p						
0	1.00	1.40	1.61	1.69	1.78	1.81
1	1.66	1.99	2.17	2.22	2.30	2.33
2	1.90	2.23	2.42	2.47	2.47	2.58
3	2.09	2.44	2.52	2.65	2.74	2.69
4	2.18	2.50	2.68	2.70	2.84	2.86
5	2.17	2.61	2.71	2.78	2.72	2.80

Table 2.3.: Coating Brownian noise power spectral density improvement factors  $\Theta_{pl}^{\text{CoatBrown}}$  for  $LG_{pl}$  modes over the  $LG_{00}$  mode, where all modes are scaled to give 1 ppm clipping loss on a fixed mirror size.

In the case of the  $LG_{33}$  mode, for which the majority of the research described in thesis was carried out, we see that the coating Brownian noise power spectral density is reduced by a factor of 2.65 from the level experienced when using the  $LG_{00}$  mode as the readout beam. It was this clear and significant potential advantage of using the  $LG_{33}$  mode that encouraged us to investigate it further within the context of gravitational wave interferometers. The improvement factors offered by  $LG_{pl}$  modes for other thermal noise sources are shown in appendix A.

### 2.7.2. Hermite-Gauss modes

Although higher-order HG modes might not be expected to give as good thermal noise performance as the higher-order helical LG modes due to their lack of circularly symmetric intensity profiles, it is still interesting to see what improvement they can offer over the LG<sub>00</sub> mode. This is especially interesting in light of some of the results reported in chapter 5, where we saw that a 10m suspended cavity appeared to preferentially resonate with HG modes despite being pumped with a LG mode.

The beam size scaling factors  $a_{nm}$  for HG<sub>nm</sub> modes, relative to the LG<sub>00</sub> mode, required to give a 1 ppm clipping loss are shown in table 2.4

m	0	1	2	3	4	5
n						
0	1	0.910	0.842	0.789	0.746	0.710
1	0.910	0.850	0.798	0.754	0.718	0.686
2	0.842	0.798	0.756	0.721	0.689	0.662
3	0.789	0.754	0.721	0.690	0.664	0.640
4	0.746	0.717	0.690	0.664	0.640	0.619
5	0.710	0.687	0.662	0.640	0.619	0.600

Table 2.4.: Beam size scaling factors  $a_{nm}$  between HG<sub>00</sub> and HG<sub>nm</sub> modes to give 1 ppm clipping loss on an arbitrary sized circular mirror.

The results for the coating Brownian noise power spectral density improvement factors  $\Theta_{nm}^{\text{CoatBrown}}$  for HG<sub>nm</sub> modes over the LG<sub>00</sub> mode were calculated in the same way as for LG modes as

$$\Theta_{nm}^{\text{CoatBrown}} = \frac{a_{nm}^2}{g_{nm}}. \quad (2.23)$$

The numerical values for these improvement factors are shown in table 2.5 for HG<sub>nm</sub> modes up to HG<sub>55</sub>. From this table we can see that higher-order HG modes do have a coating Brownian noise power spectral density advantage over the HG<sub>00</sub> mode, though this improvement is less significant than those calculated for the LG modes as shown in table 2.3. At the equivalent mode order as the LG<sub>33</sub> mode, the HG<sub>45</sub> offers only a factor 1.47 improvement, compared with the LG<sub>33</sub> improvement of 2.65. The improvement

factors offered by  $\text{HG}_{nm}$  modes for other thermal noise sources are shown in appendix A.

m	0	1	2	3	4	5
n						
0	1	1.10	1.11	1.08	1.05	1.02
1	1.10	1.29	1.33	1.40	1.30	1.27
2	1.10	1.33	1.40	1.41	1.41	1.39
3	1.08	1.32	1.41	1.44	1.45	1.45
4	1.05	1.30	1.41	1.45	1.47	1.47
5	1.02	1.27	1.39	1.45	1.47	1.48

Table 2.5.: Coating Brownian noise power spectral density improvement factors  $\Theta_{nm}^{\text{CoatBrown}}$  for  $\text{HG}_{nm}$  modes over the  $\text{HG}_{00}$  mode, where all modes are scaled to give 1 ppm clipping loss on a fixed mirror size.

## 2.8. Thermal lensing

Another thermal effect, aside from thermal noise itself, which must be considered is that of thermal lensing in the optical substrate materials. Light is absorbed in the substrates and coatings of the partially transmissive mirrors; most significantly the power recycling mirror, the arm cavity mirrors and the central beam splitter. For the  $\text{LG}_{00}$  mode, absorption is strongest in the centre of the mirrors, on the optic axis of the beam. A radial thermal gradient results, and if the thermo-refractive coefficient  $\frac{\partial n}{\partial T}$  or the thermal expansion coefficient  $\alpha$  of the substrate is non-zero, a thermal lens is produced. An inability to accurately compensate for the thermal lens effect, which will vary with different laser powers and may be non-stationary in time, will lead to imperfect matching of the beam to the interferometer eigenmode and those of the arm cavities therein. This leads to a power loss within the interferometer and an increase in light coupled into higher-order modes [DZJB04].

Thermal compensation systems have been in place at the LIGO and Virgo detectors already, but these have proven tricky to implement successfully [LZF<sup>+</sup>02]. With higher laser powers expected in future detectors an advance in the methods of thermal com-

compensation may be required to capitalise on the potential shot noise improvement. Vinet shows in [Vin09] that the higher-order LG modes have a significantly better performance than the  $LG_{00}$  mode in terms of thermal distortions of mirrors caused by power absorption in the coating, due to the more even absorption of power across the mirror surface. This is a considerable advantage of higher-order LG beams, as dealing with high-power instabilities such as non-stationary thermal lensing is expected to be one of the major difficulties in commissioning and running the advanced detectors. The use of higher-order LG modes can be expected to relax the requirements on the thermal compensation subsystem.



## Chapter 3.

# Simulation study into $LG_{33}$ mode interferometry and production

Motivated by the potential factor of 2.65 improvement in coating Brownian noise power spectral density using the  $LG_{33}$  mode, as shown in section 2.7, a numerical numerical investigation into the interferometric performance of the  $LG_{33}$  mode was pursued. This chapter includes the methods and results of the numerical interferometric performance study, in which the compatibility of the  $LG_{33}$  mode with standard techniques in the gravitational wave interferometer community were investigated, such as the Pound-Drever-Hall longitudinal error signal generation for optical cavities, and the Ward technique for generating alignment error signals for cavities. Also investigated investigated were the coupling of alignment degrees of freedom to phase noise in an advanced detector-like layout, and finally the potential increase in observable event rate was calculated for two typical gravitational wave sources with the Advanced Virgo detector, in the case where the  $LG_{33}$  mode was used in place of the  $LG_{00}$  mode.

Following the positive results of the numerical interferometric performance study, we proceeded with a numerical study into the means of higher-order LG mode generation. This study included the design of phase profiles for use with spatial light modulators or diffractive optical elements that can convert the  $LG_{00}$  mode into higher-order LG modes, as well as the optimisation of the beam size parameter upon conversion and a derivation of the beam parameters subsequent to conversion.

### 3.1. Interferometric performance simulation study of the $LG_{33}$ mode

For any new technology to be seriously considered for inclusion in the design of a gravitational wave interferometer, its compatibility with other techniques that are already in place must first be demonstrated. Typically the development of a new technology for gravitational wave interferometers happens in several stages; first the potential advantages of the technology are evaluated, secondly a simulation study is performed to assess the compatibility with the interferometer, thirdly table-top experiments are performed to demonstrate the technology, and finally the technology is tested on a suspended prototype interferometer. In this section we will describe the second, and to some degree also the first of these stages, under the banner of an interferometric performance study. Interferometric performance in this context refers specifically to the ability to generate the required longitudinal and alignment control signals, the level of coupling of a number of variables to the measured phase (phase noise analysis), and finally the maximum achievable detector sensitivity.

The first consideration to ensure a realistic analysis of the performance of the  $LG_{33}$  mode was the beam sizes which should be compared. As we saw in sections 2.6 and 2.7, a smaller beam size is required for the  $LG_{33}$  mode in order to have the same clipping loss as the  $LG_{00}$  mode for a fixed optic size. If we take the maximum allowed clipping loss to be 1 ppm<sup>1</sup>, the  $LG_{33}$  beam size at an optic must be a factor of 1.64 smaller than the  $LG_{00}$  beam which also experiences the same clipping loss.

The performance of three different configurations for a symmetric 3km cavity were compared, which are referred to as the  $LG_{33}$ ,  $LG_{00}^{\text{large}}$  and  $LG_{00}^{\text{small}}$  configurations. The  $LG_{33}$  and  $LG_{00}^{\text{large}}$  configurations both have a clipping loss of 1 ppm at the cavity mirrors, thus the beam size at the mirrors for the  $LG_{00}^{\text{large}}$  configuration is a factor of 1.64 larger than for the  $LG_{33}$  configuration. The  $LG_{00}^{\text{small}}$  configuration has the same spot size at the mirrors as the  $LG_{33}$  configuration, but uses a  $LG_{00}$  beam, and therefore has a lower clipping loss. The  $LG_{00}^{\text{small}}$  configuration is really a control configuration, included in the study in order to better separate the effects due beam parameters and effects due directly to mode shape. The cavity mirror curvatures for each configuration are shown

---

<sup>1</sup>This is a somewhat arbitrary number, but it is commonly used throughout the gravitational wave community, and is related to the acceptable round trip cavity losses.

in table 3.1, and the rest of the cavity parameters were as detailed in the Advanced Virgo reference design [FM06].

Configuration	$LG_{00}^{\text{large}}$	$LG_{33}$	$LG_{00}^{\text{small}}$
$R_C$ (m)	1537	1910	1910
$w$ (mm)	57.7	35.2	35.2
$w_0$ (mm)	8.9	16.3	16.3
$L$ (km)	3	3	3
Finesse	1227	1227	1227

Table 3.1.: Cavity parameters for each of the three different configurations used in the study.  $R_C$ ,  $w$ ,  $w_0$  and  $L$  refer to the mirror radii of curvature, the beam spot size at the mirrors, the beam waist size, and the cavity length respectively. The cavity finesse is defined as the ratio of the full width at half maximum of a cavity resonance to the separation of successive resonances [Sie86]. The  $LG_{33}$  and  $LG_{00}^{\text{small}}$  configurations have the same cavity parameters, since the  $LG_{00}^{\text{small}}$  configuration was a control test to help distinguish between the effects of beam parameters and mode shape.

### 3.1.1. Longitudinal control signals

The first control signal investigated was the longitudinal error signal for a single cavity, generated using the Pound-Drever-Hall (PDH) modulation/demodulation error signal generation technique [DHK<sup>+</sup>83]. The compatibility of the  $LG_{33}$  mode with the PDH method is crucial to its application in gravitational wave interferometers, as this method is used to control many degrees of freedom within gravitational wave interferometers, and as such is one of the key techniques that enables their successful operation. One would expect the  $LG_{33}$  mode to perform identically as for the  $LG_{00}$  in this test, as the PDH error signal is known to be dependent not on the transverse beam profile, nor on the cavity geometry, but simply on the average phase of the beam within the cavity. Nonetheless, a demonstration of this result was required to confirm the expectation.

A FINESSE [FHL<sup>+</sup>04] model was made of each configuration, in which a carrier light field is phase modulated and then used as the pump light for a 3 km cavity, with geometry prescribed by the particular beam parameters for that configuration. The reflected

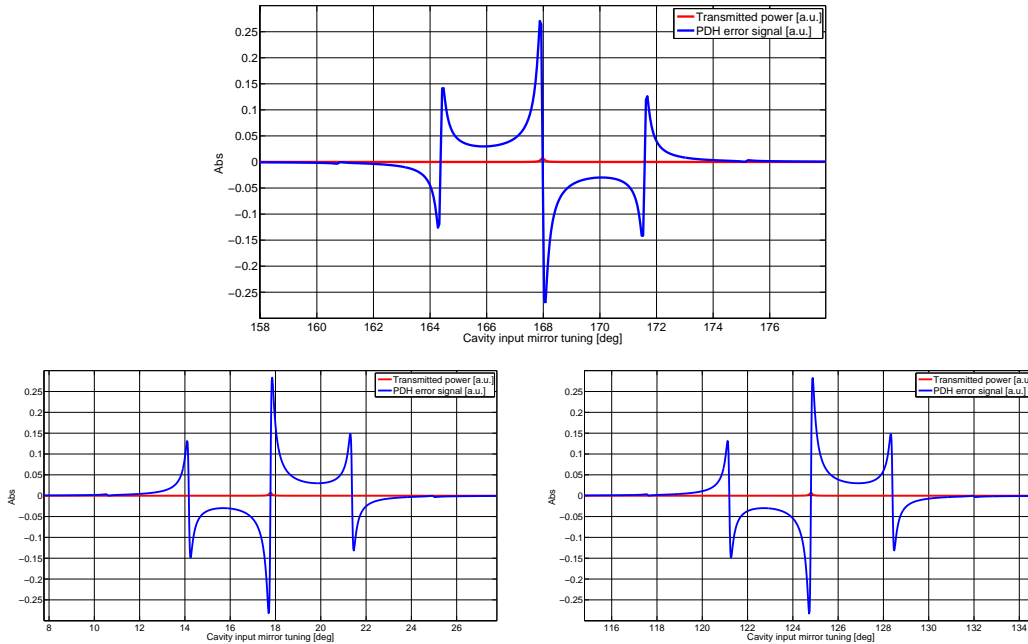


Figure 3.1.: PDH error signals for the 3 km cavity, for the three different configurations.

The upper plot shows the results for the  $LG_{33}$  configuration, the lower left plot is for the  $LG_{00}^{\text{large}}$  configuration and the lower right plot is for the  $LG_{00}^{\text{small}}$  configuration.

light from the cavity is detected with a photodetector, and demodulated at the original modulation frequency. The cavity length was scanned over the resonant peak, and the resulting error signal plotted, as shown in figure 3.1. From this figure we can see that the resulting longitudinal control signal was identical for all three of the considered configurations, except with the opposite sign for the  $LG_{33}$  mode case<sup>2</sup>. This confirmed our expectation, providing the evidence that crucially the  $LG_{33}$  is compatible with the widely used PDH error signal generation method.

### 3.1.2. Alignment control signals

As well as length sensing and control, angular sensing and control is crucial to maintaining the stable operation and maximum sensitivity of a gravitational wave interferometer.

<sup>2</sup>The opposite sign of the error signal in the case of the  $LG_{33}$  mode is of no consequence; one could simply alter the demodulation phase or invert the signal after demodulation to recover the same sign.

To investigate how the  $LG_{33}$  mode performs in this respect, an alignment scheme based on the Ward technique described in [MRWM94a], and subsequently in [Hei99] was designed for the same 3 km cavity configurations as previously described. The optical layout for this scheme is shown in panel (A) of figure 3.2. As in the case of the PDH signal investigation, the carrier light is phase modulated and passed into the cavity, although this time via a beam splitter.

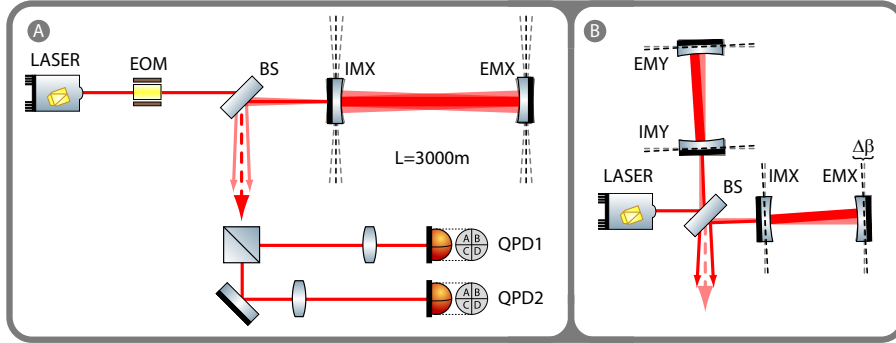


Figure 3.2.: Two optical layouts used in the alignment analysis simulations. (A) shows the single arm cavity alignment control scheme investigated, and (B) shows the differential misalignment of arm cavities, for which the coupling into dark port power was analysed.

The reflected beam from the cavity is split in two, and each resulting beam is passed through a telescope and detected with a quadrant photodetector. These telescopes are designed such that the Gouy phase (see equation 4.2) difference between the beams at each quadrant photodetector is  $90^\circ$ , in order to provide the maximum possible orthogonality between alignment signals from the end mirror and the input mirror. The difference signal from each quadrant photodetector is demodulated by mixing with the initial modulation frequency. The demodulation phase was chosen so as to maximise the slope of the error signal corresponding to the mirror for which the photodetector is required to sense the alignment. We performed the analysis for the case of rotations of the mirrors about the vertical axis (yaw) only, but the results are equally applicable to rotations about the horizontal axis (pitch). In order to match as closely as possible the conditions under which the alignment control system will be developed in practice, we tuned the parameters rather than using the theoretical optimum parameters.

Figure 3.3 shows the alignment signals sensed by each quadrant photodetector for mis-

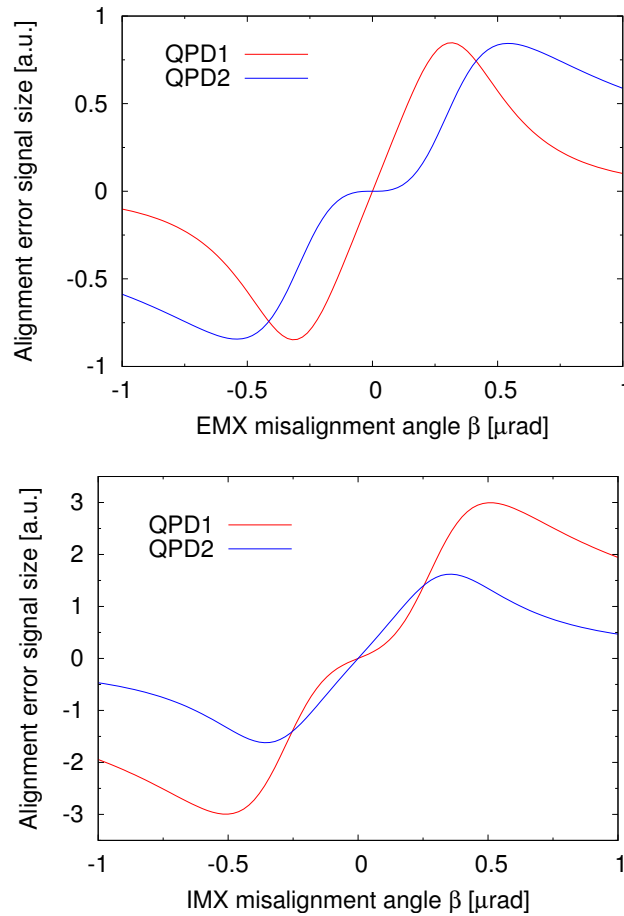


Figure 3.3.: Alignment error signals for a 3km cavity in the  $LG_{00}^{\text{small}}$  configuration, as sensed by both quadrant photodetectors QPD1 and QPD2 as a function of misalignment angle  $\beta$  of the cavity end mirror (top) and input mirror (bottom).

alignments of both the cavity input mirror and the end mirror, for the  $LG_{00}^{\text{small}}$  configuration. The top plot shows that at the working point, the error signal slope observed by QPD1 when the end mirror is misaligned is much steeper than that observed by QPD2. The lower plot shows the reverse scenario when the input mirror is misaligned; the steepest slope is observed by QPD2. This demonstrates a good separation of the two different alignment sensing degrees of freedom between the two sensors, which would enable the construction of a functioning alignment control loop for each degree of freedom.

The alignment sensing figure of merit for each configuration can be further summarised

by its control matrix [MF08]. The elements  $\sigma_{\text{detector}}^{\text{mirror}}$  of these control matrices are the slopes of the error signal at the working point as measured at quadrant photodetectors QPD1 and QPD2, for misalignments of the cavity input mirror IMX, and end mirror EMX, as shown in equation 3.1.

$$C_{\text{configuration}} = \begin{pmatrix} \sigma_{\text{QPD1}}^{\text{IMX}} & \sigma_{\text{QPD1}}^{\text{EMX}} \\ \sigma_{\text{QPD2}}^{\text{IMX}} & \sigma_{\text{QPD2}}^{\text{EMX}} \end{pmatrix} \quad (3.1)$$

The resulting control matrices for each of the three cavity configurations were as follows:

$$\begin{aligned} C_{LG_{33}} &= 7.444 \begin{pmatrix} 1 & 0.003 \\ 0.368 & 0.641 \end{pmatrix} \\ C_{LG_{00}^{\text{large}}} &= 17.77 \begin{pmatrix} 1 & 0.862 \\ 0.645 & 0.153 \end{pmatrix} \\ C_{LG_{00}^{\text{small}}} &= 5.615 \begin{pmatrix} 1 & 0.009 \\ 0.385 & 0.639 \end{pmatrix}. \end{aligned}$$

An ideal control matrix would be proportional to the identity matrix, since the off diagonal elements correspond to the presence of information from the unwanted mirror in a given photodetector signal. None of the configurations give an ideal control matrix, although it is clear that some perform better than others. Comparing the two configurations with the same clipping loss at the cavity mirrors, we can see that the  $LG_{33}$  configuration performs much better than the  $LG_{00}^{\text{large}}$  configuration. This is evident in the fact that the off-diagonal elements in the  $C_{LG_{00}^{\text{large}}}$  control matrix are larger with respect to the on-diagonal elements than in the  $C_{LG_{33}}$  control matrix. In fact, the off diagonal elements in  $C_{LG_{00}^{\text{large}}}$  are significantly larger even than the  $\sigma_{\text{QPD2}}^{\text{EMX}}$  element, demonstrating that misalignments of the end mirror couple more strongly to QPD1 even than QPD2, which should mostly sense end mirror misalignments.

A comparison between the  $C_{LG_{33}}$  and the  $C_{LG_{00}^{\text{small}}}$  control matrices shows very little difference between the two. Since these two configurations have the same cavity geometry and thus the same beam parameters, we can conclude that in this case the beam shape does not play a significant role in determining the alignment sensing performance of a configuration. We are left to conclude that the main factor determining the performance is in fact the cavity geometry, and that the  $LG_{33}$  mode *is* compatible with the alignment scheme used in the simulation.

### 3.1.3. Coupling of cavity mirror tilt to longitudinal phase

As well as investigating the compatibility of the  $LG_{33}$  mode with the commonly used interferometric sensing and control methods, we also investigated two of the main couplings of alignment degrees of freedom to noise in an interferometer. It is important to ascertain the impact of changing the beam shape on these couplings, since increased couplings from alignment degrees of freedom to phase noise will necessitate more stringent requirements on the residual alignment fluctuations.

One such coupling is between cavity mirror misalignment and the longitudinal phase in one of the arm cavities of an interferometer. As one of the cavity mirrors is misaligned, the effect on the cavity eigenmode optical axis will be either a tilt or shift, or some combination of both, with respect to the aligned axis [SS06, Hei99], depending on the cavity geometry and which mirror is misaligned. In the case of a symmetric cavity, the eigenmode will both tilt and shift when either of the mirrors are misaligned. A shifted eigenmode will experience a microscopically longer cavity round trip length than the perfectly aligned eigenmode. This effect is illustrated in figure 3.4 for the simple example of a flat-concave cavity, in which a misalignment of the concave mirror produces purely a shift in the eigenmode optical axis.

In a real interferometer, the longitudinal degree of freedom of the cavity will be controlled using the PDH method to keep it on resonance. Length changes caused by fluctuations in the alignment will be compensated for by the longitudinal control loops, and so the alignment fluctuations couple to the longitudinal degree of freedom, and hence to the gravitational wave strain channel as noise. Since this coupling is geometric in origin, one would not expect it to differ greatly between the  $LG_{33}$  configuration and the  $LG_{00}^{\text{small}}$  configuration, since the cavity geometry is equal for both. Figure 3.5 shows the intracavity power as a function of cavity end mirror tilt on the x-axis and longitudinal cavity tuning on the y-axis, for each of the three configurations. These plots demonstrate the level of coupling between end mirror tilt and longitudinal phase by showing the change in tuning required to keep the intracavity power at a maximum for a given tilt. Comparing the  $LG_{33}$  and  $LG_{00}^{\text{large}}$  configurations, we can see that the coupling is much stronger in the  $LG_{00}^{\text{large}}$  case (note the different y-axis scales). Over the  $1 \mu\text{rad}$  tilt range the resonant tuning of the  $LG_{33}$  configuration shifts by about  $0.4^\circ$ , compared to about  $5^\circ$  for the  $LG_{00}^{\text{large}}$  configuration<sup>3</sup>.

---

<sup>3</sup>Cavity tuning, expressed in degrees, is a convenient definition of either cavity length change as a

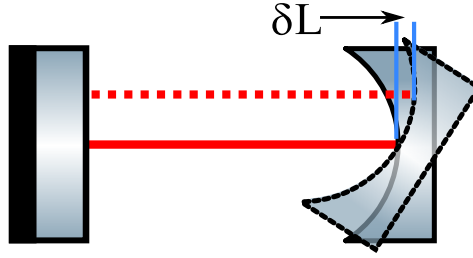


Figure 3.4.: An illustration of the coupling mechanism between misalignment and longitudinal phase in a plane-concave cavity. As the curved mirror is misaligned, the cavity eigenmode axis shifts, resulting in a longer round trip path length.

The results for the  $LG_{33}$  and  $LG_{00}^{\text{small}}$  configurations are very similar, as expected since they have the same cavity parameters. This suggests that the coupling from tilt to longitudinal phase in the cavity is dominated by the geometry of the cavity, and not by the beam shape. This is a positive result for the  $LG_{33}$  mode, in that it performs intrinsically no worse than the  $LG_{00}$  mode. In fact, when compared against the  $LG_{00}$  mode with the same clipping loss of 1 ppm in a 3 km cavity, the  $LG_{33}$  mode has a significantly lower coupling from tilt to longitudinal phase.

#### 3.1.4. Coupling of differential arm cavity misalignment to dark port power

The second alignment to interferometer noise coupling that we investigated was the coupling of differential arm cavity misalignment to power at the interferometer output port. If the two arm cavities are differentially misaligned, the overlap of the two beams at the central beam splitter will be imperfect, leading to a change in the light power present at the output port of the interferometer, as illustrated in panel (B) of figure 3.2. If this differential misalignment varies with time, the power measured at the dark port will also vary with time, producing a signal at the photodetector that is indistinguishable from gravitational wave signals. Static misalignments will also increase the coupling of common mode noise sources such as laser power fluctuations to the gravitational wave channel, since the interferometer will no longer be operating on an exactly dark fringe.

A FINESSE model was made to obtain values for the output power enhancement due to differential misalignment for each of the three previously described cavity configurations,

---

fraction of wavelength, or frequency change as a function of cavity FSR.

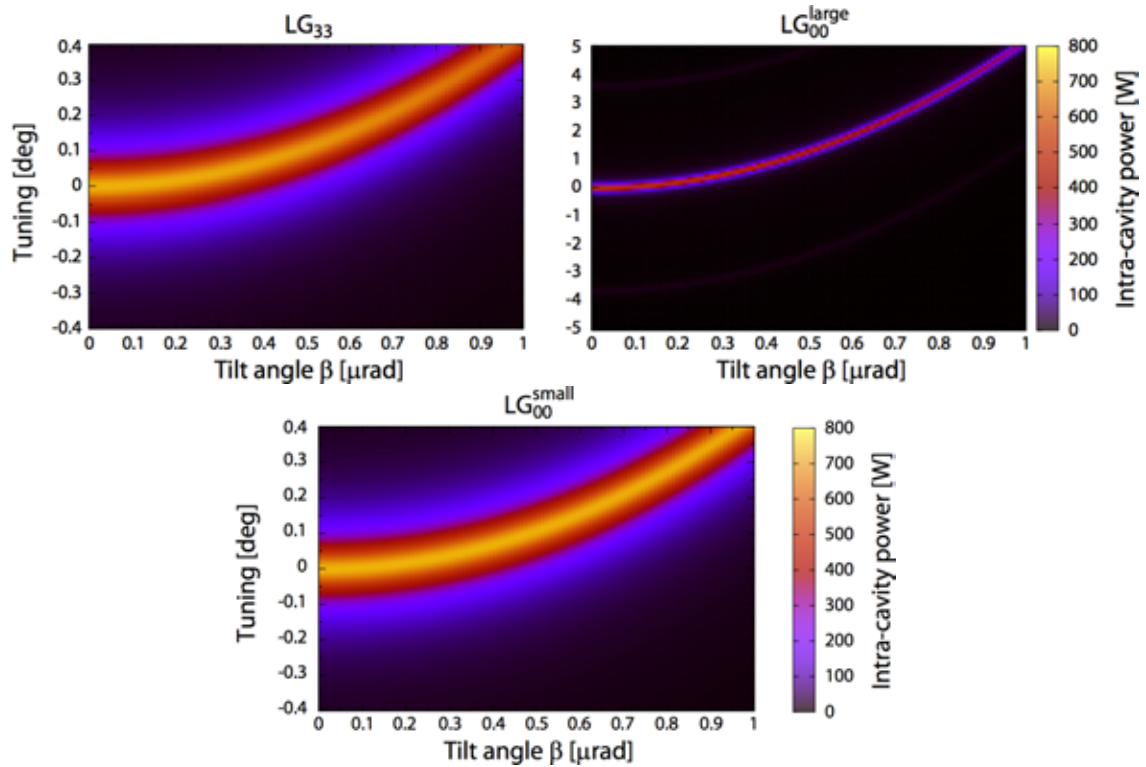


Figure 3.5.: Intra cavity power as a function of cavity end mirror tilt angle  $\beta$  and longitudinal tuning  $\phi$  for the three different configurations. The first two configurations show very similar results, but the  $LG_{00}^{\text{large}}$  configuration shows a much stronger coupling from tilt to tuning (note the larger scale on the tuning axis in the  $LG_{00}^{\text{large}}$  plot).

as shown in figure 3.6. Also plotted in figure 3.6 is a reference limit on the acceptable dark port power, around  $7.1 \times 10^{-9}$  W, calculated from a differential arm length requirement of  $10^{-15}$  m [AAB<sup>+</sup>] and a dark fringe offset of  $10^{-12}$  m [AdL07]. Comparing the  $LG_{33}$  and  $LG_{00}^{\text{large}}$  configurations, we can see that the  $LG_{33}$  configuration can tolerate larger differential misalignments before surpassing the reference limit. However, both  $LG_{33}$  and  $LG_{00}^{\text{large}}$  configurations are outperformed by the  $LG_{00}^{\text{small}}$  configuration in this investigation. This demonstrates that the coupling of differential arm cavity misalignment to dark port power depends both on the beam parameters and the beam shape.

The dependence on beam parameter and shape can be explained by considering the relative phase difference between the beams from the two arms across the overlapping region at the beam splitter. If the wavefronts of the two beams are not parallel, sinusoidal

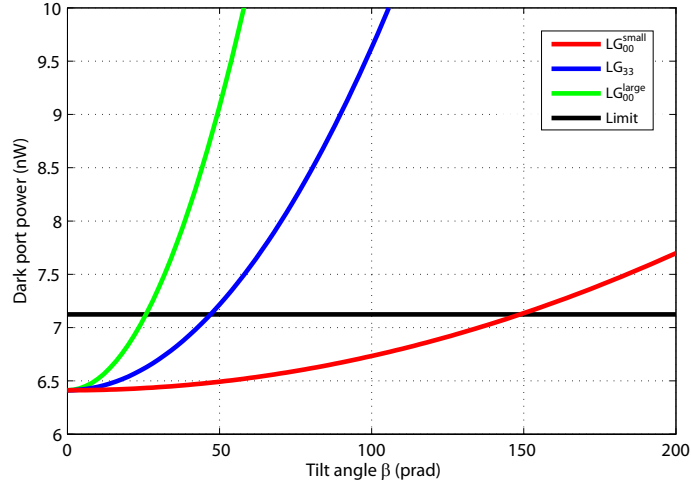


Figure 3.6.: Dark port power as a function of differential arm cavity misalignment for the three different configurations. The black line shows the limit calculated for dark port power based on a differential arm length requirement of  $10^{-15}$  m for a dark fringe offset of  $10^{-12}$  m.

fringes are formed with a spacing determined by the angle between the propagation vectors of the two beams<sup>4</sup>. The larger the overlapping region is, the larger the portion of the fringe that is within the overlapping region will be, and thus the less complete we should expect the interference to be. This effect depends on the true spatial extent of the beams at the overlapping region, which in turn depends on both the beam size parameter and the beam shape.

### 3.1.5. Coupling to unwanted modes due mode mismatch

Although mode matching is usually considered a technical detail rather than a fundamental concern, we found it worthwhile to compare the effects of mode mismatch into a cavity for the  $LG_{33}$  mode and the  $LG_{00}$  mode. This was partly in light of experimental observations that showed that the  $LG_{33}$  mode was more sensitive to mode mismatch in a cavity than the  $LG_{00}$ , such as those described in section 5.4.

Figure 3.7 shows the theoretical coupling into a range of mode orders caused by mismatch of the beam waist to the cavity waist, for both the  $LG_{00}$  mode and the  $LG_{33}$  mode in

<sup>4</sup>In the misalignment regime we are concerned with (100s of picoradians), the fringe spacing is of the order of km; far greater than the overlapping region of the beams.

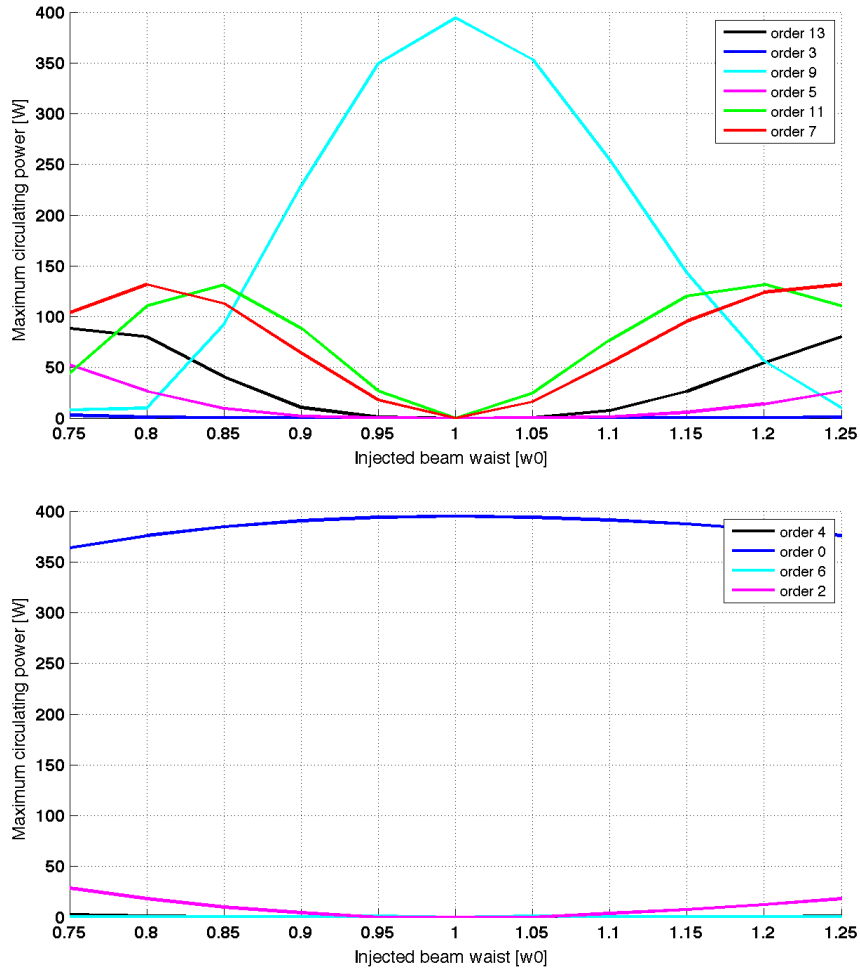


Figure 3.7.: Theoretical coupling of beam waist size mismatch to power in different mode orders. The upper plot shows the coupling for a  $LG_{33}$  input mode, and the lower plot shows the coupling for the  $LG_{00}$  input mode. Plots courtesy of Charlotte Bond.

a cavity similar to the Glasgow 10m cavity described in section 5.4. It is clear that the coupling is much stronger for the  $LG_{33}$  mode; when the injected waist is just 1.2 times the size of the cavity waist, the order 9 will no longer be the dominant mode order in the cavity. The  $LG_{33}$  mode also shows a stronger coupling into other modes when the injected waist position is mismatched to the cavity waist position. This increased susceptibility of the  $LG_{33}$  mode to mode mismatch is not likely to be a direct concern in terms of phase noise within a gravitational wave interferometer, but it should be borne

in mind as a practical consideration when determining acceptable tolerances in beam waist size and position mismatch.

### 3.1.6. Sensitivity improvements for Advanced Virgo

The final comparison between the performance of the LG<sub>00</sub> and LG<sub>33</sub> modes was in terms of the overall detector sensitivity. Several scenarios for using the LG<sub>33</sub> mode in the Advanced Virgo detector were evaluated, and published in [CHF09], but here we just discuss a scenario which compares the sensitivity of the detector with LG<sub>00</sub><sup>large</sup> and LG<sub>33</sub> modes. In each case the detector sensitivity was calculated using a version of Gravitational Wave Interferometer Noise Calculator [GWINC], specially adapted for Advanced Virgo, and the thermal noise scaling factors for the LG<sub>33</sub> mode shown in section 2.7.

Configuration	SR det. [Hz]	$\Gamma_{\text{NS/NS}}$ [Mpc]	$\Gamma_{\text{BH/BH}}$ [Mpc]
LG <sub>00</sub> <sup>large</sup>	750	126	900
LG <sub>33</sub>	750	148	1140
LG <sub>00</sub> <sup>large</sup>	300	130	580
LG <sub>33</sub>	300	163	715

Table 3.2.: Results of the GWINC calculation for detection ranges of two standard gravitational wave sources with the Advanced Virgo reference design, for both the LG<sub>00</sub><sup>large</sup> and LG<sub>33</sub> cavity configurations.

Table 3.2 shows the results of the calculation for the two cases NS/NS, and BH/BH, where the signal recycling detuning (SR det.) [HF07] was optimised for detection of signals from binary neutron star inspirals and binary black hole inspirals respectively. The figures of merit chosen were the effective detection ranges for the two signal sources,  $\Gamma_{\text{NS/NS}}$  and  $\Gamma_{\text{BH/BH}}$ . According to these results, the LG<sub>33</sub> mode provides a relative improvement of the inspiral ranges by around 20 % and 25 % for signal recycling detunings of 750 Hz and 300 Hz respectively, compared to the LG<sub>00</sub> mode. This corresponds to a potential increase by around a factor of 2 in the observable event rate for binary black hole and neutron star inspiral sources of the Advanced Virgo detector by using the LG<sub>33</sub> mode instead of the LG<sub>00</sub> mode. It is worth bearing in mind that while this constitutes a significant improvement in the detection prospects of Advanced Virgo, one would expect

the benefits to be even more pronounced in third generation interferometers, in which the levels of the other limiting noise sources should be significantly lower.

In summary, for all the interferometric performance aspects analysed, the  $LG_{33}$  configuration performs significantly better than the  $LG_{00}^{\text{large}}$  configuration which has the same clipping loss of 1 ppm on the Advanced Virgo cavity mirrors. For the longitudinal error signal generation with the PDH method, the alignment error signal generation using the Ward technique, and the coupling of cavity mirror tilt to phase, the beam shape had little or no effect on the result. In each of these cases the cavity geometry was shown to be the dominant factor in determining the performance, by comparing the  $LG_{33}$  configuration with the control configuration  $LG_{00}^{\text{small}}$ . In the case of differential arm cavity misalignment coupling to dark port power, both the beam shape and the beam size parameter were shown to influence the result. However, in this case the  $LG_{33}$  configuration still performed better than the  $LG_{00}^{\text{large}}$  configuration. It was also shown that an increase in the observable inspiral event rate by around a factor of two could be achieved by using the  $LG_{33}$  mode in place of the  $LG_{00}$  mode in the Advanced Virgo detector. The results of this study suggest that for the Advanced Virgo case, not only would using the  $LG_{33}$  mode improve the sensitivity of the detector, but it would also make the alignment sensing more achievable, as well as leading to less stringent alignment requirements than for the  $LG_{00}^{\text{large}}$  configuration. This result gave a very positive outlook for LG mode technology within gravitational wave detectors at this point, and so we proceeded with plans for a table-top demonstration of LG mode interferometry.

### **3.2. Numerical investigation into $LG_{33}$ beam generation by $LG_{00}$ phase profile modulation**

Before beginning a table-top demonstration of LG mode interferometry, it was necessary to develop our understanding of the various methods of generating higher-order LG modes. In this section I will briefly describe the work on higher-order LG mode production methods that had been previously described in the literature, and then describe a series of numerical investigations that were performed into a particular subset of these methods; those that achieve higher-order mode production by converting from the  $LG_{00}$  mode by modulating its phase profile. This study gave us a solid foundation upon which to begin the table-top experiments with higher-order LG modes that are

described in chapter 4.

### 3.2.1. Overview of previous work in Laguerre-Gauss beam production

Although at the time of starting my PhD studies the idea of using LG modes in gravitational wave detectors was relatively new, having been first described in print in 2006 [MTV06], LG modes had already been used in other research areas for at least 16 years. However, so far the optimization of higher-order LG beam sources has largely been in a different direction to that which is required by the gravitational wave detector community. For example the use of LG beams in the cold atoms and optics fields often requires high-speed manipulation of the beam parameters and positions, whereas the use of LG modes in high-precision interferometry depends on mode purity and stability. One of the leading candidate methods for the latter is the use of diffractive optic elements (DOEs), or *phase plates* for conversion from a  $LG_{00}$  mode to a higher-order LG mode, due to their stability, as well as potentially high conversion efficiency and output mode purity [BCKW94, TRS<sup>+</sup>96]. Other conversion methods include using computer generated holograms [ADAP98], spatial light modulators [MAI<sup>+</sup>08] and astigmatic mode converters [ABSW92, CP99]. However, none of these mode conversion methods are perfect, and some light inevitably remains in unwanted modes. A comparison of the merits and drawbacks of each method can be found in the paper [KST<sup>+</sup>02].

We decided that the LG mode production techniques that used phase profile modulation to convert from the  $LG_{00}$  mode to higher-order LG modes were the most suitable for our purposes. This is because there are two techniques which work in this way; the spatial light modulator (SLM) technique and the etched diffractive optical element (DOE) technique. These two techniques are complementary in that while the SLM method is adaptable but lacks stability and efficiency, the DOE method is stable and efficient, but lacks adaptability. Our plan was to use the SLM method at first, and then progress to the DOE method at a later stage once we had a phase profile design and conversion setup that fulfilled our requirements.

### 3.2.2. Phase modulation profile design

At the most basic level, the requirement for a phase modulation profile to convert a  $LG_{00}$  beam into a higher-order LG beam is to replicate the phase cross section of the

desired  $LG_{pl}$  mode. Replicating the amplitude cross section can be achieved to some extent using a phase modulating surface, as described later on in this section, but for now we will just discuss the replication of the phase cross section. We will consider the phase cross sections of arbitrary order  $LG_{pl}$  modes, for simplicity at the beam waist. In polar coordinates, the phase cross distribution  $P^{\sin}(r, \phi)_{pl}$  of the sinusoidal LG modes at the beam waist (i.e. where  $z=0$ ) is

$$P_{pl}^{\sin}(r, \phi) = \pi \left[ \Theta \left( L_p^{|l|} \left( \frac{2r^2}{w_0^2} \right) \right) + \Theta(\cos l\phi) \right], \quad (3.2)$$

and for helical LG modes

$$P_{pl}^{\text{hel}}(r, \phi) = \pi \Theta \left( L_p^{|l|} \left( \frac{2r^2}{w_0^2} \right) \right) + l\phi, \quad (3.3)$$

where  $w_0$  is the beam waist size, and  $\Theta$  is the Heaviside function. The function of a phase modulation profile is to imprint this desired phase cross section on the incident beam, which in our case is a  $LG_{00}$  beam. Two examples of such phase cross sections are shown in the left and right panels of figure 3.8, for converting to the sinusoidal and helical  $LG_{33}$  modes respectively.

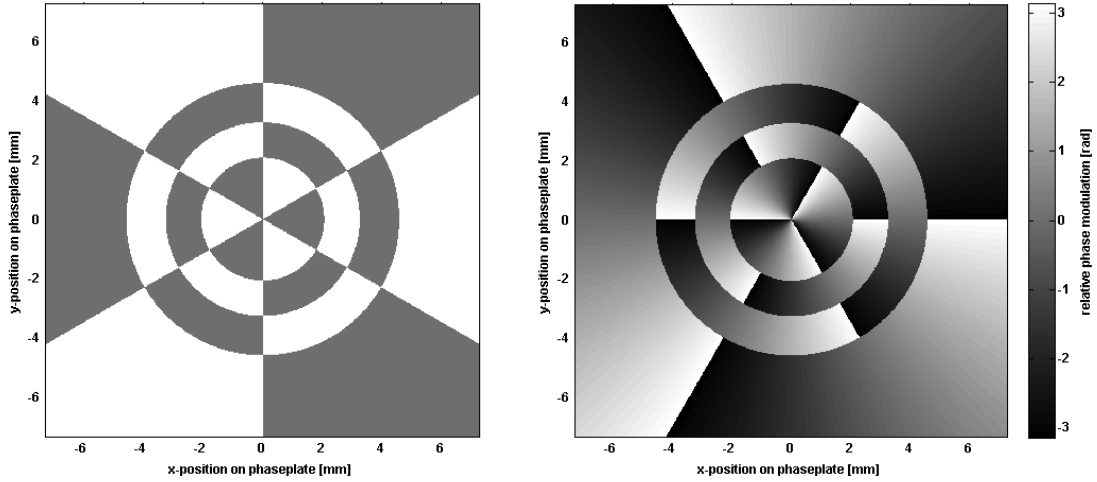


Figure 3.8.: Two phase modulation profiles of physical dimensions  $14.6 \times 14.6$  mm and  $768 \times 768$  pixels, created to convert a  $LG_{00}$  mode to a cosine  $LG_{33}$  mode (left panel) and a helical  $LG_{33}$  mode (right panel), each with a spot size at the phase modulating surface of  $w = 2$  mm.

### Blazed phase grating profile

When designing phase modulation profiles, it is useful to add a blazed grating phase pattern to the initially required phase profile, so as to spatially separate the modulated light from the light which remains unmodulated during the interaction with the phase modulating device. In the case of a reflective type SLM, this unmodulated component may be the result of direct reflection from the front surface of the SLM screen. In both SLMs and DOEs, some unmodulated light also results from the quantization of the phase levels [Sch]. Without adding a blazed grating, the unmodulated light propagates along the same axis as the modulated light, and can spoil the desired effects of the phase modulation profile on the incident beam. The use of blazed phase modulation profiles is commonplace in beam shaping applications, and was used for LG mode production with an SLM in the work reported in [MAI<sup>+</sup>08]. Figure 3.9 shows examples of blazed

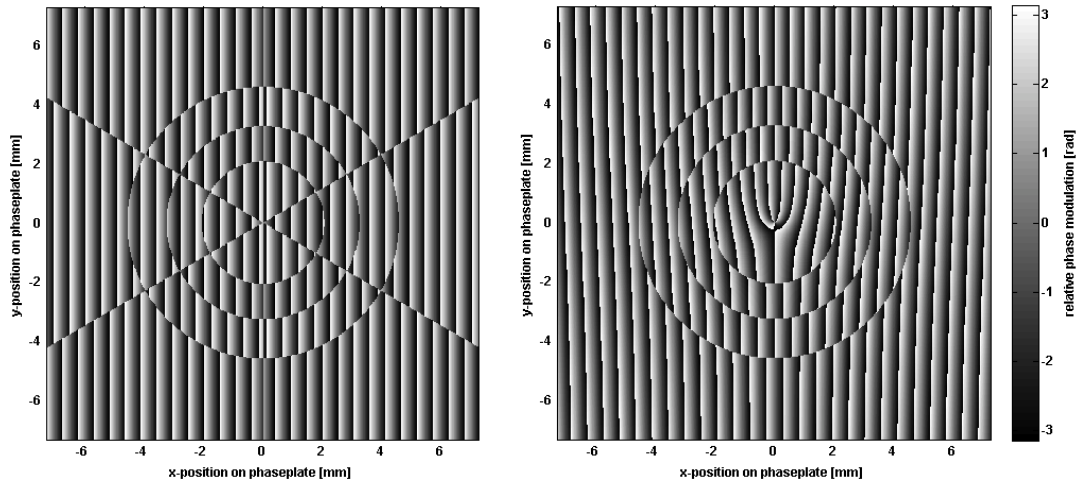


Figure 3.9.: Example of blazed phase modulation profiles for generating sinusoidal (left) and helical (right)  $LG_{33}$  modes.

phase profiles for converting the  $LG_{00}$  mode to both sinusoidal and helical  $LG_{33}$  modes. The blazed phase profile for the helical  $LG_{33}$  mode shows the ‘forked grating’ pattern that is often referred to in the literature concerning LG mode generation, as for example in [ADAP98], [JT08] and [BK08].

The blazing angle should be designed such that the diffraction angle into the first order is greater than the divergence angle of the beam. Most phase profile modulating devices,

whether SLMs or DOEs, will have some level of spatial discretisation. This discretisation will also produce diffraction orders, so one should take care to avoid an overlap of these orders with the first diffraction order from the blazed grating in order to achieve high purity in the desired diffraction order.

### Contoured blazing for intensity modulation

The use of a blazed phase grating to separate modulated light from unmodulated light also affords one the opportunity to achieve some amplitude modulation of the modulated beam, as well as phase modulation. This can be achieved by adjusting the amplitude of the blazing pattern to be proportional to the desired mode amplitude shape. The diffraction efficiency into parts of the output beam corresponding to the lower blazing amplitudes will be lower, hence providing the required amplitude modulation. In fact, this technique can also be used to correct for the inhomogeneous amplitude profile of the  $LG_{00}$  beam incident on the phase modulating surface, simply by dividing the amplitude of the blazing pattern by the  $LG_{00}$  amplitude profile. Figure 3.10 shows examples of

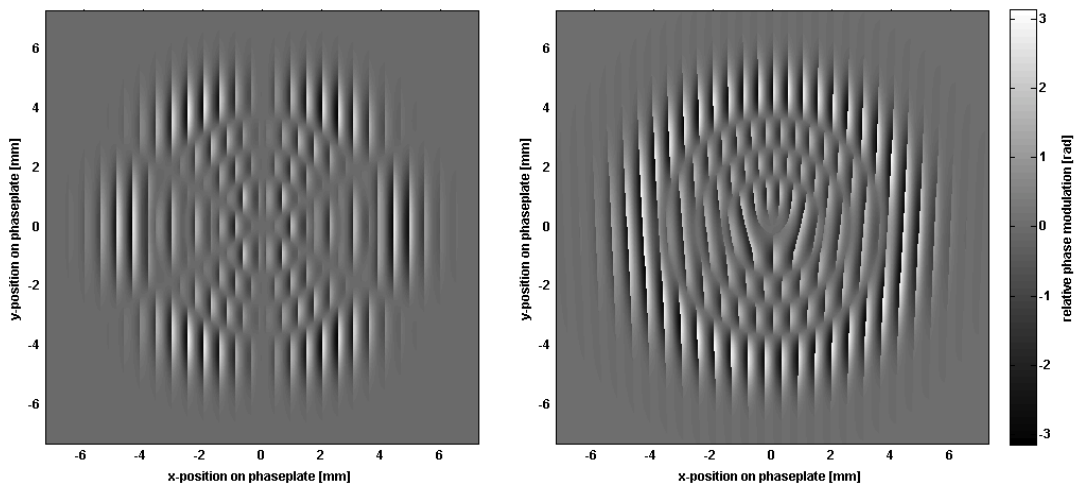


Figure 3.10.: Example of amplitude contoured blazed phase modulation profiles for generating sinusoidal (left) and helical (right)  $LG_{33}$  modes.

the amplitude contoured blazed phase modulation profiles for converting to both the sinusoidal and helical  $LG_{33}$  modes. It should be noted that though this technique can be used to increase the purity of the generated mode, in general it will reduce the overall

efficiency of conversion into the desired mode. Experimental results comparing the use of phase profiles with and without amplitude contouring are shown in sections 4.2.1 and 4.3.3.

### 3.2.3. Simulations of conversion from $LG_{00}$ beam to a $LG_{33}$ beam

To test the functionality of the phase modulation profiles it was necessary to simulate the beam conversion procedure. These simulations were performed in Matlab using a largely self developed package of scripts, in which the complex electric field amplitudes at every point in a grid are described with a matrix of complex numbers. The properties of the input  $LG_{00}$  beam and the phase modulation profile can be adjusted, and the properties of the resulting beam observed, thus enabling an optimisation of the conversion procedure to be carried out. The interaction of the input  $LG_{00}$  beam with the phase modulating is represented in the simulation as an element by element multiplication of the electric field complex amplitude matrix and the imaginary phase modulation profile matrix. In the simulation there is no requirement to use a blazed phase profile, since there is no unmodulated light after the interaction with the phase modulation profile. As a result, we used phase profiles like those shown in figure 3.8 for the conversion.

Subsequent to the interaction of the input  $LG_{00}$  with the phase modulation profile, the resulting field was propagated a distance of 3 m using a fast-Fourier transform (FFT) code developed successively by Vinet, Schilling and Freise. The details of this FFT code are described in [VVC01]. The final field intensity and phase were then plotted and compared to the field amplitude of an ideal  $LG_{33}$  mode in figure 3.11. The upper panels of figure 3.11 show that the intensity profile converted  $LG_{33}$  beam does share some features with that of the ideal  $LG_{33}$  mode; the 4 concentric rings are clearly visible. However, it is also clear that the outer rings are not as bright for the converted mode as in the ideal case. The phase profiles in the lower panel of figure 3.11 also show strong similarities between the ideal and converted mode; the three phase spirals and three radial phase dislocations are visible in both. However, the converted mode shows higher spatial frequency ‘ripple’ like features in the phase profile which are not present in the ideal mode. Plots of the amplitude and intensity of both  $LG_{33}$  fields for a cross section through the optic axis can be seen in figure 3.12. The intensity cross section highlights the fact that the outer rings of the converted mode are less bright than the ideal mode. This feature is likely to be a result of the inhomogeneous intensity distribution of the

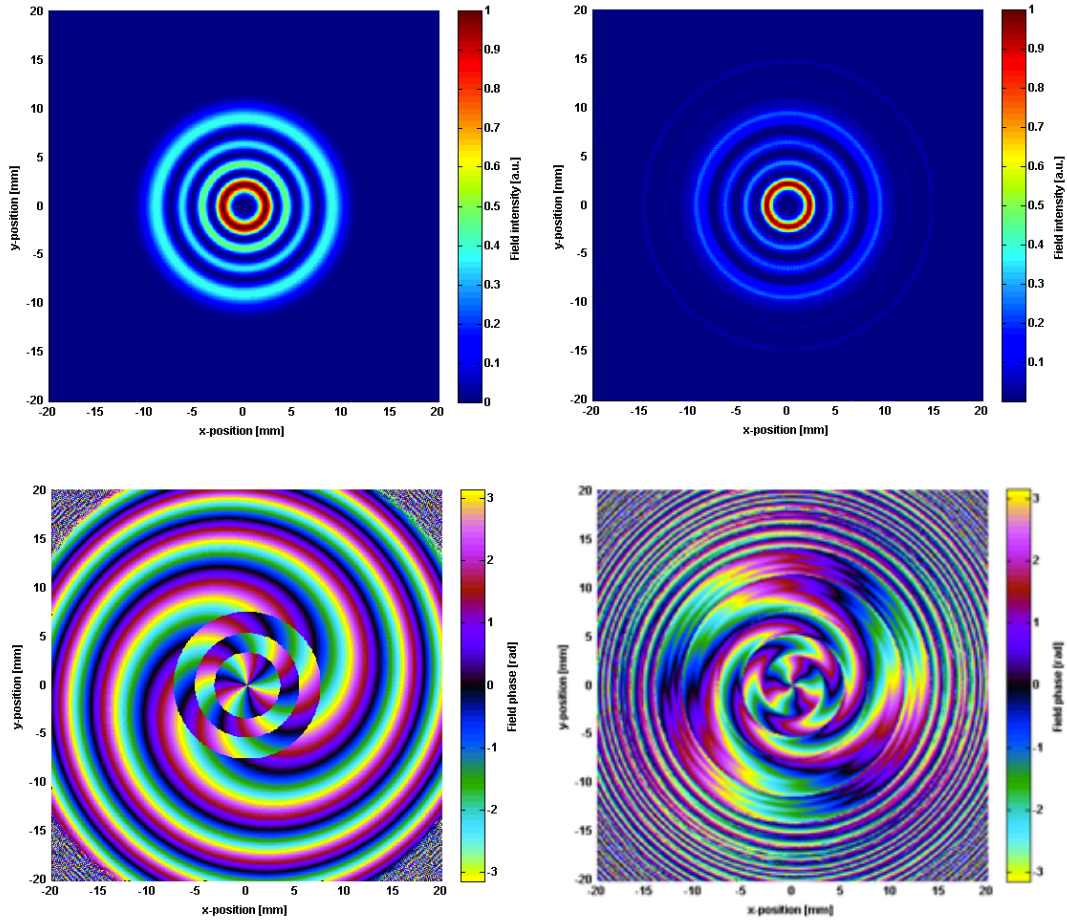


Figure 3.11.: Intensity (top) and phase (bottom) profiles of an ideal helical  $LG_{33}$  mode (left) and a helical  $LG_{33}$  mode generated by interaction of a  $LG_{00}$  with the phase modulation profile shown in figure 3.8 (right).

input  $LG_{00}$  mode over the phase modulation profile, resulting in lower light amplitudes interacting with the outer regions of the profile. This can be improved by employing the amplitude contouring technique described in section 3.2.2.

### 3.2.4. Converted beam parameter estimation

A useful figure of merit for the performance of a phase modulation profile is the purity of the generated  $LG$  mode after interaction with the phase modulation profile. We calculate the mode purity as the squared inner product of the normalised converted

### 3.2. Numerical investigation into $LG_{33}$ beam generation by $LG_{00}$ phase profile modulation

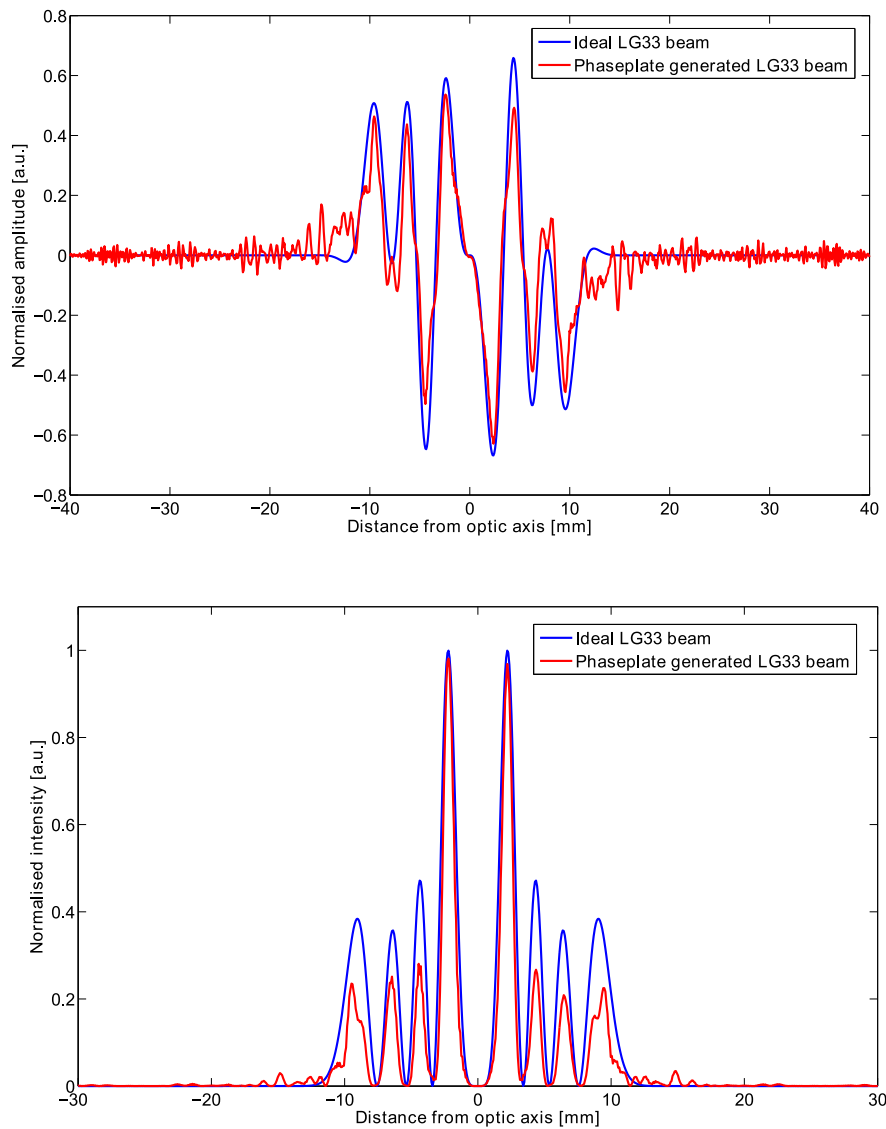


Figure 3.12.: The normalised amplitude (top) and intensity (bottom) for cross sections through the optic axis of the simulated converted  $LG_{33}$  beam and the ideal  $LG_{33}$  beam. The amplitude plot shows higher spatial frequency noise present in the simulated converted beam. It can be seen from the intensity plot that the outer rings of the simulated converted beam contain a lower proportion of the beam power than in the ideal  $LG_{33}$  beam case.

$LG_{33}$  field amplitude and the ideal  $LG_{33}$  field amplitude. This gives a measure of the fraction of power in the converted field which is in the correct mode. This power fraction is referred to as the mode purity in [MAI<sup>+</sup>08] and [CACD98], and so the same definition is used in this work.

When performing the inner product the beam parameters of the ideal mode used as the reference will affect the outcome, since even for two ideal modes, different beam sizes or curvatures will give a lower purity result than 100%. Choosing the beam parameters of the ideal  $LG_{33}$  mode in the inner product amounts to choosing a basis for the modal description (see section 2.5). In order to calculate the true purity of the converted mode, one is required to choose the basis in which the inner product between the two fields is maximal.

For this reason it was necessary to investigate the effect of the phase modulation profile on the waist size and position parameters,  $w_0$  and  $z_0$  of the beam interacting with it. Without a proper understanding of the change of these beam parameters upon conversion, it would not be possible to choose the correct beam parameters for the ideal  $LG_{33}$  mode in the calculation of mode purity, and the result of the inner product would give an underestimate for the purity of the converted mode. In this section we extend the mode conversion procedure analysis to include the possibility that the phase modulating surface is not located at the input beam waist position. The phase modulation profile is still designed with no phase curvature term however, as in equations 3.2 and 3.3.

We expected that the dimensions of the phase modulation profile primarily determine the beam *size* of the output beam, but that the beam *phase front curvature* is unchanged during interaction with the phase modulating surface. The expectation that the phase modulation profile determines the beam size stems from the fact that it is this profile that determines where the nodes in intensity of the converted field are positioned. For a higher-order  $LG_{33}$  mode, it seems clear that the spacing of the radial rings is one of the main indicators of the beam size parameter. Our expectation that the phase front radius of curvature remains unchanged simply stems from the fact that we could see no physical reason for why this curvature should change upon interaction with the phase modulating surface in the absence of any curvature inherent in the surface itself.

The expected resulting beam waist size  $w_0$  and position  $z$  after interaction with the phase modulation profile can be calculated for any set of input beam parameters. We can rearrange the well known relations for Gaussian beams to give the more fundamental

beam parameters  $w_0$  and  $z$  as functions of the known beam radius curvature  $R_C$  and beam spot size  $w$  parameters. Starting with the equation for beam radius of curvature as a function of position along the optical axis  $z$  and the Rayleigh range of the beam  $z_R$  [FS10]

$$R_C(z) = z + \left( \frac{z_R^2}{z} \right), \quad (3.4)$$

we rearrange to get

$$z_R^2 + z^2 = R_C(z) z. \quad (3.5)$$

The equation for the beam spot size  $w(z)$  in terms of the beam waist size  $w_0$ , the Rayleigh range and the distance to the beam waist is

$$w(z) = w_0 \sqrt{1 + \frac{z^2}{z_R^2}}. \quad (3.6)$$

The Rayleigh range is related to the beam waist size and the wavelength by the following equation;

$$z_R = \frac{w_0^2 \pi}{\lambda} \quad (3.7)$$

Rearranging this gives

$$w_0 = \sqrt{\frac{z_R \lambda}{\pi}}. \quad (3.8)$$

Substituting this expression for  $w_0$  into equation 3.6 gives

$$w(z) = \sqrt{\frac{z_R \lambda}{\pi} \left( 1 + \frac{z^2}{z_R^2} \right)} = \sqrt{\frac{\lambda}{\pi} \left( z_R + \frac{z^2}{z_R} \right)}. \quad (3.9)$$

Squaring both sides, multiplying through by  $z_R$  and rearranging gives

$$z_R^2 + z^2 = \frac{z_R w(z)^2 \pi}{\lambda}. \quad (3.10)$$

Now we can substitute the expression for  $z_R^2 + z^2$  from equation 3.5 to obtain

$$R_C(z) z = \frac{z_R w(z)^2 \pi}{\lambda}. \quad (3.11)$$

Rearranging for  $z$ , squaring both sides and substituting the result for  $z_R^2$  acquired from equation 3.5 gives

$$z^2 = \frac{(R_C(z) z - z^2)(w(z)^2 \pi)^2}{(R_C(z) \lambda)^2}. \quad (3.12)$$

Collecting  $z^2$  terms on one side of the equation gives

$$z^2 \left( 1 + \left( \frac{w(z)^2 \pi}{R_C(z) \lambda} \right)^2 \right) = \frac{z (w(z)^2 \pi)^2}{R_C(z) \lambda^2}. \quad (3.13)$$

Now dividing both sides by  $z$ , rearranging for  $z$  and tidying a bit gives

$$z = \frac{\left( \frac{w(z)^2 \pi}{\lambda} \right)^2 R_C(z)}{R_C(z)^2 + \left( \frac{w(z)^2 \pi}{\lambda} \right)^2}. \quad (3.14)$$

If we define the parameter  $\Upsilon(z)$  as follows

$$\Upsilon(z) = \left( \frac{w(z)^2 \pi}{\lambda} \right)^2 \quad (3.15)$$

we can write equation 3.14 in a more visibly intuitive manner;

$$z = \frac{\Upsilon(z) R_C(z)}{R_C(z)^2 + \Upsilon(z)}. \quad (3.16)$$

The beam waist size can now be found in terms of the radius of curvature and beam spot size at a given point along the x-axis and the distance to the beam waist, or even in terms only of the radius of curvature and beam spot size at a given point along the x-axis. Starting by substituting the result for  $z$  from equation 3.14 into equation 3.5 we get

$$z_R^2 = \frac{R_C(z)^2 \Upsilon(z)}{R_C(z)^2 + \Upsilon(z)} - \frac{R_C(z)^2 \Upsilon(z)^2}{(R_C(z)^2 + \Upsilon(z))^2}. \quad (3.17)$$

Factorising the right hand side gives

$$z_R^2 = \frac{R_C(z)^2 \Upsilon(z)}{R_C(z)^2 + \Upsilon(z)} \left( 1 - \frac{\Upsilon(z)}{R_C(z)^2 + \Upsilon(z)} \right). \quad (3.18)$$

Substituting for  $z_R$  from equation 3.7 dividing both sides by  $\left(\frac{\pi}{\lambda}\right)^2$  and taking the fourth root of both sides gives

$$w_0 = \left[ \frac{R_C(z)^2 w(z)^4}{R_C(z)^2 + \Upsilon(z)} \left( 1 - \frac{\Upsilon(z)}{R_C(z)^2 + \Upsilon(z)} \right) \right]^{\frac{1}{4}}. \quad (3.19)$$

The expression for  $z$  and  $w_0$  can be simplified further, and are given here in their final form;

$$z = \frac{R_c}{\left(\frac{\lambda R_c}{w^2 \pi}\right)^2 + 1} \quad (3.20)$$

$$w_0 = \frac{w^2}{1 + \frac{w^4 \pi^2}{R_c^2 \lambda^2}} \left[ 1 - \left( \frac{R_c^2}{\lambda} + 1 \right)^{-1} \right]^{\frac{1}{4}}. \quad (3.21)$$

The accuracy of predictions based on our expectations about the beam parameter change upon mode conversion by was tested comparing the calculated beam parameters with FFT simulation results. In the simulation, the converted beam parameters were estimated by fitting the beam parameters of the ideal LG<sub>33</sub> mode such as to maximise the overlap integral between the converted beam and the ideal LG<sub>33</sub> beam. The ideal LG<sub>33</sub> parameters which give the best mode purity result for the converted beam, calculated in the manner previously described, are the best approximation to the beam parameters of the converted beam itself. This procedure was performed for a range of different input beam waist sizes and curvatures, and then compared with the calculated theoretical beam parameters.

Figure 3.13 shows the theoretical results for generated beam waist size and position compared to the numerical results from the simulation. For each of the 10 different input beam waist sizes and each of the 10 different beam waist positions investigated numerically, the theoretical and numerical results agree very well. We therefore conclude that our aforementioned theory is sound for the purposes of estimating post-conversion beam parameters.

### 3.2.5. Optimum conversion beam size ratio

Since the beam waist size  $w_0$  appears in the phase cross section equations 3.3 and 3.2, it is clear that a given phase modulation profile will be optimized to give a particular output LG<sub>33</sub> beam size. However, since the higher-order LG modes are more spatially extended than the LG<sub>00</sub> mode, one expects that the incident LG<sub>00</sub> beam should have a larger beam size in order to actually interact optimally with the phase modulation profile. We therefore performed a study using FFT simulations to find the optimum ratio of input LG<sub>00</sub> beam size to phase image beam size for a range of different LG<sub>pl</sub> modes.

Figure 3.14 shows the results of this investigation for conversion to the helical LG<sub>33</sub> mode, where the conversion procedure was simulated for the same input beam size, but each time with a different phase image size. The phase modulating surface was always

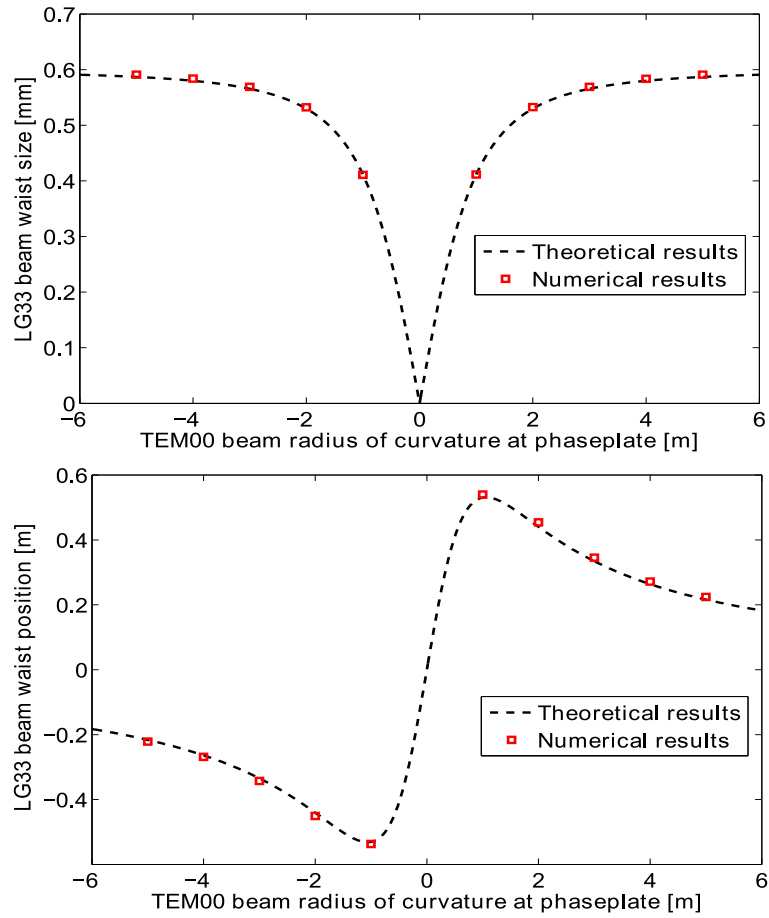


Figure 3.13.: Plotted in the upper panel are the waist sizes of the best-fit ideal  $LG_{33}$  mode for a simulated phase-plate generated  $LG_{33}$  beam for ten different input  $LG_{00}$  beam curvatures. For comparison, the theoretical prediction for the waist size of the generated  $LG_{33}$  mode is also plotted. The best-fit and theoretical waist positions are similarly plotted in the lower panel. A clear agreement between the best-fit results and the theoretical trend is observed in both plots.

located at the beam waist for simplicity. In this case the optimum ratio of input beam size to converted beam size was found to be around 3. Table 3.3 shows this optimum ratio for generating all  $LG_{pl}$  beams up to and including order 9.

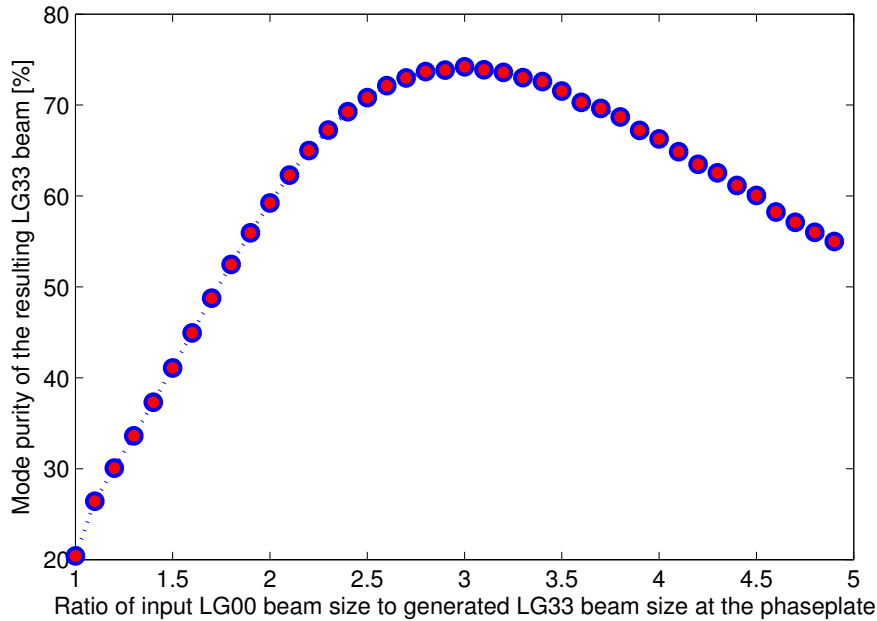


Figure 3.14.: Simulated converted  $LG_{33}$  mode purity as a function of the ratio between input  $LG_{00}$  beam size and  $LG_{33}$  phase modulation profile beam size. The maximum mode purity is achieved when the input beam size is around a factor of 3 larger than the phase modulation profile beam size.

### 3.2.6. Theoretical purities of generated LG modes

The squared inner product of the normalised phaseplate generated  $LG_{33}$  field amplitude and ideal  $LG_{33}$  field amplitude gives a measure of the amount of power in the phaseplate generated field which is in the correct mode, a figure of merit known as the mode purity [MAI+08, CACD98]. For the helical  $LG_{33}$  mode conversion simulation, 74.16% of the power in the converted  $LG_{33}$  field was in the  $LG_{33}$  mode. The same simulation was performed for the sinusoidal  $LG_{33}$  mode conversion, in which we found that 60.13% of the power was in the correct mode.

We believed that some of the power remained in other modes as a result of the limitation of phase only modulation. To test whether or not this was the case we added an amplitude modulating ‘mask’ to the simulation, at the same position as the phase modulating surface. The profile of the mask was based on the ideas described in section 3.2.2, in the context of contoured blazing for amplitude modulation. Figure 3.15 shows the transmission profile mask for both the helical and sinusoidal cases. The amplitude

4	2.9	3.0								
3	2.5	2.7	2.8	3.0						
2	2.2	2.4	2.5	2.7	2.9	3.0				
1	1.7	2.0	2.2	2.4	2.6	2.8	2.9	3.1		
0	1.0	1.4	1.7	2.0	2.2	2.5	2.6	2.8	3.0	3.2
$\frac{p}{l}$	0	1	2	3	4	5	6	7	8	9

Table 3.3.: Optimum ratio between input  $LG_{00}$  beam size and  $LG_{pl}$  phase image beam size, for LG modes up to the order 9.

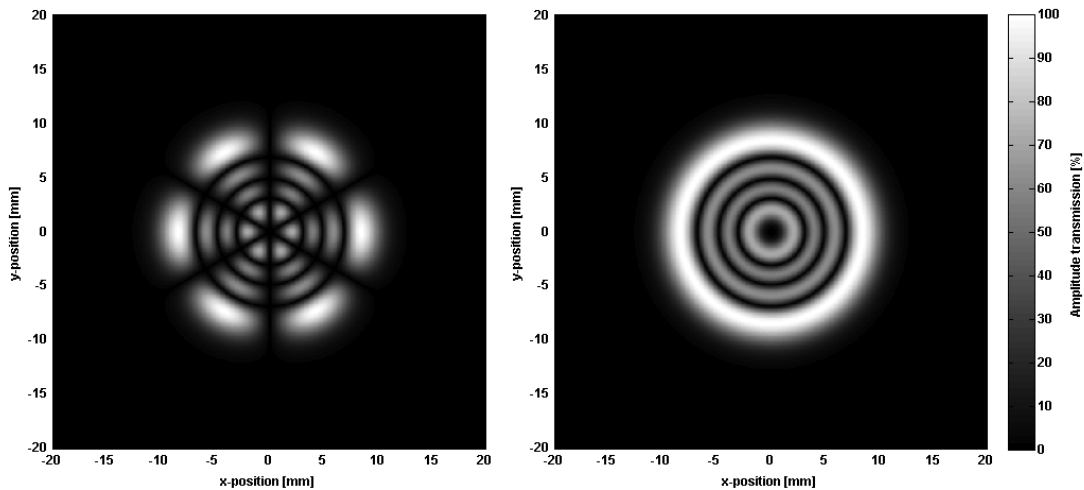


Figure 3.15.: Amplitude transmission masks for the sinusoidal (left) and helical (right)  $LG_{33}$  modes, as used in simulations of the beam conversion procedure.

transmission profiles were calculated simply by dividing the normalised amplitude profile of the  $LG_{33}$  beam to be generated by the normalised amplitude profile of the incident  $LG_{00}$  beam.

Using these amplitude masks, the converted beam purity was now found to be 100 % in both helical and sinusoidal cases. This confirmed our belief that the limitation of phase only modulation was responsible for the beam power not converted into the  $LG_{33}$  mode. It also showed that it should theoretically be possible to achieve 100 % purity in the converted mode if both phase and amplitude modulation are applied. In reality however, technical limitations in the equipment mean that such high purities are unlikely

### 3.2. Numerical investigation into $LG_{33}$ beam generation by $LG_{00}$ phase profile modulation

to be achievable directly from a phase and amplitude modulator, or a phase modulator used with a contoured blazing profile, in the laboratory.



## Chapter 4.

# Tabletop demonstrations of LG mode production and cleaning

With an improved understanding of the principles of mode conversion using a phase modulating surface, we proceeded with experimental table-top demonstrations of LG mode generation and interferometry. For the table-top experiments, we decided to use a computer-controlled liquid-crystal-on-silicon spatial light modulator (LCoS SLM) for preparing the LG beams. We found this to be the best choice for our work because of the availability and adaptability of such devices. We could easily alter the phase profile imprinted on the beam to be converted, and thus try many different profiles for conversion. At this relatively early stage in the experimental investigations, this advantage was deemed to outweigh the disadvantages of the SLM generation method; namely low mode conversion efficiency and phase front stability. Although, for example an etched diffractive optic would offer better stability and conversion efficiency, there is no possibility to alter the design once the optic is manufactured. At this time our goal was not to find the optimal the conversion method, but rather to investigate the interferometric performance of LG<sub>33</sub> beams.

In this chapter I will first describe the procedure used to determine the phase modulation characteristics of the SLM for 1064 nm light, and then describe the results we obtained using the SLM to generate higher-order LG modes. The rest of the chapter describes the experiments we performed with the helical and sinusoidal modes that were generated, aimed at verifying some of the results of the simulation study described in section 3.1. As part of this work, we demonstrated the first feedback control of an optical cavity pumped with a higher-order LG mode, and showed that the LG<sub>33</sub> mode transmitted through the cavity on resonance had a strongly enhanced mode purity when compared

with the input mode. These results, along with our demonstration of the incompatibility of helical LG modes with triangular cavities, were published in [FKCF10].

## 4.1. Characterising the spatial light modulator

For initial table-top experiments with higher-order LG modes, our method of choice for generating the modes was to use a SLM. The SLM we used was a Holoeye LCR-2500 liquid-crystal on silicon reflective type [OKS06] model, with a  $1024 \times 768$  resolution on a  $14.6 \text{ mm} \times 19.6 \text{ mm}$  active area. Figure 4.1 shows the SLM set up on the optical table.

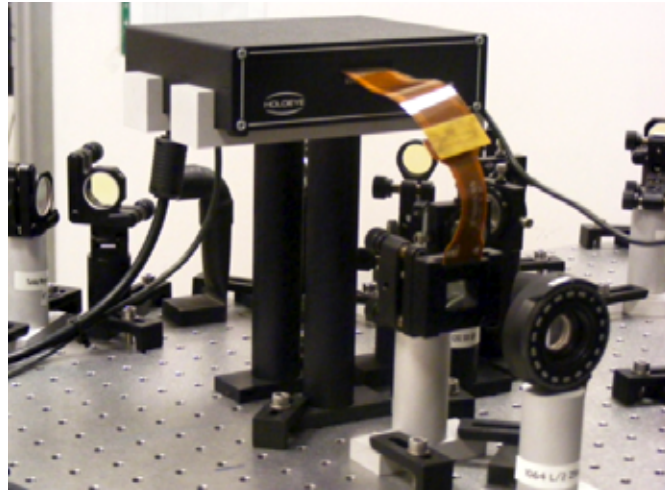


Figure 4.1.: The Holoeye LCR-2500 liquid crystal on silicon spatial light modulator device. The control box is provided with the desired phase modulation profile by a PC, via a DVI cable. The modulating surface of the SLM is mounted in a 3-axis kinematic mount, and connected to the control box by orange ribbon cable.

Before using the SLM for the generation of higher-order LG modes, it was necessary to characterise the device. Many of the device's specifications were provided by the manufacturer, but the modulation index for 1064 nm light is not given, since the device was primarily designed for wavelengths in the range from 400-700 nm. The device is operated remotely by PC via a DVI connection; a very convenient method as the SLM can be addressed by the PC in exactly the same way as a second monitor. The desired phase profile is transmitted via DVI cable to the SLM control box as a greyscale image.

The control box converts the greyscale values for each pixel in the image to a specific voltage value, which is then applied to the corresponding pixel on the phase modulating optical component of the SLM, referred to as the SLM head or display. The phase modulation depth of pixels within the SLM display is determined by the voltage, and thus the SLM displays the phase profile supplied in the original image from the PC.

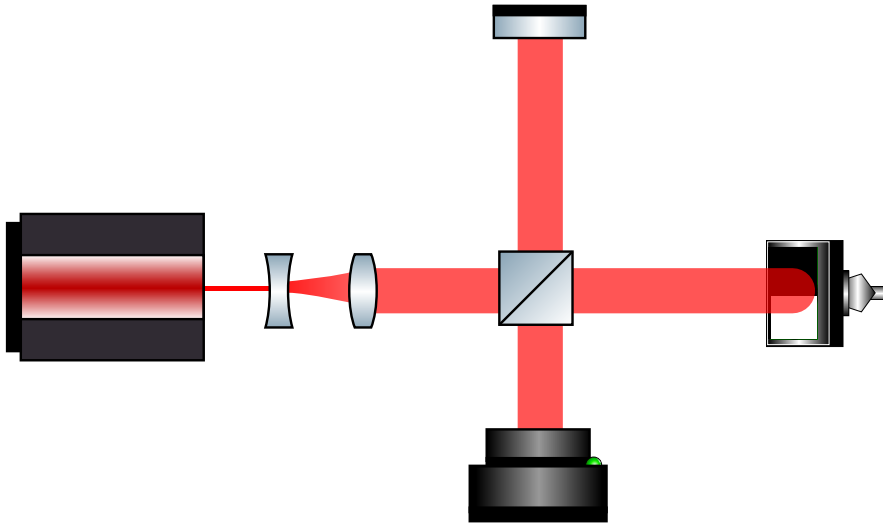


Figure 4.2.: The optical layout for characterising the SLM. A simple Michelson design is used with an expanded beam, where the SLM forms one of the end mirrors. The arms are misaligned in the vertical axis to produce a horizontal fringe pattern at the anti-symmetric port. The greyscale value applied to one half of the SLM is then varied, while the other half remains constant. The fringe pattern is recorded using a CCD camera, and the data are subsequently processed to recover the phase modulation depth at each greyscale value.

For most uses of SLMs it is necessary to use a look up table to convert accurately from greyscale values to the driving voltage which it applies to the liquid crystal cells in order to achieve the desired phase modulation. The data from such a table is often referred to as a ‘gamma curve’, because of its analogous function to the gamma correction used in image processing. In the absence of manufacturer data for the gamma curve at 1064 nm, it was necessary to ascertain it by means of measurement in the lab. Several methods for characterising the phase modulation properties of SLMs have been reported in the literature previously, such as in [MAI<sup>+</sup>08], and [MCJV97]. We decided to use a method similar to that used in [MCJV97], as it seemed the more straight-forward of the

two methods and we did not expect to require the full pixel-by-pixel characterisation obtained from the other method.

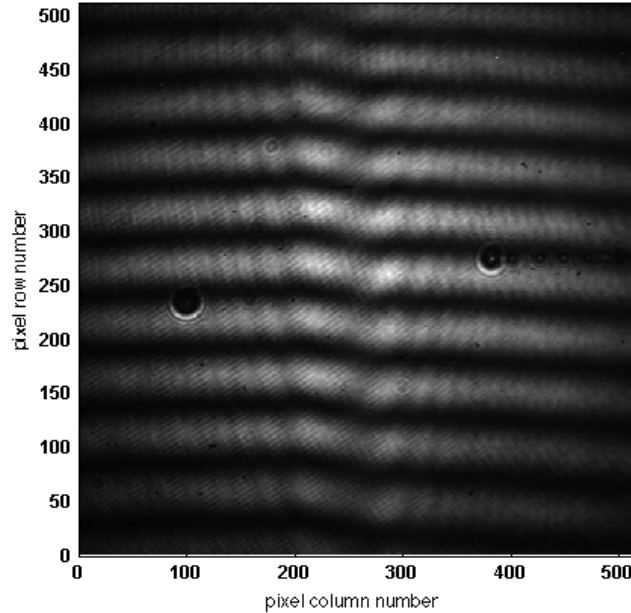


Figure 4.3.: The measured fringe pattern from the setup shown in figure 4.2, when a greyscale level of 200 was applied to one half of the SLM. The right hand side of the fringe pattern is the side which corresponds to light reflected from the modulated half of the SLM.

The setup for measuring the phase modulation characteristics of the SLM is shown in figure 4.2. An expanded beam is used as the readout beam for a Michelson interferometer, where one of the end mirrors is formed by the reflective surface of the SLM. Horizontal interference fringes were formed at the anti-symmetric port by misaligning the arms along the vertical axis. The relative position of the bright and dark fringes is dependent on the phase difference between light from the two arms of the interferometer. By changing the greyscale value applied to one half of the SLM, we can observe the change in the relative position of the fringe pattern which corresponds to light reflected from that half of the SLM, and recover the phase modulation depth that this light experiences on reflection from the SLM. The fringe pattern corresponding to the unmodulated half of the SLM serves as a reference, and avoids false interpretation of drifts of the Michelson as phase changes caused by the SLM.

The fringe pattern at the anti-symmetric port was recorded for 27 different grayscale levels applied to one half of the SLM only, using a CCD camera. An example of one such image is shown in figure 4.3. From each such image, one column of pixels was then selected for each of the modulated and unmodulated side of the beam. The intensity variation over these columns was then fitted via a sinusoidal function with a Gaussian envelope:

$$I(x) = A \exp(-x^2/\sigma^2) [\sin(\omega x + \phi) + C]. \quad (4.1)$$

The difference between the fitted phase  $\phi$  of the SLM modulated and unmodulated sides of the fringe pattern was then calculated. Once any initial phase offset between the two sides of the fringe pattern is subtracted off, this phase difference gives the phase modulation of the SLM for that particular greyscale value. An example of the fits for the left and right sides of the CCD data shown in figure 4.3 can be seen in figure 4.4.

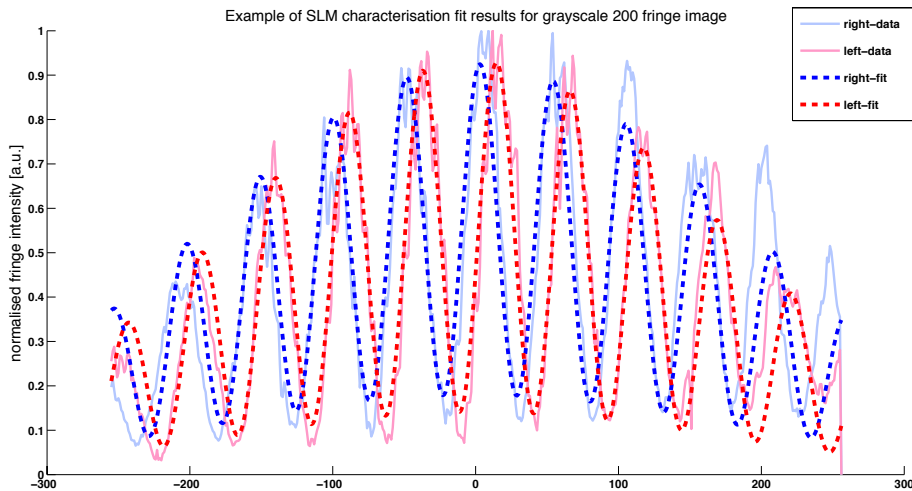


Figure 4.4.: Results of fitting equation 4.1 to the data from columns of pixels from the left and right sides of the CCD image shown in figure 4.3. This step was repeated for 27 different grayscale values, and the fitted phase differences between the left and right sides were used to generate the calibration curve shown in figure 4.5.

A plot of the recovered phase modulation as a function of applied greyscale level is shown in figure 4.5. It is clear from this plot that the SLM is not capable of producing a

$2\pi$  phase modulation in light reflected from its surface. In fact, the maximum achievable modulation is around 2.3. This makes the use of the SLM sub-optimal for generating higher-order LG modes, for two main reasons; Firstly, it is not possible to achieve the optimal diffraction efficiency into the first order from the blazed phase grating profile with a phase depth of less than  $2\pi$ . Secondly, one expects that since the generated phase profile is required to cycle from 0 to  $2\pi$  a total of  $l$  times over the azimuthal coordinate to produce a  $\text{LG}_{pl}$  mode (see section 3.2.2), a modulation depth less than  $2\pi$  should be insufficient to generate such modes. In practice, however, we found that the SLM was capable of producing the helical phase front of higher-order LG modes when used in the first order blazed grating configuration.

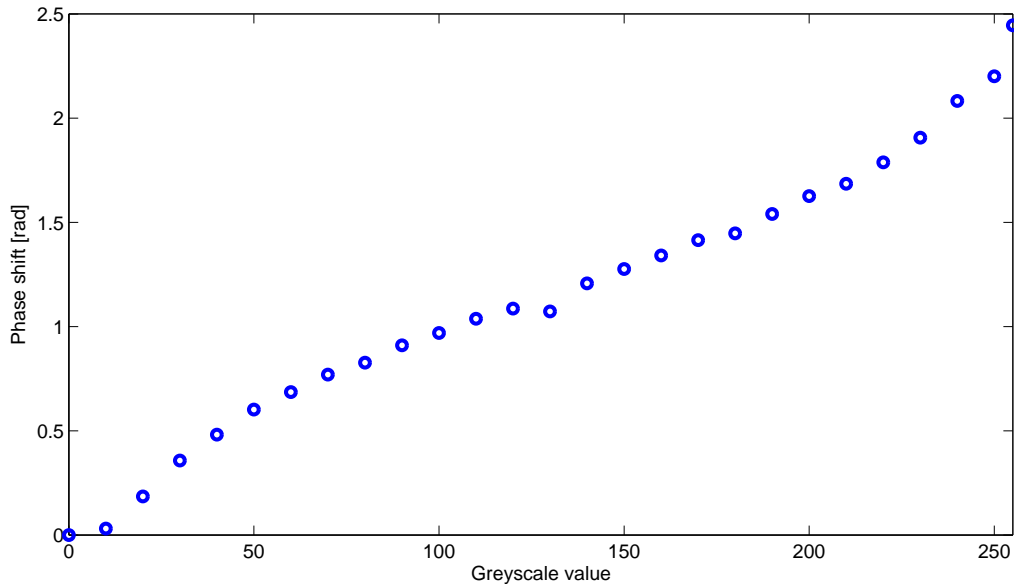


Figure 4.5.: Measured phase modulation from the LCR-2500 SLM as a function of applied grayscale value. Aside from the one anomalous point, the plot shows a similar trend to those of the manufacturer provided ‘gamma curves’ for shorter wavelengths. The main difference for the 1064 nm case is that the maximum phase modulation depth is less than  $\pi$ , as opposed to the  $2\pi$  for which the device is rated up to 700 nm wavelengths.

## 4.2. Higher-order LG modes generated using a spatial light modulator

Presented in this section are the method and results of the table-top LG mode generation procedure. The SLM was used in the configuration shown in figure 4.6 to generate a range of both helical and sinusoidal LG modes. In this section I will discuss the recorded intensity profiles of the  $LG_{pl}$  beams generated in this way, as well as interferometric measurements made in order to probe the actual phase profile of the generated beams. Also discussed in this section is the effect of the blazing angle added to the LG mode conversion profile, as discussed in section 3.2.2 on the diffraction pattern obtained.

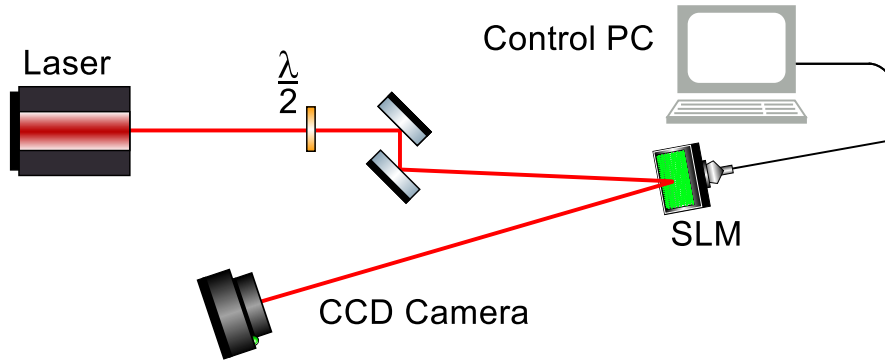


Figure 4.6.: Initial setup for generating and observing LG modes with the SLM.

The estimation of mode purities achieved with this conversion method required the use of a more complicated setup involving a linear mode cleaner. Since this procedure was intimately related to the experimental investigation of the interferometric performance of higher-order LG modes, I present the procedure and the results obtained later in section 4.3.3.

### 4.2.1. Mode conversion results

The SLM was used in the experimental setup as shown in figure 4.6 to perform conversions from the  $LG_{00}$  mode to a number of higher-order LG modes. The  $LG_{00}$  beam was steered onto the SLM under an angle close to the SLM surface normal. It is important that the incident beam is as close to the SLM surface normal as possible, since under non-zero incident angles the projection of the  $LG_{00}$  beam onto the SLM surface will

cause ellipticity in the diffracted beam. A blazing angle of  $0.083^\circ$  was added to the basic phase modulation profiles in order to spatially separate the unmodulated light from the modulated light. The input  $LG_{00}$  beam size at the SLM display was measured to be 1.26 mm, and the beam size ratios from table 3.3 obtained from the simulation study were used to scale the phase modulation profile appropriately for the generation of different higher-order LG modes.

Figure 4.7 shows the helical modes up to  $LG_{33}$  that were generated in this way. The lower and upper panels show the modes generated using phase images that respectively did, and did not include the amplitude modulation described in section 3.2.2. The intensity profiles shown in figure 4.7 show a good resemblance to the theoretical intensity profiles for LG modes shown in figure 2.5. Comparing the amplitude modulated and unmodulated cases, we can see that diffraction rings are visible outside the last ring of the LG beam for many of the modes in the amplitude unmodulated case, but are not visible for the amplitude modulated case. However, we can observe ripple-like interference fringes on the right side of the beams in the amplitude modulated case. This is due to the influence of the zero order beam, which had a greater effect in the amplitude modulated case because the LG beam powers were significantly lower.

The diffraction efficiencies for both the amplitude modulated and unmodulated cases were measured by comparing the light power incident on the SLM to the light power present in the 1st diffraction order. This measurement was made when the SLM was displaying the phase profile for conversion to the  $LG_{33}$  mode. For the sinusoidal  $LG_{33}$ , the non-amplitude contoured diffraction efficiency was 16.4%, and the amplitude contoured diffraction efficiency was just 1.83%. For the helical  $LG_{33}$  case, the non-amplitude contoured diffraction efficiency was 15.56%, and the amplitude contoured diffraction efficiency was 3.81%.

All of these diffraction efficiencies are very low for a blazed grating profile. The low efficiency in the non-amplitude modulated case is likely to be mainly a result of the limited phase modulation depth of less than  $\pi$ , as well as the loss of light from the first diffraction order due to direct reflection from the front surface of the SLM display. Diffraction caused by the grating-like structure of the pixels in the SLM display itself may also account for some of the low efficiency into the desired mode. The amplitude-contouring also clearly has a strongly negative impact on the diffraction efficiency. This may again be a result of the limited phase modulation depth. The benefits of amplitude

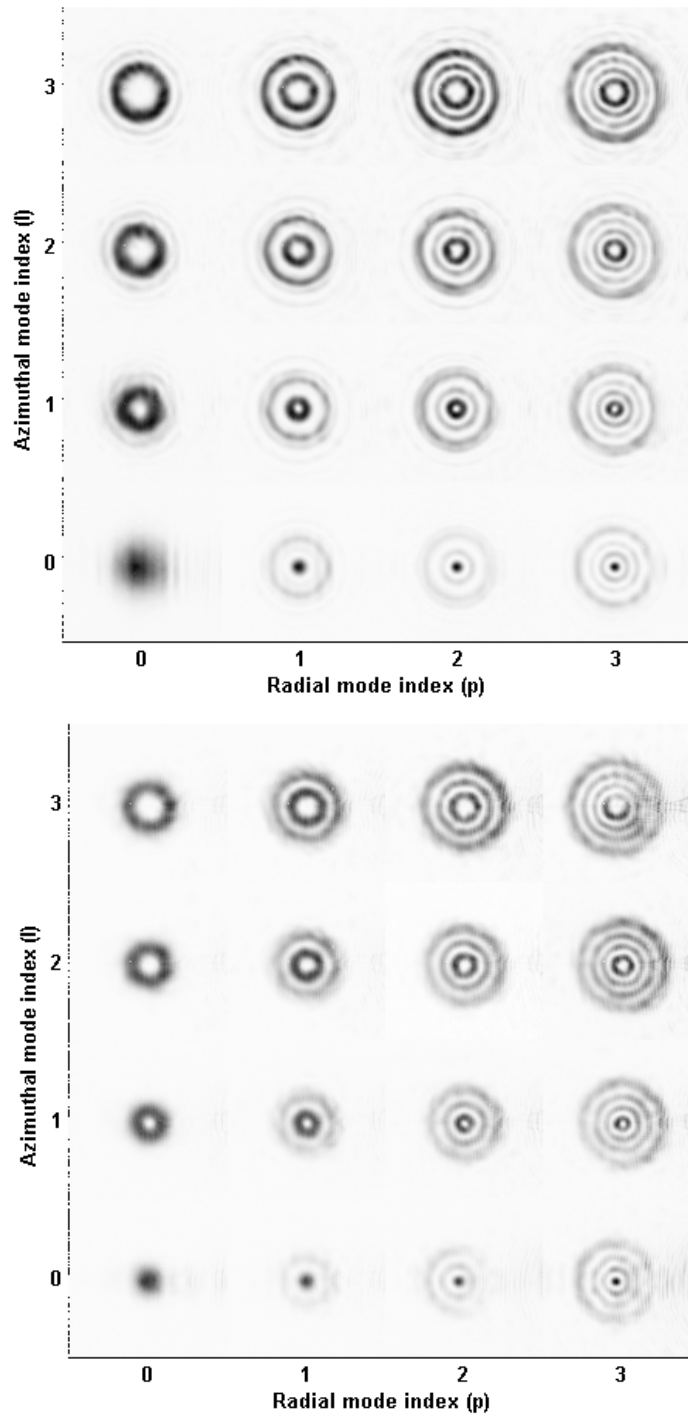


Figure 4.7.: Helical LG modes up to  $LG_{33}$ , as generated using the LCR-2500 SLM without (top) and with (bottom) amplitude contouring.

contouring in terms of generated mode purity and the drawbacks in terms of diffraction efficiency are shown in table 4.3 and discussed later in section 4.3.3 of this chapter.

It is difficult to determine the purity of the modes just from the intensity profile. In order to accurately measure the mode purity, it is necessary to have access to the field amplitude profile, as in the simulation investigation in section 3.2.3. In practice, the field amplitude is very difficult to measure accurately, as it requires an interferometric measurement against a reference plane wave.

For this reason our best estimates of the mode purities achieved with our SLM generation method were obtained using a different method involving a comparison with a numerical model. This analysis is described in section 4.3.3. We did however find it informative to observe the phase profiles of the generated LG modes with an interferometric measurement, in order to get a qualitative picture of the quality of LG modes that we could produce with the SLM.

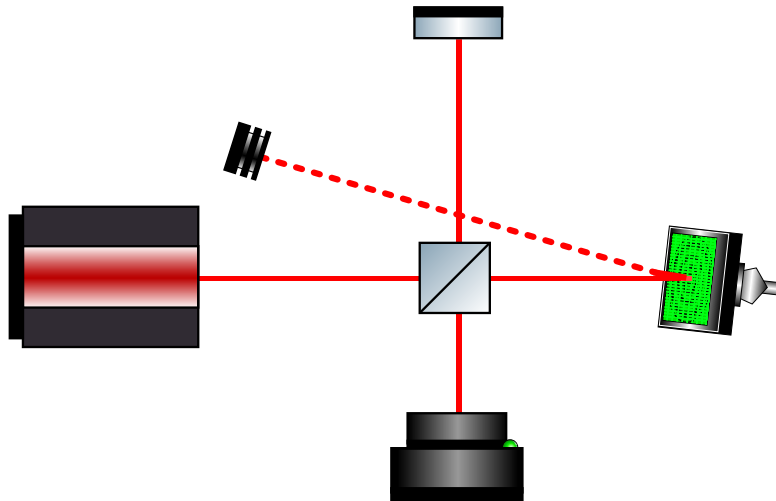


Figure 4.8.: The setup for measuring the interference between SLM generated LG modes and the  $LG_{00}$  mode. The end mirror of one arm of a Michelson interferometer is formed by the SLM, which displays the phase profile for converting to a given  $LG_{pl}$  mode. The beam reflected directly from the SLM is dumped, and the 1st diffraction order, which contains the generated  $LG_{pl}$  beam, is aligned to interfere with the beam from the other Michelson arm. The resulting interference pattern is recorded with the CCD camera.

Figure 4.8 shows the experimental setup for measuring the interference between the SLM

generated LG modes and a  $LG_{00}$  beam. In a similar way to the setup shown in figure 4.2, the SLM is used as one end mirror in a Michelson interferometer. In this experiment however, the SLM displays the LG mode conversion phase profile. The Michelson is aligned such that beam from the arm with a normal end mirror overlaps with the first diffraction order from the SLM, into which the desired LG beam is diffracted by the overlaid blazed grating. The resulting interference pattern is recorded with a CCD camera at the anti-symmetric port of the Michelson.

The lower-left panel of figure 3.11 shows the phase front of an ideal  $LG_{33}$  mode with some residual curvature. In this case, contours of constant phase follow a spiral pattern. We therefore expect the interference pattern between such a mode and a plane wave to have a similar spiral pattern. The exact pattern will depend on the relative path length difference between the arms, or ‘Michelson tuning’, but the main features of the pattern should remain visible at any tuning.

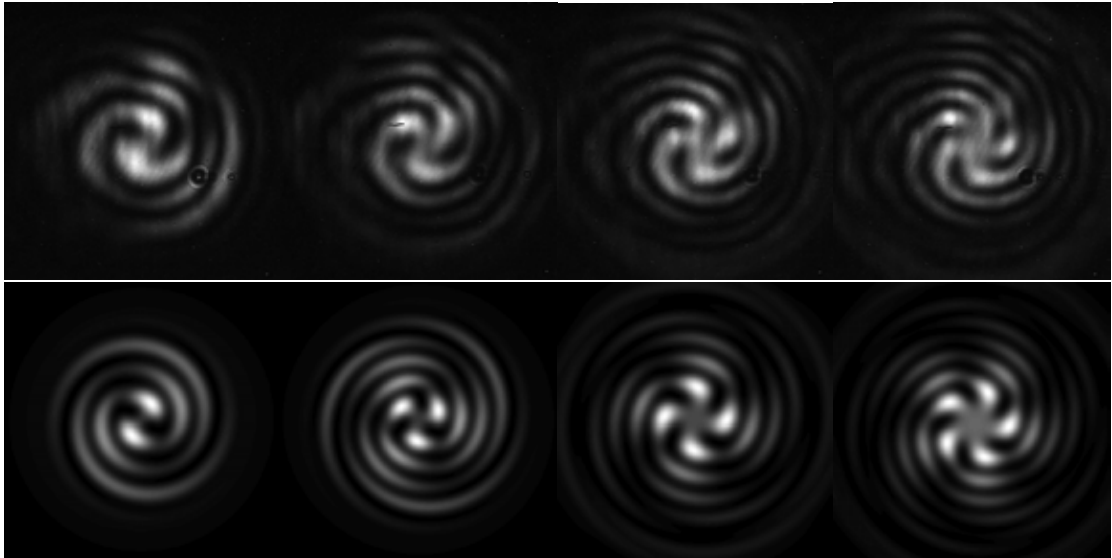


Figure 4.9.: The upper row shows measured interferograms of the SLM generated higher order LG modes with a  $LG_{00}$  mode. From left to right;  $LG_{22}$ ,  $LG_{33}$ ,  $LG_{44}$  and  $LG_{55}$ . The spiral structure in the interferogram indicates the presence of a spiral phase profile in the LG beam. The lower row shows the results of simulations in which an ideal  $LG_{pl}$  mode is interfered with the  $LG_{00}$ , with manually tuned beam parameters.

The top row of images in figure 4.9 shows the measured intensity patterns at the anti-

symmetric Michelson port when the SLM was displaying the phase profile for converting to helical  $LG_{22}$ ,  $LG_{33}$ ,  $LG_{44}$ , and  $LG_{55}$  modes. The striking feature of each of these images is the spiral pattern, each with a number of spiral arms equal to the azimuthal  $l$  index of the LG mode being observed. This spiral pattern is an expected consequence of the interference between the helical LG mode, with its spiral phase front, and the  $LG_{00}$  mode with its spherical phase front, provided that there is some residual curvature difference between the two phase fronts. The lower row of images in figure 4.9 show the results of simulations in which ideal  $LG_{pl}$  modes were interfered with a  $LG_{00}$  mode, with some residual curvature present between the two modes in each case. The main features of the intensity patterns are common between the measured and simulated interferograms, indicating that to some extent at least the SLM generated LG modes have the correct phase profiles.

#### 4.2.2. Blazing angle tests

Figure 4.10 shows the results of an investigation into the effects of using different blazing angles on the SLM phase image. The left column shows the five different phase profiles used in the investigation. Each phase profile was an amplitude contoured profile for converting to a helical  $LG_{33}$  beam. However, each phase profile had a different blazing period overlaid. The right column shows the measured diffraction pattern intensity corresponding to the phase profile, inverted to show detail more clearly. The images shown were obtained using a commercial digital camera focused on a white surface, on which the diffraction pattern from the SLM was incident. This measurement technique was necessary in order to observe the light intensity over a large horizontal range.

The darkest region of each measured diffraction pattern corresponds to the zeroth diffraction order, containing the light which is unmodulated by the SLM. The  $LG_{33}$  mode shape is diffracted into the first diffraction order. Comparing the five different diffraction patterns, we can see that as expected the diffraction angle, and hence separation of the diffraction orders at the measurement point, increases as the blazing period is reduced.

The multiplicative effect on the effective modulation depth with higher diffraction orders described in for example [MDP<sup>+</sup>09] can also be seen in figure 4.10. The faint second diffraction order appears as a single annular intensity pattern. This would be expected if the modulation depth was  $4\pi$  in this order, since the radial phase jumps which correspond to  $\pi$  in the first diffraction order would appear as  $2\pi$  jumps in the second order,

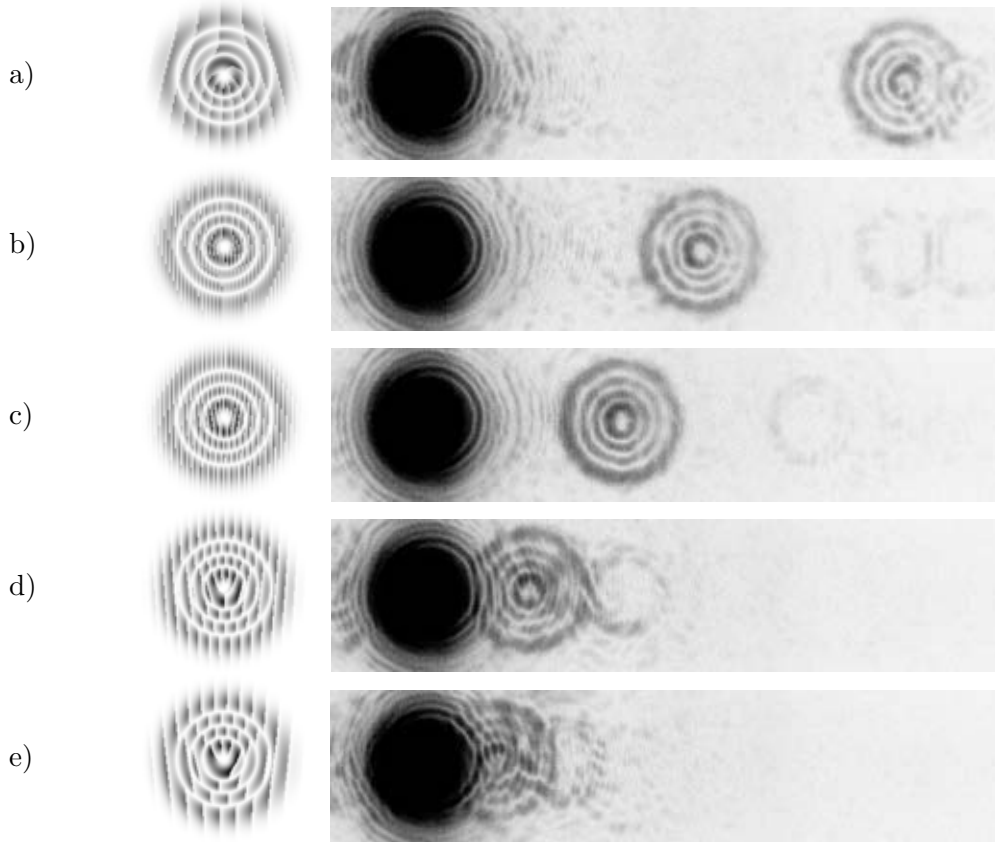


Figure 4.10.: Phase modulation profiles and the corresponding diffraction patterns. The plots a) to e) use the same phase plate to create a helical  $LG_{33}$  mode but are created with different groove width for the blazing: a) 2.123 px, b) 3.7302 px, c) 5.302 px, d) 10.302 px and e) 15.302 px. The images are inverted to show the detail more clearly.

which is equivalent to no jump at all. The 3 helical phase vortices in the first order should appear as 6 vortices in the second order, hence the dominant mode in the second diffraction order should be the  $LG_{06}$  if the target beam in the first order is  $LG_{33}$ .

### 4.3. Mode cleaning higher-order LG modes

One of the main goals of the table-top experiments with higher-order LG modes was to verify the compatibility of the  $LG_{33}$  mode with the PDH longitudinal cavity control scheme. The simulation study described in section 3.1 had shown that the PDH scheme

should work in exactly the same way for the LG<sub>33</sub> mode as for the LG<sub>00</sub> mode, but it was still a crucial step to verify this experimentally. The task at hand was therefore to demonstrate the feedback control of an optical cavity pumped with the LG<sub>33</sub> mode using the PDH method. At this point we recognised the opportunity to achieve two objectives with one experiment, by simultaneously investigating the *mode cleaning* effect of an optical cavity on the SLM generated LG<sub>33</sub> beams. As well as demonstrating the compatibility of the LG<sub>33</sub> mode with a crucial interferometric technique, we could also show that the mode cleaner effect can be used to create extremely pure LG<sub>33</sub> modes, even from relatively low purity SLM generated LG<sub>33</sub> beams.

In this section I first give an introduction to the mode cleaner effect and its use in current gravitational wave interferometers. I will then describe the design and characterisation of two different mode cleaner cavities that were used in our investigation. Finally I will describe the experiment performed with the LG<sub>33</sub> mode in a linear mode cleaner cavity, demonstrating the feedback control of the cavity and the increase in purity of the LG<sub>33</sub> beam upon transmission through the cavity.

### 4.3.1. The mode cleaner effect

The mode cleaner effect arises from the different round trip Gouy phase accrued by different mode orders [Boy80] in an optical cavity. The different amounts of Gouy phase accrued by different mode orders can be seen in the phase factor  $\exp(i\Psi(n + m + 1))$  in equation 2.13, and  $\exp(i\Psi(2p + l + 1))$  in equations 2.15 and 2.14. Any given eigenmode of a cavity experiences the mode order<sup>1</sup> plus one times the fundamental mode round trip Gouy phase,  $\Psi_{\text{RT}}$ . This round trip phase difference between different mode orders can be taken advantage of in order to separate unwanted ‘parasitic’ modes from the desired mode; an optical cavity can be designed such that when resonant for the desired mode, is it non-resonant for the unwanted modes. In this way, a cavity can ‘clean’ out unwanted modes from the beam it is pumped with [RSS<sup>+</sup>81], hence the name mode cleaner.

The round trip Gouy phase  $\Psi_{\text{RT}}$  is a function of the cavity length and the eigenmode Rayleigh range given by

$$\Psi_{\text{RT}} = 2 \arctan \left( \frac{L}{z_{\text{R}}} \right). \quad (4.2)$$

---

<sup>1</sup> $n + m$  for HG modes or  $2p + l$  for LG modes

For the simple case of a plane-concave cavity, the cavity Rayleigh range  $z_R$  is given by

$$z_R = \sqrt{L(R_c - L)}, \quad (4.3)$$

where  $L$  is the cavity length and  $R_c$  is the radius of curvature of the concave mirror. This leads to the simple expression for the round trip Gouy phase for a plane-concave cavity:

$$\Psi_{RT} = 2 \arctan \left( \frac{1}{\sqrt{\frac{R_c}{L} - 1}} \right). \quad (4.4)$$

A well designed mode cleaner should be designed such that the length and mirror curvatures give a large round trip Gouy phase difference between adjacent mode orders. This ensures that while the desired mode is resonant, parasitic modes which are close by in terms of mode order will be strongly suppressed in the cavity. Care should also be taken to ensure that the round trip Gouy phase is not close to being a low integer fraction of  $2\pi$ , i.e. that

$$\Psi_{RT} \neq \frac{2\pi}{n}, \quad (n = 1, 2, 3\dots) \quad (4.5)$$

to avoid degeneracy with higher FSR resonances of modes different in order by  $n$  from the desired mode.

Figure 4.11 shows the results of a numerical simulation performed using FINESSE [FHL<sup>+</sup>04], of a plane-concave linear mode cleaner cavity of length 21 cm, and with the concave end mirror with radius of curvature 1 m. Putting these values for cavity length and end mirror curvature into equation 4.4 gives a result for the round trip Gouy phase of  $\Psi_{RT} = 54.55^\circ$ . Comparing with figure 4.11, we can see that the resonances of successive mode orders are separated in cavity length by half of the round trip Gouy phase difference;  $27.27^\circ$ , as expected. The factor of two discrepancy arises from the fact that the extra optical path length associated with a cavity detuning is experienced twice during one round trip.

Mode cleaners are used in several locations in gravitational wave interferometers [AAA<sup>+</sup>04]. So-called *pre-mode cleaners* are used as stable references in the initial frequency stabilisation chain of the laser. These typically employ small, monolithic spacers in air. The beam then passes through the *input mode cleaner*<sup>2</sup>; a suspended optical cavity in vacuum. The main function of the input mode cleaner is to filter out beam geometry

<sup>2</sup>Or in the case of the GEO600 detector, two input mode cleaners.

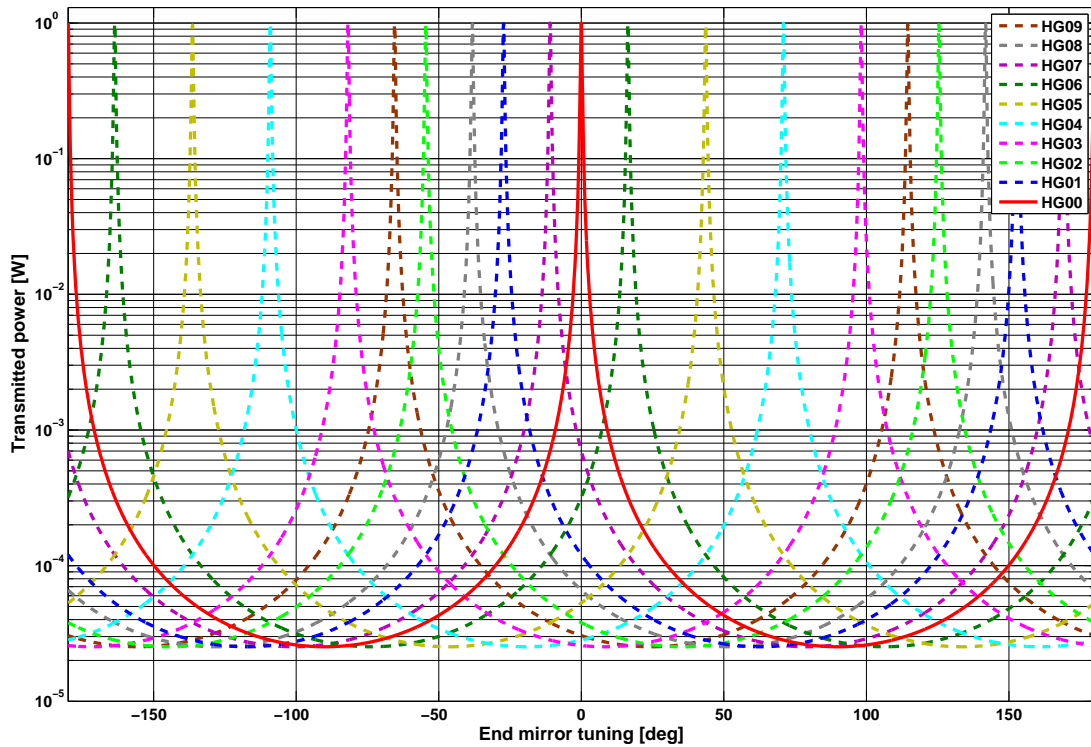


Figure 4.11.: Results of a FINESSE simulation for a mode cleaner cavity, showing transmitted power as a function of cavity length tuning for an input beam of 10 W, distributed evenly between 10 HG modes of different orders. The round-trip Gouy phase difference between the different mode orders separates their resonant peaks.

fluctuations (also called beam-jitter noise). If we recall that alignment fluctuations can be described by the addition of higher-order HG modes (see section 2.4), it is clear that by suppressing the amplitude of higher-order HG modes the alignment fluctuations in the beam transmitted through the input mode cleaner can be suppressed.

Most gravitational wave interferometers also include optical cavities in the main interferometer, which act as additional mode cleaning cavities. Often a small in-vacuum output mode cleaner is also used to filter the spatial properties of the light leaving the interferometer before it reaches the photodetectors. Since mode cleaner cavities are so prevalent in gravitational interferometers, it is important to investigate their compatibility with the  $LG_{33}$  mode.

Mode cleaner	Finesse	FSR	TEM <sub>01</sub> suppression	Throughput
GEO MC1 [GCF <sup>+</sup> 03]	2700	37.48 MHz	1325	80 %
GEO MC2 [GCF <sup>+</sup> 03]	1900	37.12 MHz	937	72 %
Virgo IMC [GMSV10]	1181	1.044 MHz	NA	86.6 %
aLIGO IMC [AdL07]	500	17.96 MHz	NA	NA
Linear MC	172	714 MHz	50.1	63 %
Triangular MC	307	714 MHz	87.6	99 %

Table 4.1.: Cavity parameters for some gravitational wave detector input mode cleaners, as well as for cavities used in this work. TEM<sub>01</sub> suppression factors and throughput percentages are given in terms of light power. The finesse and TEM<sub>01</sub> suppression factors of the mode cleaners used in this work were chosen to be lower than those of the large-scale mode cleaners.

Currently a triangular arrangement is favoured for the mode cleaners in gravitational wave detectors as it gives a spatial separation between the injected beam from the reflected beam, enabling a length control error signal to be measured in reflection without the need for polarising optics. However, triangular cavities are not ideal for use with higher-order helical LG modes, for reasons demonstrated in section 4.4. As a result of these considerations, the main experimental setup described here makes use of a linear mode cleaner cavity instead of a triangular cavity. The finesse of the linear cavity was chosen to be low in comparison with some gravitational wave detector input mode cleaners, as shown in table 4.1. While higher finesse cavities can give a stronger suppression of misalignment modes, it was interesting for us to see the large improvement that can already be gained through the use of a low-finesse mode cleaner.

### 4.3.2. Design and characterisation of the triangular and linear mode cleaners

For improving the purity of the SLM generated LG modes, we employed a linear mode cleaner cavity (LMC) consisting of two mirrors; one flat and one concave, as shown in figure 4.12. We also used a triangular mode cleaner cavity (TMC) consisting of two flat mirrors and one curved mirror to test the predictions about the interaction of LG modes

with three mirror cavities. The design of the TMC was based on the design described in [Ueh97], and is summarised along with the linear mode cleaner design in table 4.1.

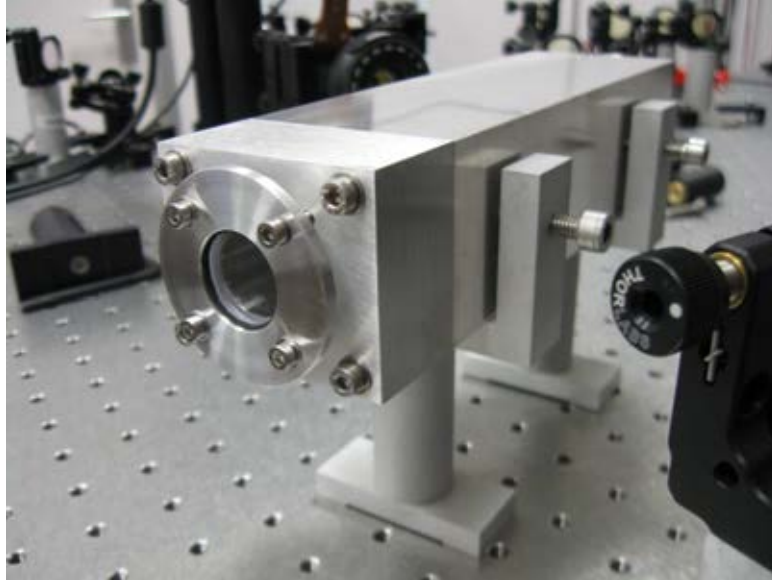


Figure 4.12.: The linear mode cleaner cavity used in the LG mode cleaning experiment. The cavity mirrors are clamped to a rigid aluminium spacer.

It was necessary to measure the finesse of the mode cleaner cavities, in order that their interaction with LG modes could be well understood and compared with simulations. Here I will only describe the process of measuring the finesse of the triangular cavity, since the same method was used to measure the finesse of the linear cavity. Our method for measuring the finesse was to perform scans of the cavity by applying a triangular wave ‘ramp’ signal to the PZT attached to one of the cavity mirrors, and recording the transmitted light power through the cavity with a photodiode. With the recorded cavity response, we could then fit a theoretical model to the data and thus estimate the finesse. We found, however, that the PZT response was not sufficiently linear over the range of a full cavity FSR to provide a reliably linear x-axis for the scan. Some extra steps were therefore required in order to make an accurate estimate of the finesse.

First of all, the cavity was slightly misaligned, in order to induce the presence of higher-order modes within the cavity. The advantage of this is that the separation between successive mode orders is a constant, and so the location of each higher-order mode peak gives an indication of the true x-axis position at that point, unaffected by the PZT

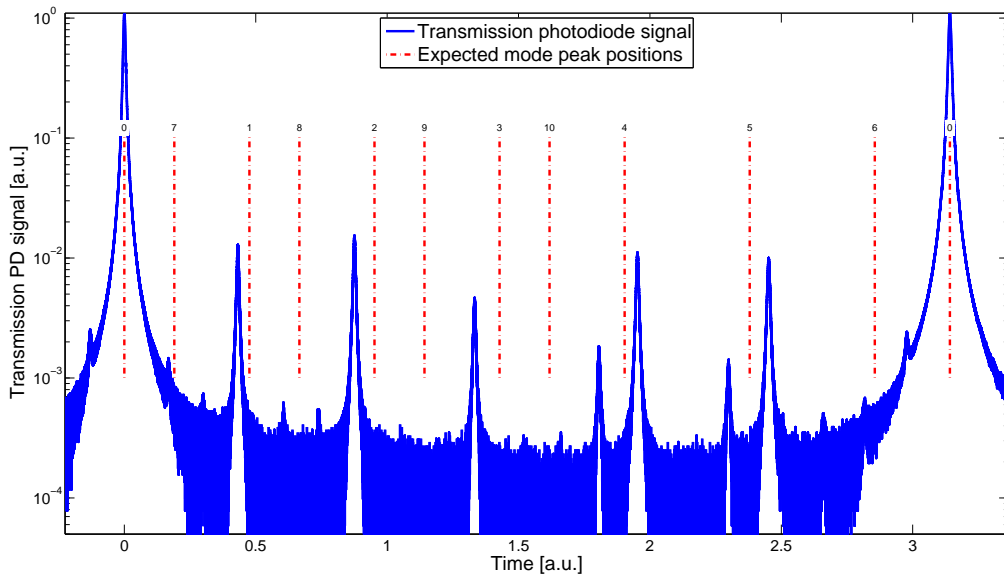


Figure 4.13.: Measured transmitted light power through the TMC as the cavity length was scanned with the PZT. The theoretically expected higher-order mode positions are labelled with the red dashed lines. These positions do not match up with the higher-order mode resonances in the measured data, which were induced by misaligning the cavity input beam.

non-linearity. Figure 4.13 shows the data from a scan of the TMC, compared with the theoretical predictions for the higher-order mode peak locations. It can be seen that the peak locations do not agree, as a result of the non-linearity of the PZT response over the scanned range.

The difference in the expected and apparent positions of the higher-order mode peaks was used to fit a parabolic function for the deviation of the PZT response from linear across the scanning range. The results of this fit are shown in figure 4.14. With the non-linearity of the PZT accounted for and the x-axis thereby calibrated, the scan data and the theoretical peak positions agree much more closely, as shown in figure 4.15. The calibrated data was then compared with a theoretical cavity response function, and a non-linear fit was made for cavity finesse. Figure 4.16 shows the results of the fit, over the whole scanning range (top) and in proximity of the two fundamental mode peaks (bottom). The result of the fit for the whole data series was 308. The results of the fits to each individual peak were 305 and 309, each exhibiting less than 1% deviation from

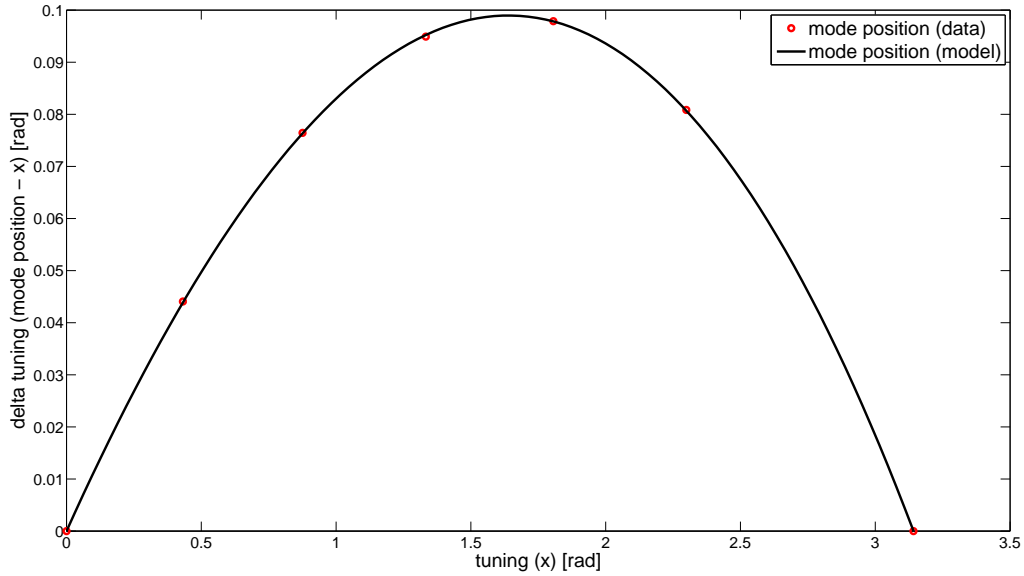


Figure 4.14.: Calibration curve for the TMC PZT. The red data points show the residuals between the expected and apparent higher-order mode resonance positions in the plot shown in figure 4.13, and the black curve shows the result of fitting a parabolic function to the data. The parabolic function was subsequently subtracted from the PZT ramp data in order to linearise the x-axis of the scan.

the overall fit. The same process was used to estimate the finesse of the LMC, and gave a result of 172.

### 4.3.3. Operation of the linear mode cleaner with higher-order LG modes

Figure 4.17 shows the experimental setup for the investigation into the performance of the LG<sub>33</sub> mode in a linear mode cleaner. The 1064 nm laser light is passed through an electro-optic modulator (EOM) for the purpose of imprinting 15 MHz phase modulation sidebands on the light to enable length control of the mode cleaner. The beam is then passed onto the modulating surface of the SLM, where the phase characteristics of the desired LG mode are imprinted on the beam. The converted LG beam is then passed through a telescope to match the beam parameters to the mode cleaner eigenmode. Figure 4.18 shows a photograph of this experimental setup on the bench in the laboratory.

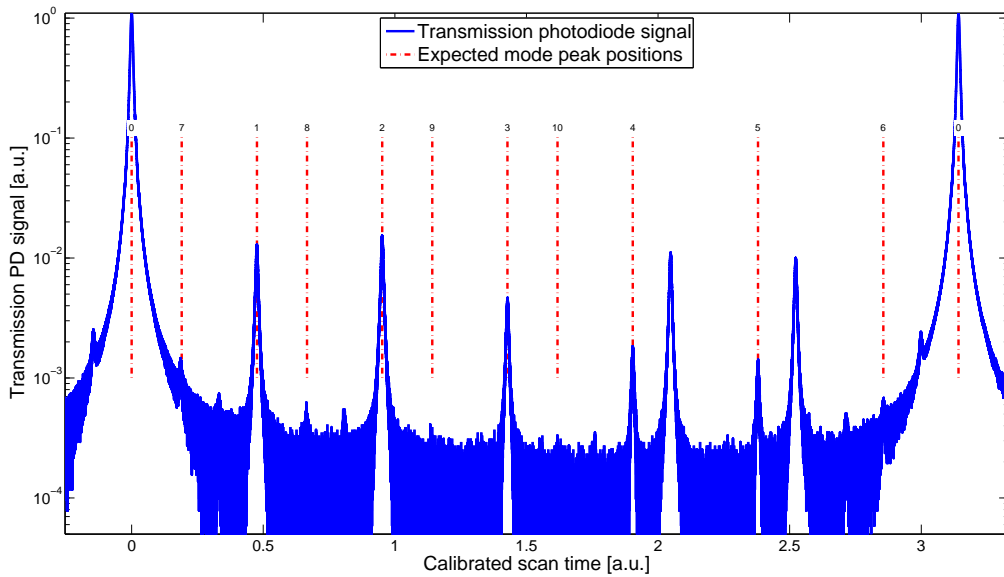


Figure 4.15.: The TMC scan after compensation for the non-linearity of the PZT. The expected higher-order mode positions now match the apparent mode positions much more closely.

The light transmitted through the mode cleaner passes through a beam splitter, and is analysed at the two ports with a photodiode and CCD camera simultaneously. The signal from the photodiode is mixed down with the original 15 MHz local oscillator signal to generate the length error signal. The error signal across the resonance of the  $LG_{33}$  mode was observed by injecting a ramp signal onto the Piezo-electric transducer (PZT) attached to the mode cleaner end mirror in order to scan the length of the cavity, and then recording the mixer output.

The blue solid line in figure 4.19 shows the length error signal recorded for a sinusoidal  $LG_{33}$  input beam, recorded from the output of the mixer while scanning over the  $LG_{33}$  resonance of the linear mode cleaner. The results of a numerical simulation of the setup are also shown in figure 4.19 as the red dotted line. It can be seen that the measured error signal is effectively equivalent to the simulated error signal, which itself was equivalent to the simulated error signal for a  $LG_{00}$  input beam, as was previously shown for a similar setup in simulations described in section 3.1.

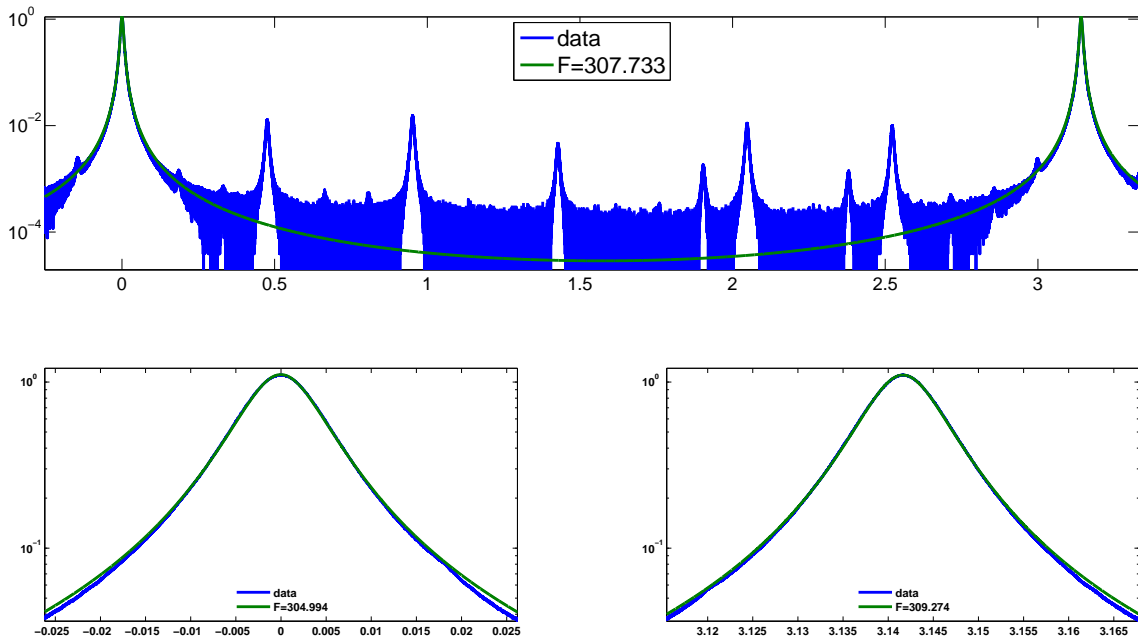


Figure 4.16.: The results of a non-linear fit of a model cavity response to the calibrated scan data. The finesse of the model was adjusted for an optimal match to the data, giving a best-fit finesse of 308. Separate fits to the two individual  $LG_{00}$  peaks gave results for the finesse that were within 1% of the value for the fit of the whole data series.

In typical gravitational wave interferometer implementations of mode cleaners the error signal is taken in reflection, following the Pound-Drever-Hall (PDH) method [DHK<sup>+</sup>83]. For this work, however, the mode cleaner cavity was of a low enough finesse that the modulation sidebands were partially transmitted through the cavity. This allowed us to measure the length error signal in transmission. It also allowed us to measure a length error signal in reflection from a triangular cavity placed after the LMC in the PDH method, as described in section 4.4, without the need for another phase modulator placed after the LMC. We have subsequently demonstrated the equivalent operation of the LMC with the  $LG_{33}$  mode with a length error signal taken in reflection using the PDH method, for example in the work described in section 5.3. The  $LG_{33}$  error signal in both of these cases also showed no difference to the  $LG_{00}$  error signal, confirming that the PDH longitudinal sensing scheme is equivalent for the  $LG_{33}$  mode and the  $LG_{00}$

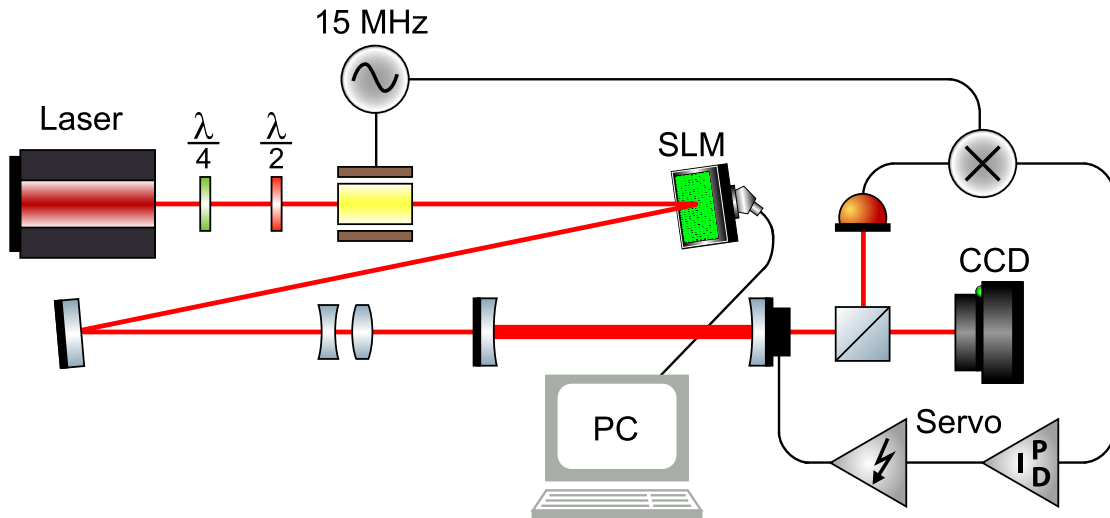


Figure 4.17.: The experimental setup for mode cleaning a SLM generated higher-order LG beam. The  $LG_{00}$  input beam is converted to a higher-order LG beam by the SLM. The resulting beam is passed through a mode-matching telescope into the linear cavity. The transmitted light is used to generate an error signal which is fed back to the PZT attached to the curved end mirror to control the length of the cavity. The transmitted beam is simultaneously imaged on the CCD camera.

mode.

The DC transmitted light level measured by the photodetector was used to aid in aligning and mode matching the beam to the cavity. Misalignments and mode mismatches cause coupling to modes of other orders than the injected mode, which appear in the scan as additional peaks alongside the desired mode order peak, as shown in figure 4.25. The alignment and mode matching lens positions were adjusted to minimise the amplitude of these other mode order peaks. The alignment and mode matching of the cavity was more sensitive in the case of the  $LG_{33}$  mode than the  $LG_{00}$  mode, in that a given misalignment or mode mismatch caused a greater amount of power to be coupled into adjacent mode orders for the  $LG_{33}$  input. While this effect is partly due to the  $LG_{33}$  beam shape itself, in this case it may also be partly due to the relatively low purity of the input beam. The power present in other modes in the input beam due to the imperfect nature of the conversion procedure will show up in the cavity scan even when the alignment and mode matching are optimal.

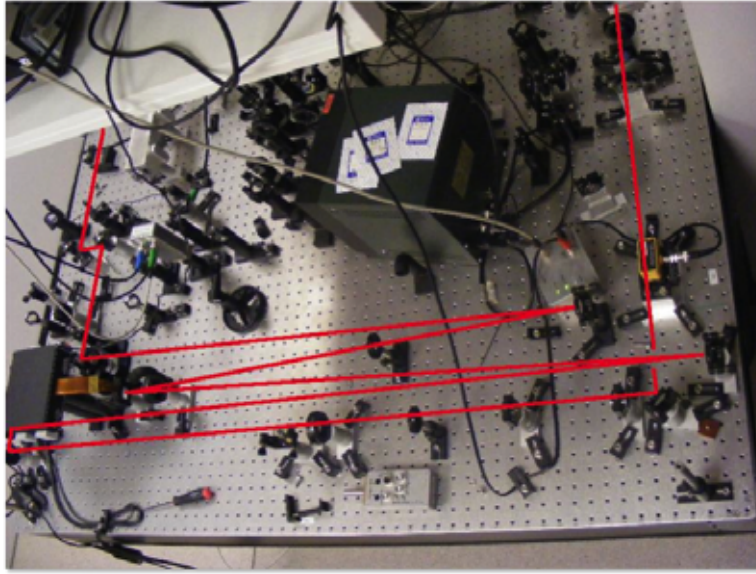


Figure 4.18.: The table-top LG mode conversion and cleaning setup. The laser source is in the upper right hand corner, the SLM is in the lower left hand corner and the linear mode cleaner is in the top left hand corner.

We subsequently closed the feedback control loop by connecting the error signal channel to the PZT via a servo and high-voltage amplifier. The length of the mode cleaner cavity was thereby controlled or ‘locked’ to maintain the resonance condition for the desired mode order. When controlled for the resonance of the  $LG_{33}$  mode, the cavity remained stable for many hours. Lock acquisition was easy and repeatable with the setup, and the lock could even be maintained during a change of input beam from helical to sinusoidal, and vice versa. The stable locking of a cavity to a higher-order LG mode was a very significant result, since the use of RF modulation/demodulation control loops are such a fundamental technique in the operation of gravitational wave interferometers. To our knowledge this was the first time an optical cavity had been operated with a higher-order LG mode, and we reported this result in [FKCF10].

The CCD camera was used to record intensity images of the transmitted beams while the mode cleaner was controlled to be resonant for the  $LG_{33}$  mode. The input and output beam intensity distributions for both helical and sinusoidal  $LG_{33}$  beams are shown in figure 4.20. It is clear by inspection that the output modes are more symmetrical, and have a higher intensity in the innermost bright radial fringe relative to the others; both features characteristic of  $LG_{33}$  modes. The typical method of analysing the output

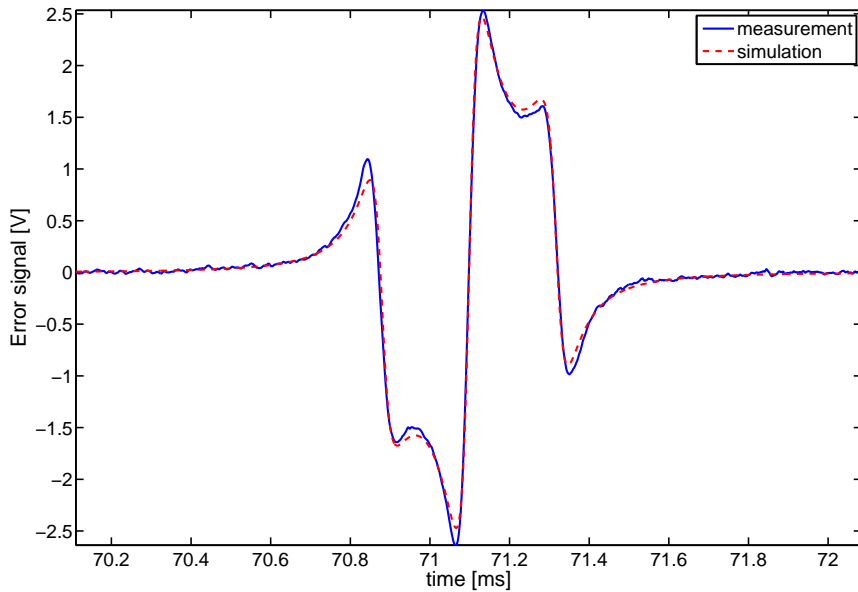


Figure 4.19.: The blue trace shows the length error signal from the linear cavity, set up as shown in figure 4.17, with a sinusoidal  $LG_{33}$  input beam. The red dashed trace shows the length error signal for the same optical setup as simulated in the frequency domain simulation software FINESSE. While there are small discrepancies between the two traces, the primary features are identical, as predicted for a similar setup in [CHF09].

mode purity would be to pass the output beam through another cavity and observe the magnitudes of different mode order resonances [KSWD07]. However, since in this case the performance of the mode in a cavity is itself being investigated, this method in its original form is not useful for our purposes. In addition, though this method is suitable for finding the proportion of the light in different mode orders, it cannot differentiate between different modes of the same order, and therefore cannot give an estimate for the actual  $LG_{33}$  mode content of the beam.

Instead, we estimated the mode content based on the intensity pattern alone, with the aid of numerical simulations. The method we used to estimate the mode content of the transmitted light relies on the fact that the light transmitted through the cavity can be described as a sum of the eigenmodes of the cavity <sup>3</sup>.

<sup>3</sup>While in fact any beam can be described by a sum of such eigenmodes, this would not be such an effective way of analysing less pure beams, such as for example the input  $LG_{33}$  beams, since a very

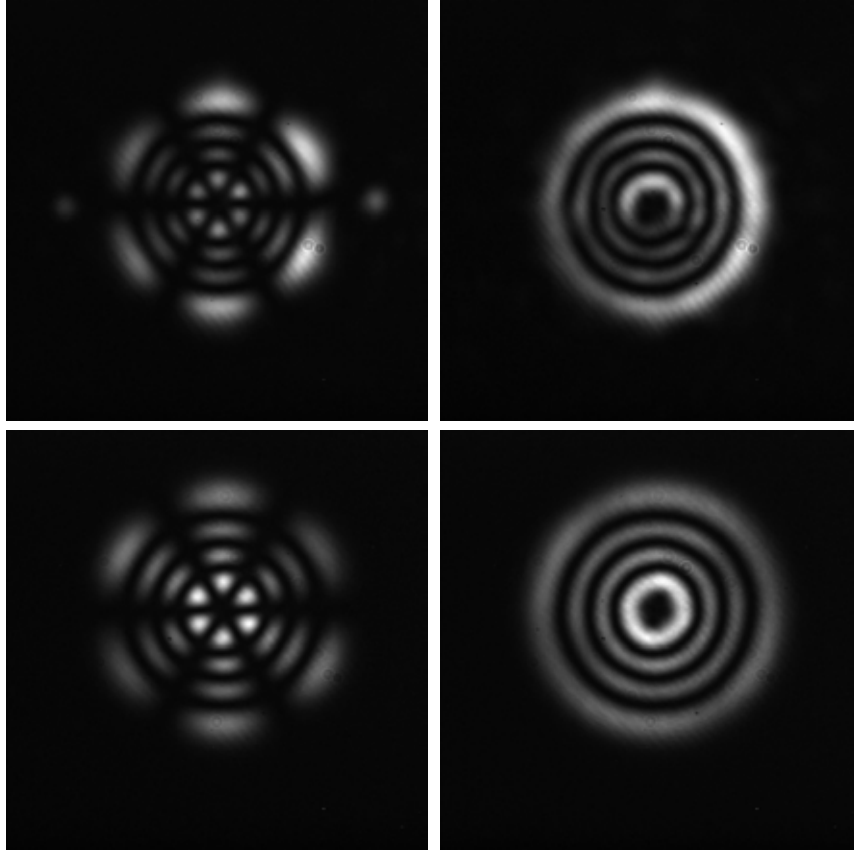


Figure 4.20.: The measured intensity patterns of the sinusoidal (left column) and helical (right column)  $LG_{33}$  beams before (upper row) and after (lower row) transmission through the linear mode cleaner. The increase in mode purity upon transmission is already evident in the increased symmetry. The remaining asymmetry apparently is a result of the inaccuracy in the manual alignment of the input beam to the mode cleaner. This effect is the same for both images but more visually apparent in the case of the helical mode.

The first step was to select the optimal basis system for the modal description of the measured light. A modal decomposition of a light field depends on the coordinate system used, as demonstrated for the optic axis definition in relation to the HG modes in section 2.4, and for the beam spot size parameter definition in relation to LG modes in section 2.5. In order not to underestimate the mode content in the  $LG_{33}$  mode, it was therefore necessary to choose a coordinate system in which the  $LG_{33}$  mode content

---

large number of eigenmodes may be required to describe the higher spatial frequency components.

would be maximal. In practice this process took the form of a non-linear fit of an ideal  $\text{LG}_{33}$  mode intensity distribution to the measured intensity data. The fitted parameters were the coordinates of the optic axis, and the beam spot size. One can also understand this step as simply a calibration of the CCD.

The next step was to analyse the residuals after subtracting the ideal  $\text{LG}_{33}$  intensity from the measured intensity. These residuals are shown for the sinusoidal  $\text{LG}_{33}$  beam in the left two panels of figure 4.21. The leftmost panel shows the residual for the input beam, and the middle panel shows the residual for the transmitted beam. The scale of the residuals is less for the output  $\text{LG}_{33}$  beam than for the input beam, thus already demonstrating an increase in mode purity upon transmission through the mode cleaner.

For the sinusoidal case, the spatial distribution of the transmitted beam residuals indicates that the remaining mode impurities may be dominated by the effects of a misalignment of the injected beam into the mode cleaner. This indication comes from the fact that intensity residual closely resembles that of a superposition of the two modes  $\text{HG}_{09}$  and  $\text{HG}_{18}$ , and the fact that misalignments can be described by the addition of HG modes (see section 2.4).

Using this information, a model of the mode cleaner setup was developed using FINESSE. In this model, the input beam could be misaligned by varying amounts, and the transmitted field analysed. We found that it was possible to create a beam residual intensity which was very similar to the measured pattern when the model included a misalignment of the input beam of  $\alpha_x = -100 \mu\text{rad}$  in the horizontal plane, and  $\alpha_y = 60 \mu\text{rad}$  in the vertical plane. The residual pattern between the intensity pattern calculated with the FINESSE simulation, and the ideal  $\text{LG}_{33}$  mode is shown in the right hand panel of figure 4.21. The result of the simulation shows a very strong agreement with the experimentally measured data.

With a model that reproduced the measured data so well, we could make some estimates of the mode content of the measured beam by analysing the mode content of the model. This was done by separately evaluating the overlap integrals between the complex field amplitude of the model and the field amplitudes of all LG eigenmodes, up to the maximum mode order of 12. The reason this could not be done directly with the measured data is because we do not have access to the field amplitude in that case; just the intensity.

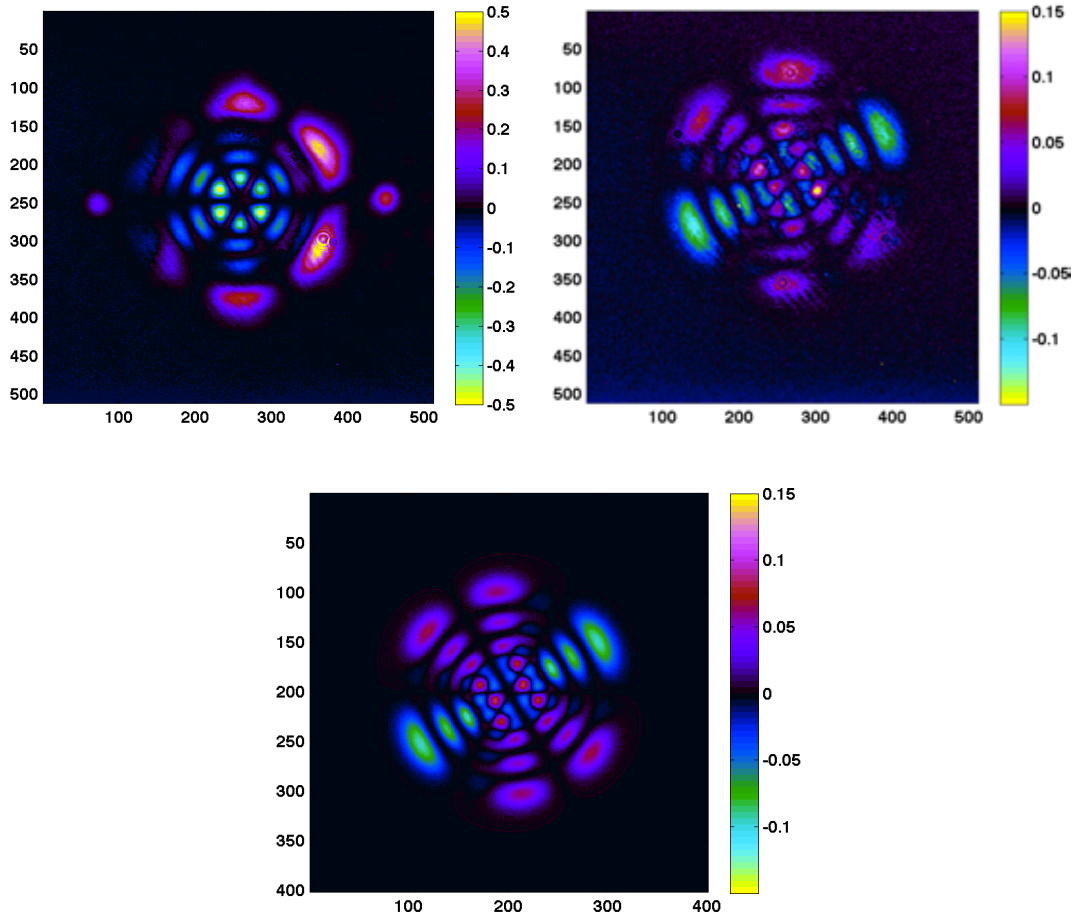


Figure 4.21.: Residuals from best fits between three intensity patterns and a theoretically ideal sinusoidal  $LG_{33}$  intensity profile. From left to right: the residual for the measured input  $LG_{33}$  beam, the residual for the measured output  $LG_{33}$  beam, the residual for an output  $LG_{33}$  intensity profile generated with a numerical model including a misalignment of the input beam to the cavity.

The results of this eigenmode decomposition for the sinusoidal beam are shown in table 4.2. This table shows that we estimate 99% of the light power to be in  $LG_{33}$  mode, and most of the remaining light power to be distributed in other modes of order 9. That most of the light power not in the  $LG_{33}$  mode is in other modes of order 9 is to be expected, since the mode cleaner is not expected to differentiate between different modes of the same order. A similar analysis for the helical mode gave effectively the same results for the mode purity.

$u_{lp}^{\text{sin}}$ mode	3, 3	4, -1	2, -5	4, 1	2, 5	other
power	99%	0.4%	0.3%	0.1%	0.1%	< 10 ppm

Table 4.2.: Mode decomposition of the numerical model of the sinusoidal LG<sub>33</sub> beam transmitted through the linear mode cleaner, under an input beam misalignment of -100  $\mu\text{rad}$  in the horizontal axis, and 60  $\mu\text{rad}$  in the vertical axis. The majority of the beam power is in the desired sinusoidal LG<sub>33</sub> mode, with the rest almost entirely concentrated in other modes of order 9.

Since 99% of the transmitted beam was in a single mode, we could make an accurate estimate of the input mode purity by simply comparing the amount of power transmitted through the mode cleaner to the amount of power injected into it. Once the intrinsic losses of the mode cleaner are taken into account, all of the light which was not transmitted through the mode cleaner may be assumed to be in unwanted modes other than the LG<sub>33</sub> mode. We estimated the intrinsic losses of the mode cleaner by injecting a pure LG<sub>00</sub> beam into the mode cleaner and measuring the transmitted power as a fraction of the input power, while the mode cleaner was controlled on the LG<sub>00</sub> resonance. This measurement gave a throughput power efficiency for the mode cleaner of 63%. This relatively low efficiency is likely due to the use of potentially lossy ‘off the shelf’ mirrors, and the slightly overcoupled cavity design, which reduces the maximum transmitted intensity.

After taking the intrinsic optical losses of the mode cleaner cavity into account, we estimated the input mode purity of the sinusoidal LG<sub>33</sub> beam to be 51%, and 66% for the helical LG<sub>33</sub> beam. Examples of higher-order LG modes with mode purities likely to be well above 70% have been created previously directly with SLMs using a more thoroughly optimized conversion procedure, for example in [MAI<sup>+</sup>08], although in this case the authors refrain from quoting an experimentally measured purity. However, our work was the first time a purity improvement of a LG mode using an optical resonator to an estimated 99% has been reported in the scientific literature. From the agreement with the model, we believe the demonstrated mode purity to be limited in first order by the manual alignment of the input beam. If this is the case, the mode purity can very likely be improved by using a standard automatic alignment system, such as the Ward technique described in [MRWM94b]. Table 4.3 summarises the results for the generated LG<sub>33</sub> mode purities with the amplitude contoured and non-contoured SLM

LG <sub>33</sub> mode	Amplitude contouring	Mode purity (%)	Conversion efficiency (%)
Helical	No	56	8.7
Sinusoidal	No	40	6.6
Helical	Yes	66	2.5
Sinusoidal	Yes	51	1.0

Table 4.3.: Purities of the generated modes before mode cleaning, and efficiencies of the SLM LG<sub>33</sub> mode conversion process, for the amplitude contoured and non-contoured cases.

profiles, as well as the overall conversion efficiencies. We can see that although the amplitude contouring gives roughly a 20% increase in the purity of the mode generated, it comes at the cost of more than a factor of 6 in efficiency for the sinusoidal case, and a factor of more than 3 for the helical case. It should be noted that these results are likely to be improved for a SLM which is better optimised for the wavelength used.

It was also possible to lock the mode cleaner to even higher-order LG modes of both the helical and sinusoidal variety, as shown in figure 4.22.

We also measured the interference pattern between a LG<sub>33</sub> mode transmitted through the linear mode cleaner cavity and a LG<sub>00</sub> mode, in a similar way to the measurements shown in figure 4.9. The measured interference pattern is shown in figure 4.23. The two superposed beams in the right panel are deliberately misaligned, as this results in a more intuitively understandable image. The forked interference pattern shows some similarity to the phase profile used to generate the LG<sub>33</sub> mode, as shown in figure 3.8. The number of fork teeth in the central region indicates the  $l$  value of the mode being observed [JT08], and the number of dark radial bands as ever indicates the  $p$  value of the mode.

In this section we have demonstrated the feedback control of an optical cavity with the LG<sub>33</sub> mode, as well as even higher-order LG modes, and shown a dramatic increase in the purity of SLM generated LG<sub>33</sub> modes upon transmission through an optical cavity. We have also estimated the efficiency of the mode conversion process. Though this efficiency was very low in our experiment, we expect that using a custom made transmissive diffractive optical element will result in much higher conversion efficiencies.

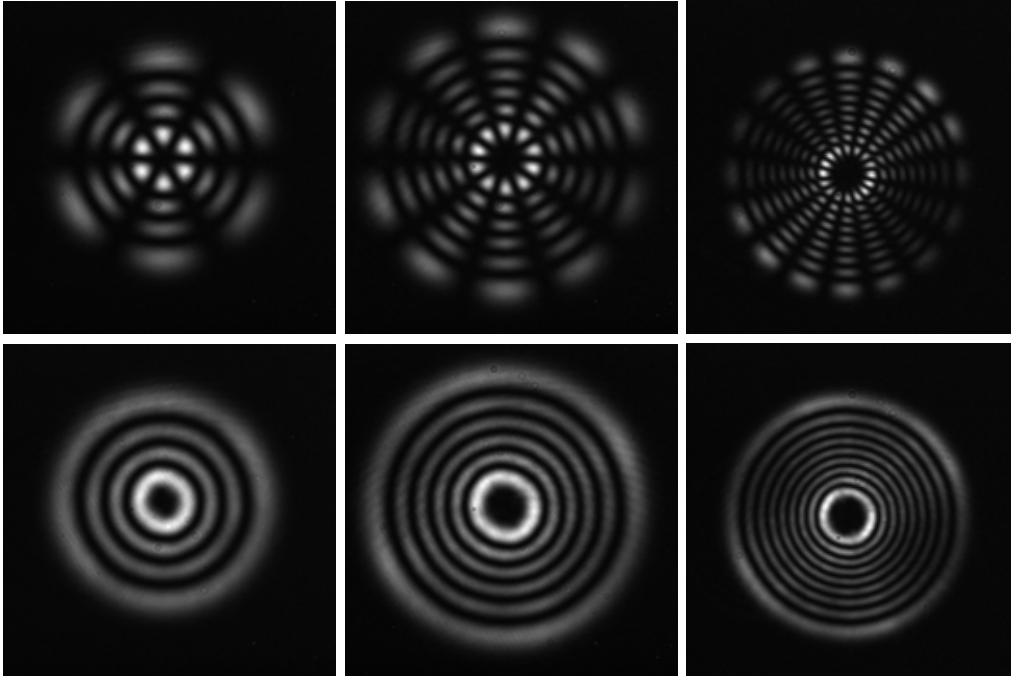


Figure 4.22.: Higher-order sinusoidal (top row) and helical (bottom row) LG modes transmitted through the linear mode cleaner. From left to right: LG<sub>33</sub>, LG<sub>55</sub> and LG<sub>88</sub> modes

#### 4.4. Helical LG mode interaction with a 3-mirror cavity

As intimated in section 4.3, we believed that a triangular mode cleaner would not be compatible with helical LG<sub>33</sub> modes. This is primarily due to the fact that after one full round-trip in a triangular cavity, any beam is reflected 3 times, and is thus mirrored about the vertical axis. This means that only light fields with symmetry about this axis can constructively interfere and be fully resonant. While the *intensity* profiles of helical LG<sub>33</sub> modes display symmetry about the vertical axis, their *phase* profiles do not, as shown in the leftmost panel of figure 4.24. Certain sinusoidal modes, on the other hand, do possess the required symmetry (or anti-symmetry) about the vertical axis, as shown in the middle and right panels of figure 4.24. We also expect that the vertically symmetric mode and the vertically anti-symmetric modes should have different resonance conditions. This is because the anti-symmetric mode will require an additional  $\lambda/2$  of round trip path length compared to the vertically symmetric mode (equivalent to an additional  $\pi$  phase shift), in order to interfere constructively. The

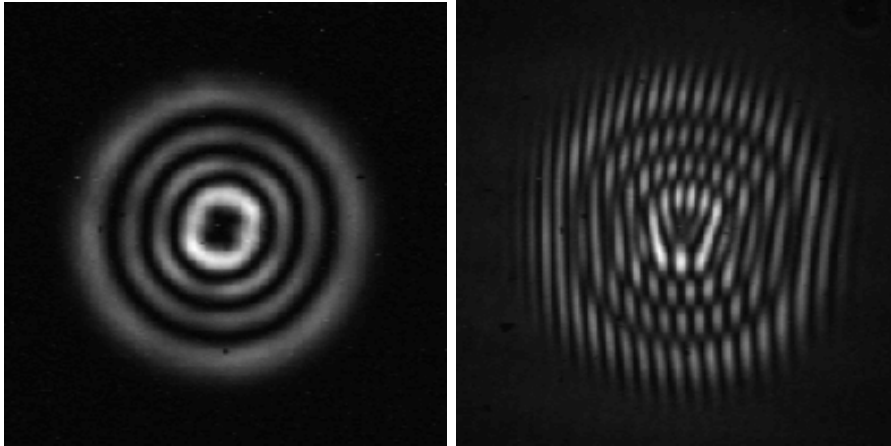


Figure 4.23.: The  $LG_{33}$  mode transmitted through a linear mode cleaner (left), and the interference pattern generated when the mode is superposed with a  $LG_{00}$  mode (right) under an angle.

resonant conditions of the two different sinusoidal modes should therefore be separated by half of the free spectral range of the cavity.

An interesting outcome of this arises when we consider the helical LG modes as a sum of sinusoidal modes, employing Euler's formula  $e^{ix} = \cos(x) + i \sin(x)$ . If the helical modes can be described as a sum of sinusoidal modes, then one expects that when a helical mode is injected into a triangular mode cleaner, the mode cleaner can be tuned to be on resonance for one of the constituent sinusoidal modes, while being anti-resonant for the other. As a result of this we expected that a triangular mode cleaner can be used to decompose a helical LG mode into its sinusoidal components.

Another important difference between linear and triangular mode cleaner cavities is that the latter feature a spherically curved mirror which is probed by the circulating beam under an angle (not normal incidence). This results in a breaking of the symmetry about the azimuthal angle for the mode cleaner eigenmodes. This is not usually a problem for fundamental mode operation, since an astigmatic  $LG_{00}$  mode is still an eigenmode of the cavity. Higher-order LG modes on the other hand are not eigenmodes of astigmatic cavities [BFC<sup>+</sup>11]. The mode shape of even sinusoidal LG beams degenerates upon transmission through a triangular mode cleaner as a result of the astigmatism. There are two possible solutions to this problem; to use linear cavities exclusively, or to design non-astigmatic mode cleaner cavities with four or more mirrors. Some work has

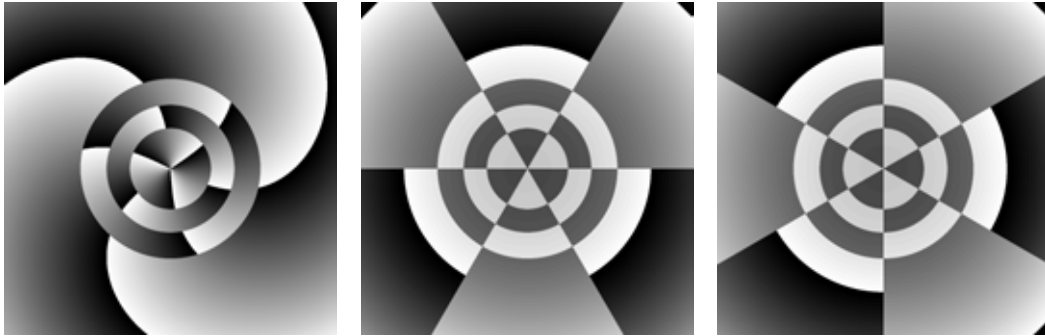


Figure 4.24.: Transverse phase distributions of the helical (left), vertically symmetric sinusoidal (center) and vertically anti-symmetric sinusoidal (right)  $LG_{33}$  modes. The colour represents the phase, in a range from 0 (white) to  $2\pi$  (black).

already been done to design non-astigmatic mode cleaner cavities for fundamental mode operation [Ske05], which should be investigated for use with higher-order LG modes. One possibility may be to implement aspherical mirrors to build a non-astigmatic mode cleaner for higher-order LG modes. It should be noted that using only linear cavities as mode cleaners incurs the additional complication of using polarising optics to extract the control signals in reflection.

In order to experimentally demonstrate these effects, a triangular mode cleaner was placed after the linear mode cleaner, as depicted in figure 4.26. The length of the triangular mode cleaner was scanned while using the sinusoidal  $LG_{33}$  beam and the helical  $LG_{33}$  beam as the input in succession. Figure 4.25 shows the transmitted light power measured for both scans. The helical input scan shows three separate large resonances. It follows from the theoretical understanding that these should correspond, from left to right, to the resonances of the vertically symmetric sinusoidal mode, the vertically anti-symmetric sinusoidal mode, and then the next free spectral range of the vertically symmetric mode <sup>4</sup>.

When the input beam was changed from the helical to the vertically symmetric sinusoidal  $LG_{33}$  mode, the second peak disappeared from the trace. This is as would be expected if the second peak in the helical trace indeed corresponds to the vertically symmetric

<sup>4</sup>The resonances may equally well have corresponded to the anti-symmetric, symmetric, and the next free spectral range of the anti-symmetric modes, but the sinusoidal input mode trace demonstrates otherwise.

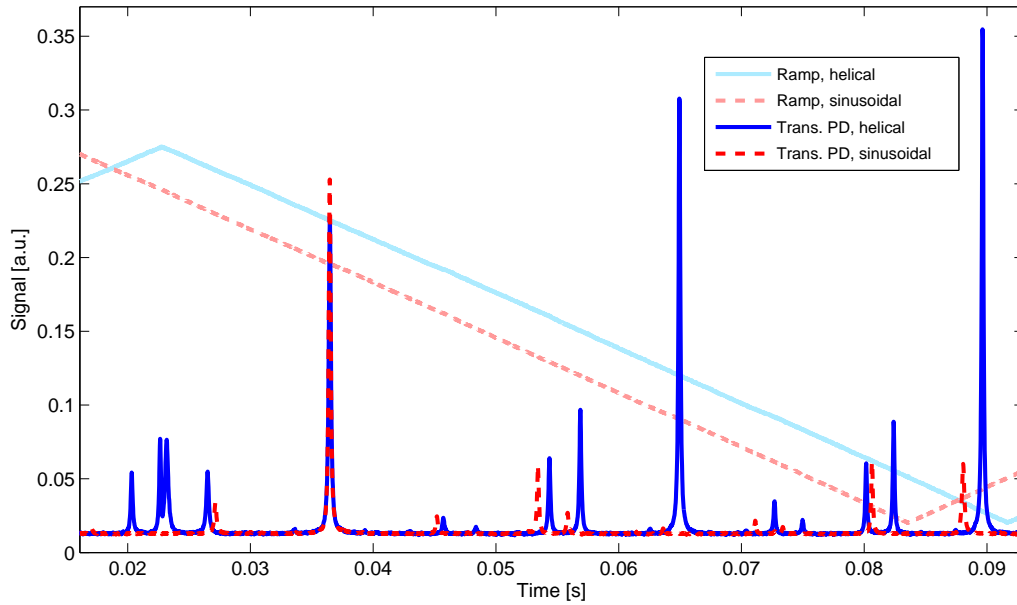


Figure 4.25.: Overlaid scans of the triangular mode cleaner, with helical and vertically symmetric sinusoidal LG<sub>33</sub> input beams. The helical beam trace shows three large peaks, with a total separation of one free spectral range. The first of these peaks is also present in the sinusoidal trace, but the second and third peaks are not. The third peak is absent in the sinusoidal trace due to the temperature drift of the spacer taking the next free spectral range out of the scanning range, but the second peak is absent as it corresponds to the vertically anti-symmetric sinusoidal mode.

mode. The third peak was also not visible in the recorded scan, though this was due to a thermal drift of the mode cleaner spacer taking the second free spectral range peak out of the scanning range. In the figure, the sinusoidal trace has been shifted along the time axis to overlap the first large peak with the corresponding one from the helical case in order to visually compensate for the drift. This can be seen from the shifting of the ramp signal trace, since the trigger level on the oscilloscope was constant throughout.

In order to test the assertion that the first and second peaks in the helical trace corresponded to the vertically symmetric and anti-symmetric modes respectively, we then feedback controlled the triangular cavity in similar fashion to the linear mode cleaner. In this case, however, the length error signal was obtained from the light reflected from the cavity input mirror, following the PDH method.

Intensity profiles of the input, transmitted and reflected beams at one of these resonances are shown in figure 4.26. The beam after the linear cavity was of slightly lower quality than that shown in figure 4.20 as less time was spent optimising the alignment for this experiment. It was observed that the beam transmitted through the triangular cavity on this resonance strongly resembled the vertically symmetric sinusoidal LG<sub>33</sub> mode. The reflected beam is always a superposition of all the modes rejected by the mode cleaner, and is in general therefore of lower mode purity than the transmitted mode. However, it can still be seen that the vertically anti-symmetric LG<sub>33</sub> mode is clearly the dominant mode present in the reflected light.

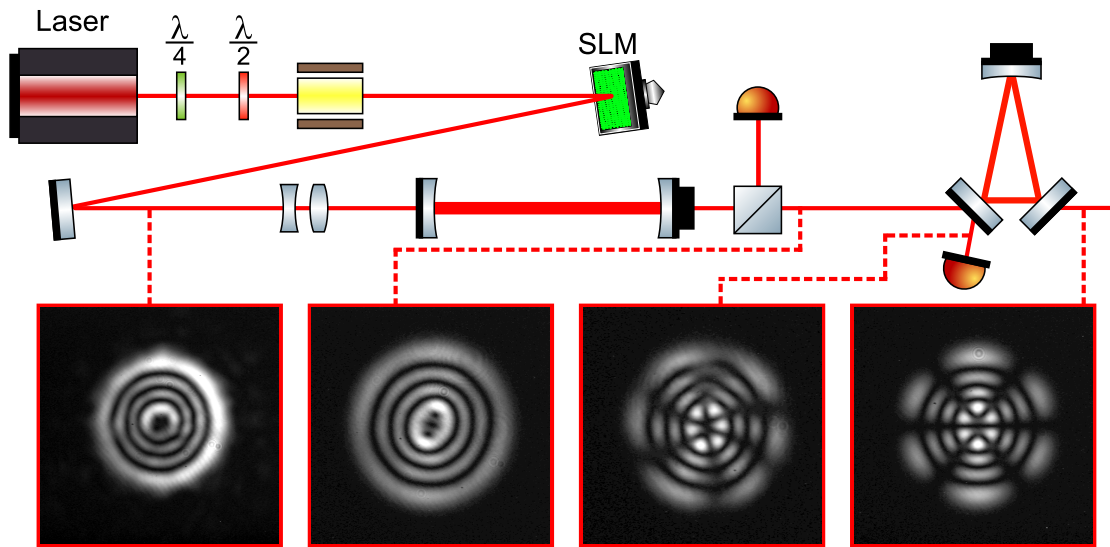


Figure 4.26.: The experimental setup for investigating the interaction of a helical LG<sub>33</sub> mode with a triangular mode cleaner. The intensity profiles of the beams at various locations in the setup are shown, contrast enhanced here to show the main features more clearly. From left to right the images show: helical LG<sub>33</sub> after the SLM, helical LG<sub>33</sub> after transmission through the linear mode cleaner, beam reflected from the triangular cavity and beam transmitted through the triangular cavity.

We repeated the measurement for the alternative resonance point, where as expected we found the dominant types of the transmitted and reflected sinusoidal mode to be reversed. This confirmed our prediction that the helical input beam is decomposed into the constituent sinusoidal modes upon interaction with the triangular mode cleaner.

We can therefore conclude that in order for helical  $LG_{33}$  modes to be compatible with gravitational wave interferometers, the mode cleaners used must be linear, or at least be comprised of an even number of mirrors.

Looking in more detail at the transmitted mode in figure 4.26, it can be seen that the vertical band is brighter than the other bands. We expect that this effect is caused by the astigmatism inherent in the cavity, due to the non-zero angle of incidence of the beam on the curved mirror. The effects of astigmatism and other mirror surface defects on LG modes within cavities are discussed in more detail in section 5.1.

These results show that helical LG modes will be incompatible with the current triangular mode cleaner designs in place for Advanced LIGO, Advanced Virgo and GEO600. In addition, the astigmatism effect is likely to make even the sinusoidal LG modes incompatible with 3 mirror mode cleaners, as discussed further in section 5.1. The incompatibility with triangular mode cleaners constitutes a significant consideration for the overall optical design of the detectors for which LG mode technology is considered.

## Chapter 5.

# Prototype experiments with the $LG_{33}$ mode

Following the largely positive results of the table-top LG mode experiments, we were afforded a fortuitous opportunity to work in collaboration with members of the Glasgow interferometry group towards testing the LG mode technology on the 10 m suspended cavity in Glasgow. Progression from table-top experiments to a prototype experiment with suspended mirrors is a standard feature of the development of new technologies for gravitational wave detectors, in order to ensure compatibility with realistic interferometer subsystems and requirements.

At this point, we had also become increasingly aware of one of the main difficulties that was expected to be encountered with the LG mode technology; LG mode degeneracy and the coupling to degenerate modes caused by mirror surface imperfections. We believe that we had not encountered this problem up to this point due to our use of relatively small beam sizes on the cavity mirrors. On small spatial scales, even off the shelf mirrors such as those used in the linear mode cleaner can be close approximations to ideal spherical surfaces. However, simulations with the  $LG_{33}$  mode in larger cavities with larger beam sizes on realistic mirror surfaces showed this to be a potentially fatal drawback to the use of higher-order LG modes in gravitational wave detectors [BFC<sup>+</sup>11, HMY<sup>+</sup>11].

The most urgently required experiment with LG modes at this point was therefore an analysis of the extent of the degeneracy problem in a larger cavity with larger beam sizes. Performing LG mode experiments at the Glasgow 10 m prototype was thus another opportunity to achieve two goals with one experiment; we could assess the compatibility of the  $LG_{33}$  with the prototype interferometer at large, and since the 10 m cavity geometry is such that the beam sizes at the mirrors are roughly a factor of 5 larger than in our

table-top experiment, we hoped to be able to simultaneously investigate the effects of LG mode degeneracy.

## 5.1. Degeneracy of higher-order Laguerre-Gauss modes

In this section I will give a brief explanation of the LG mode degeneracy problem and its significance for LG mode technology in gravitational wave interferometers. Most of the theoretical work on this issue that has been done in Birmingham has been performed by Charlotte Bond, so a more thorough explanation of this matter is likely to appear in her thesis later on. Some key results of Bond's can also be found in [BFC<sup>+</sup>11].

An important difference between higher-order LG modes and the fundamental  $LG_{00}$  mode is that only the  $LG_{00}$  mode is unique in its mode order. For each higher-order mode there exists at least one other mode of the same order. Since the mode filtering effect of optical cavities relies principally on the round trip Gouy phase difference between different mode orders, as described in section 4.3, they cannot therefore filter out all other modes than the  $LG_{33}$  when on resonance for order 9. For this reason we call the other order 9 modes *degenerate* with the  $LG_{33}$  mode.

This degeneracy of higher-order modes has serious implications for their application in gravitational wave interferometers. In the initial simulations reported in [CHF09] the interferometer mirrors were modelled as perfect spherical curved mirrors. In reality however, the mirrors will have some small deviations from perfect spherical surfaces which can cause coupling from the  $LG_{33}$  mode into other modes of order 9. If we consider this process occurring within the arm cavities of a gravitational wave interferometer, the degeneracy of the modes of order 9 will mean that they can all be resonant at the same time. The mode content of the circulating beam may therefore have a significantly reduced proportion of  $LG_{33}$ , the remainder being made up principally of other order 9 modes. If the mode content of both arm cavities is different, which is likely to be the case if the coupling between modes is driven by the randomly oriented mirror surface distortions, the modal overlap at the beam splitter will be imperfect and the output port contrast will be reduced.

Further complications can arise if the resonance frequencies of order 9 modes in the arm cavities are not exactly equal, but are separated by frequencies less than the cavity linewidth. This can occur because the round trip Gouy phase in a cavity is determined by

the *average* curvature of the mirror surfaces (as well as the mode order), and the average curvature experienced by different spatial modes even of the same order may differ slightly for mirror surfaces which are not perfectly spherical. The average curvature experienced by different spatial modes can differ, since their different intensity profiles will sense certain portions of a mirror surface to a differing degree. If we consider two higher-order HG modes of the same order -  $\text{HG}_{90}$  and  $\text{HG}_{09}$ , it is clear that the round trip Gouy phase of these two modes will be primarily sensitive to the average curvature along two orthogonal axes of the mirror surface. In the case of an astigmatic mirror therefore, the two modes will have different round trip Gouy phases and hence different resonance conditions.

For the case of a  $\text{LG}_{33}$  mode in an astigmatic cavity, it is instructive to consider a decomposition of the mode into HG modes, as described by equation 2.16. In this case, as previously considered, the different HG modes that constitute the  $\text{LG}_{33}$  mode will experience different round trip Gouy phases. After a round trip, therefore, the HG modes will no longer have the same phase relations as required by equation 2.16. Performing the reverse decomposition from HG modes to LG modes, one will find the mode content in the LG base system changed from a pure  $\text{LG}_{33}$  mode to a mix of order 9 modes. In addition to this, the different constituent HG modes will have different resonance frequencies, as previously described for  $\text{HG}_{90}$  and  $\text{HG}_{09}$ , leading to the splitting of even a pure  $\text{LG}_{33}$  mode into several ‘pseudo-degenerate’ mode peaks. This effect was experimentally demonstrated in a 10 m suspended cavity, as described in section 5.4. The frequency splitting effect between  $\text{HG}_{10}$  and  $\text{HG}_{01}$  modes has previously been used to estimate the astigmatism of a 40 m cavity at the Caltech prototype gravitational wave detector facility in [AAS08].

In the case where several modes of the same order have resonant frequencies in a cavity which are separated by less than the cavity linewidth, the error signal will have multiple nearby zero crossings. This can make the arm cavities difficult to control, since the linear range of the error signal will be reduced, and mode ‘hopping’ between these pseudo-degenerate modes may occur.

The method and results of a detailed numerical and analytical investigation into the effect of mirror surface distortions on the purity of LG modes within optical cavities were presented by Bond at the 2011 Amaldi meeting, and in [BFC<sup>+</sup>11], and another study on this topic is presented in [HMY<sup>+</sup>11]. One of the most important outcomes from the

work described in [BFC<sup>+</sup>11] was the derivation of an analytical formula for predicting the amount of coupling between different LG modes upon reflection from a mirror, based on the spatial features of mirror surfaces as described by Zernike polynomial functions. In the limit that the height of the surface distortions is much smaller than the wavelength of the light, coupling between an incident mode  $LG_{pl}$  and a reflected mode  $LG_{p'l'}$  is only significantly caused by Zernike polynomials  $Z_n^m$  which satisfy the condition  $m = |l - l'|$ . Based on this result, it was possible to propose limits on the heights of the most important low order Zernike polynomial present on mirror surfaces, in order to achieve a circulating mode purity of over 99.9% [BFC<sup>+</sup>11].

Experiments at the Glasgow prototype give us a way to investigate the LG mode degeneracy problem heretofore only looked at theoretically and numerically. Though we did not observe the detrimental effects of the mode degeneracy problem in our table-top experiment we believe this is most likely due to the relatively small beam sizes used on the mirrors, and the low cavity finesse in comparison to the advanced detector arm cavities. However, it is clear that LG modes must also work with larger beam sizes in order to provide the thermal noise benefits that make them attractive in the first place. LG modes must also be compatible with cavities of similar finesse to the advanced detector arm cavities. We have therefore carried out experiments with the  $LG_{33}$  mode at the Glasgow 10 m prototype facility which uses larger beam sizes in a higher finesse cavity.

## 5.2. Design and manufacture of an etched diffractive optic for mode conversion

For the 10 m prototype experiment we used a diffractive optic element (DOE) to facilitate the conversion from  $LG_{00}$  to  $LG_{33}$ , rather than the SLM used in the table-top experiments. While the SLM was very useful for prototyping purposes to investigate the effects of different phase profiles, a fixed transmissive optic allows for the generation of a higher mode purity at a higher laser power, with greater efficiency and stability than the SLM. The design of the phase profile for the DOE was very similar to those used with the SLM to generate  $LG_{33}$  modes. We opted for a non-amplitude contoured phase profile, to maximise the amount of light power that would remain in the desired diffraction order. Some of the main design specifications of the DOE are shown in table 5.1.

Element area	$30 \times 30 \text{ mm}^2$
Structured area	$21 \times 21 \text{ mm}^2$
Thickness	3.05 mm
Pixel aspect ratio	$3000 \times 3000$
Pixel depth quantisation	$2\pi$ over 8 levels
Pixel size	$7 \mu\text{m}$
Off axis angle	2.51 mrad
Input beam size	3.5 mm

Table 5.1.: Design specifications for the DOE used on the LG mode conversion bench at the Glasgow 10 m prototype.

Several factors were considered when choosing the angle into which the desired beam is diffracted, known as the ‘off axis angle’. First of all, a non-zero off axis angle is required in order to separate the desired mode from the unmodulated light. In the SLM setup, the unmodulated light was mainly considered to be a result of direct reflection from the front surface of the SLM. However, in the transmissive configuration used for the DOE, the dominant source of unmodulated light is from fabrication tolerances in the etching depth [Sch]. The off axis angle must be large enough so that the beams in 0th and 1st orders do not overlap after a practical propagation distance. In practice this means that the off axis angle should be larger than the sum of the divergence angles of the 0th and 1st order beams, each given by  $\Theta = \arctan\left(\frac{\lambda}{\pi w_0}\right)$ . For the case of a 3.5 mm  $\text{LG}_{00}$  beam interacting with the DOE at the waist position, this gives a minimum off axis angle of 1.22 mrad.

The off axis angle should not be made arbitrarily large, however, as limitations in the pixel resolution become a larger source of error for larger off axis angles. This is because for larger off axis angles the grating rulings are closer together, and thus the quantisation error per ruling is greater in both the transverse and depth axes. We verified this by analysing the results of FFT simulations performed at Jenoptik for three different off axis angle designs. We used the same analysis method as described in section 3.2.3 to decompose the field within the desired diffraction order into the constituent LG modes. The power content in each of the order 9 modes is shown in table 5.2 for each of three different off axis angles. The greatest  $\text{LG}_{33}$  mode content was found to be generated by the 2.51 mrad off axis angle design, and the least was found to be generated by

the 5 mrad design. In addition to this the 2.51 mrad design also generated the least power in other order 9 modes, about which we were particularly concerned due to their degeneracy with the  $LG_{33}$  mode in optical cavities. For this reason we chose to use the 2.51 mrad off axis design.

Mode indices		Power content (%)		
$p$	$l$	2.51 mrad	3.76 mrad	5.0 mrad
3	3	87.2	86.9	85.1
4	1	$1.06 \times 10^{-5}$	$1.20 \times 10^{-4}$	$3.40 \times 10^{-3}$
2	5	$1.05 \times 10^{-5}$	$9.90 \times 10^{-5}$	$3.16 \times 10^{-3}$
1	7	$4.80 \times 10^{-6}$	$1.05 \times 10^{-6}$	$2.65 \times 10^{-5}$
0	9	$4.38 \times 10^{-6}$	$2.62 \times 10^{-7}$	$2.54 \times 10^{-5}$
0	-9	$4.36 \times 10^{-6}$	$1.39 \times 10^{-6}$	$3.72 \times 10^{-5}$
2	-5	$3.60 \times 10^{-6}$	$9.56 \times 10^{-7}$	$5.14 \times 10^{-6}$
1	-7	$3.42 \times 10^{-6}$	$2.66 \times 10^{-7}$	$1.10 \times 10^{-5}$
4	-1	$2.43 \times 10^{-6}$	$1.77 \times 10^{-7}$	$5.76 \times 10^{-6}$

Table 5.2.: Table showing the power present in LG modes of order 9 in the simulation of DOE  $LG_{33}$  conversion, for three different off axis designs. The 2.51 mrad off axis angle design performs the best, with the most power in the  $LG_{33}$  mode and the least power in other modes of order 9.

### 5.3. $LG_{33}$ conversion bench at the Glasgow 10 m prototype

The setup for the  $LG_{33}$  mode conversion bench is shown in figures 5.1 and 5.2. The beam is picked off from the previously used laser path (shown in purple) after a fibre output coupler, and directed with a flip mirror into the LG mode conversion area. The red path shows the  $LG_{33}$  mode conversion path, in which the beam passes through an EOM for generating the control sidebands, and the DOE. The resulting beam is then transmitted through a linear mode cleaner, which is feedback controlled using the PDH method to remain on resonance for mode order 9. This serves to increase the mode purity of the beam, in a similar method to that described in section 4.3. The transmitted beam is then passed back into the previously used laser path using another flip mirror, and on towards the suspended cavity. The green path is a DOE bypass path, which enables us

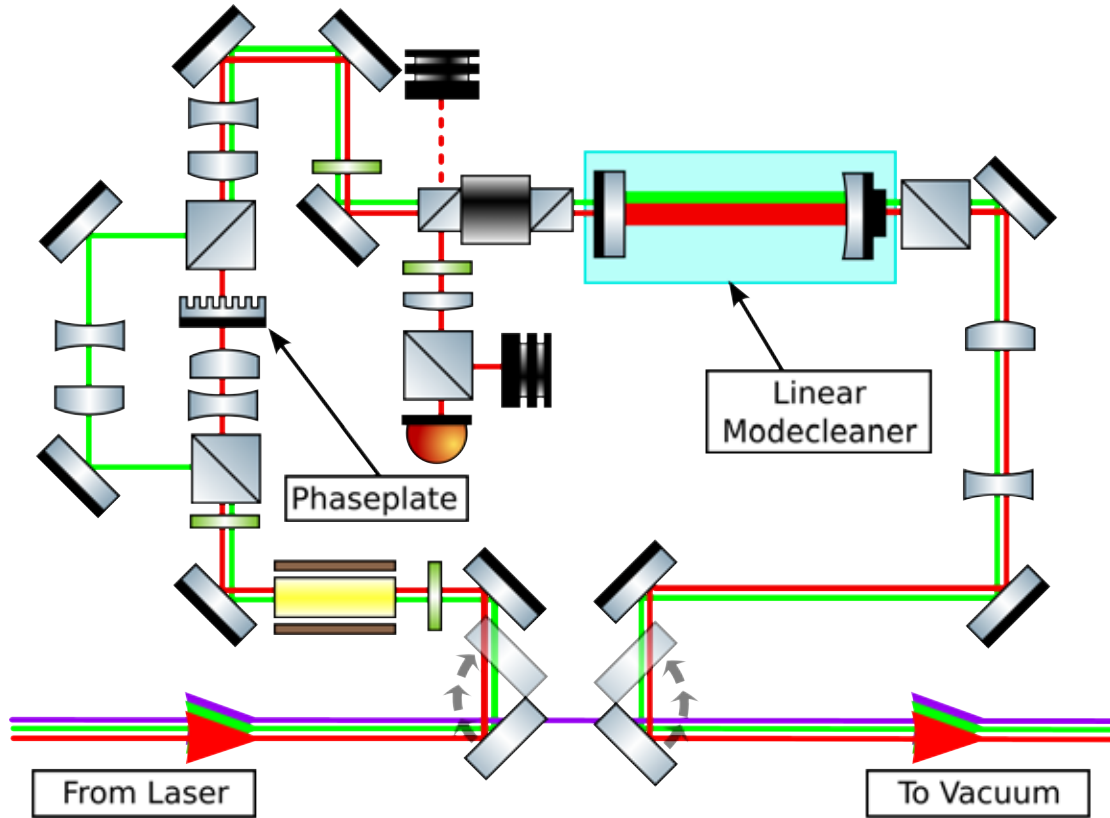


Figure 5.1.: Schematic of the laser mode conversion path on the Glasgow 10 m prototype input optics bench. The red line shows the  $LG_{33}$  mode path, and the green line shows the  $LG_{00}$  path that bypasses the phaseplate. The purple line shows the original  $LG_{00}$  laser path.

to alternatively operate the linear mode cleaner with the  $LG_{00}$  mode. The idea of this path was to ensure a fair comparison between the performance of the  $LG_{00}$  and  $LG_{33}$  modes in the suspended cavity. Since the light transmitted by the mode cleaner must be defined by the cavity eigenmodes, the transmitted  $LG_{00}$  and  $LG_{33}$  beams should have the same alignment and mode matching relative to the suspended cavity. The hope was that this would enable us to make a valid assessment of the relative performance of the two modes within the suspended cavity. It transpired later, however, that the beam parameters of the  $LG_{33}$  mode and the  $LG_{00}$  mode after transmission through the linear mode cleaner were not exactly the same. This was determined by making a series of measurements of the beam size at different positions after the mode cleaner for both modes, and fitting the Gaussian beam divergence function to the measurements to

extract the beam waist size and position. Figure 5.3 shows the fit results for the  $LG_{33}$  mode.

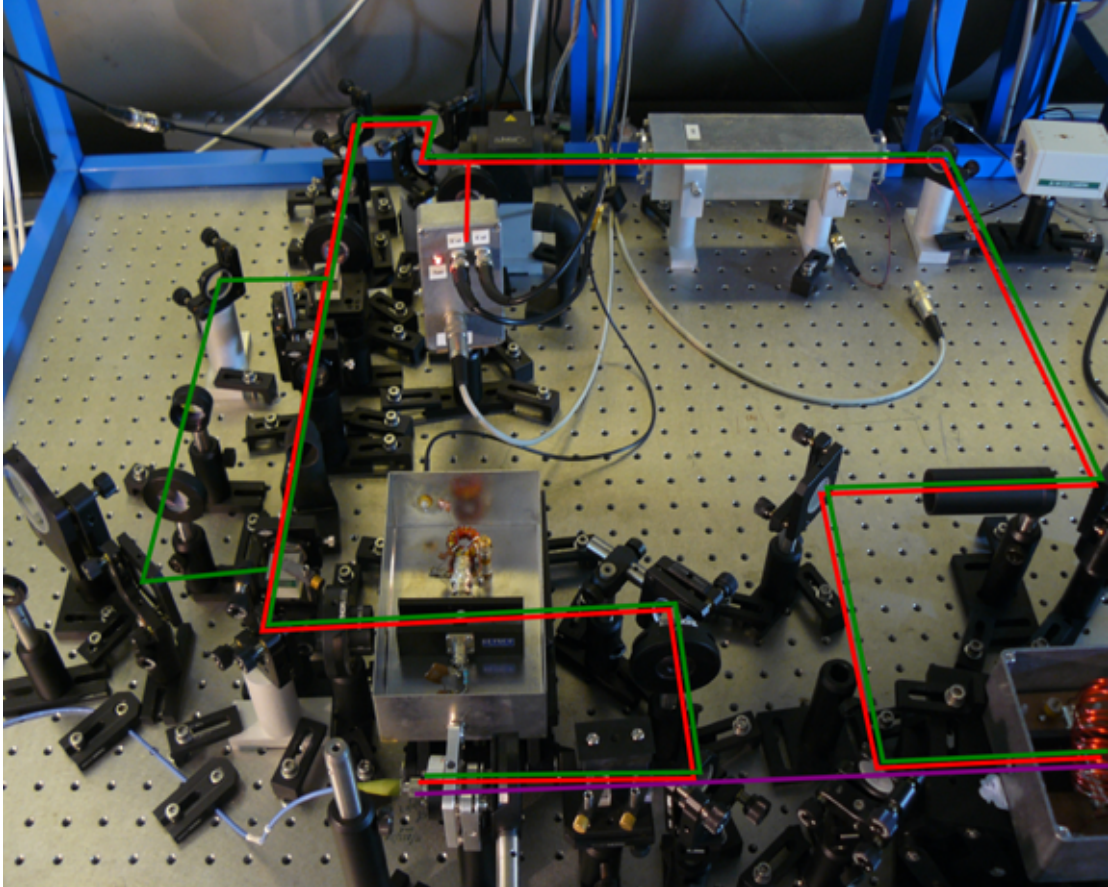


Figure 5.2.: The laser mode conversion path on the Glasgow 10 m prototype input optics bench. The red line shows the  $LG_{33}$  mode path, and the green line shows the  $LG_{00}$  path that bypasses the phaseplate. The purple line shows the original  $LG_{00}$  laser path.

After passing through the linear mode cleaner, the beam is directed back into the original  $LG_{00}$  laser path. Before passing into the vacuum system, the beam is passed through numerous optical components on the laser bench. First of all, the beam is transmitted through an EOM, which is used to imprint 15 MHz sidebands on the light. The beam subsequently passes through a Faraday isolator, in place to minimise the amount of light reflected back to the laser. The original laser path on the bench was designed to accommodate the  $LG_{00}$  beam, which has a less extended intensity profile than the  $LG_{33}$

### 5.3. $LG_{33}$ conversion bench at the Glasgow 10 m prototype

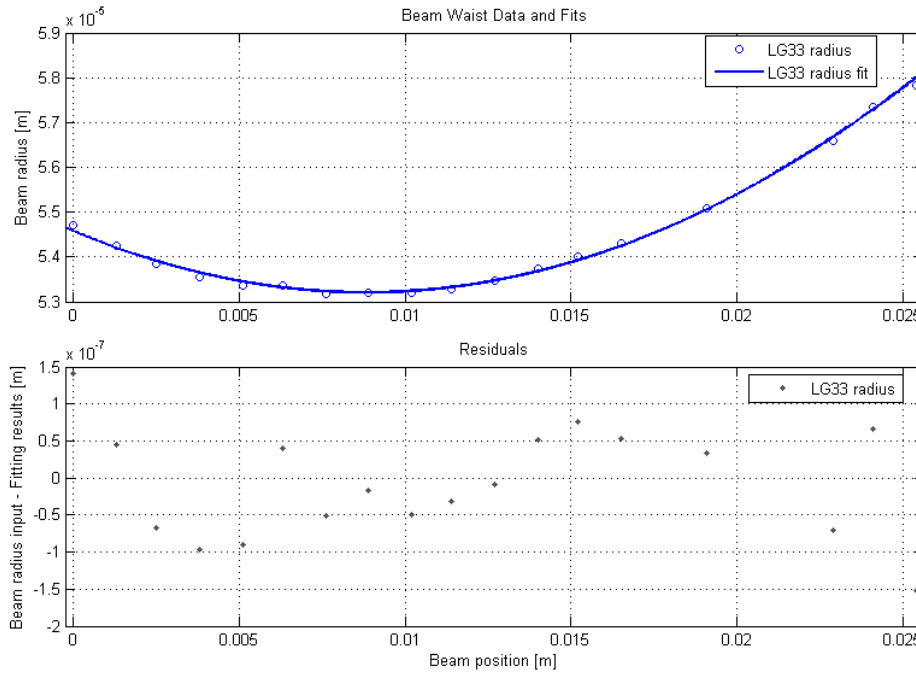


Figure 5.3.: Data points and fit for the beam waist size and position of the  $LG_{33}$  after the linear mode cleaner. Plot courtesy of B. Sorazu.

beam. As a result of this, in many places the  $LG_{33}$  beam was close to the point of clipping at the edges of some of the apertures through which it was required to pass. This additional design constraint should be taken into account in any future applications of higher-order LG mode technology; apertures which are sufficient for the  $LG_{00}$  mode may not be sufficient for the  $LG_{33}$  mode. In addition to this, we found the  $LG_{33}$  beam to be more sensitive to the imperfections in the transmissive optics along the laser bench path.

After passing through all the transmissive optics, the intensity profile of the  $LG_{33}$  mode had significantly deteriorated, as shown in figure 5.4. This had a significant impact on the experiment, because it introduced another uncontrollable variable; we could no longer be sure that phenomena observed in the 10 m cavity with the rough  $LG_{33}$  beam were a consequence of the fundamental interaction of the  $LG_{33}$  mode with the cavity rather than a consequence of the distortions already present in the beam.

Cavity length	$9.812 \pm 0.001$ m
Free spectral range	$15.277$ MHz $\pm 1.6$ kHz
Input test mass power transmission	1.3 %
End test mass power transmission	6 ppm nominal
Input test mass radius of curvature	$\infty$ nominal
End test mass radius of curvature	15 m nominal
Cavity beam waist size	1.55 mm
Transverse mode spacing	4.58 MHz
Modulation sideband frequency	15 MHz
Cavity Finesse	600 Nominal

Table 5.3.: Relevant parameters of the 10 m suspended cavity in Glasgow.

#### 5.4. 10 m cavity performance with the $LG_{33}$ mode

One of the main aims of this work was to investigate the LG mode degeneracy effect in the 10 m suspended cavity. Table 5.3 shows some of the relevant parameters for the 10 m cavity. After the EOM and the Faraday isolator, the beam is passed through a mode matching telescope in order to match the beam to the cavity eigenmode. As illustrated in figure 3.7, the task of accurately mode matching the  $LG_{33}$  mode to a cavity is more delicate than for the  $LG_{00}$  mode. Such was the difficulty of this task for the  $LG_{33}$  mode that we found the dominant mode order present when the  $LG_{33}$  beam was injected into the cavity to be not order 9, but rather orders 7 or 11. The dominant mode orders were determined by taking high speed video footage of the beam transmitted through the cavity as the cavity was scanned. It was through these measurements that we also found that the mode shapes at the resonant tunings in the cavity resembled HG modes much more closely than LG modes.

Since the purity of the  $LG_{33}$  beam injected into the cavity had been degraded by the transmissive components, and the mode matching into the cavity was also apparently not good enough to achieve a dominant order 9 resonance in the cavity, it is difficult to draw strong conclusions about the performance of the  $LG_{33}$  mode in the 10 m cavity. Nevertheless, we observed scans of the cavity with the rough  $LG_{33}$  beam as the input beam. Figure 5.5 shows the transmitted light power through the cavity as the cavity is scanned, for both the  $LG_{00}$  and  $LG_{33}$  modes. Since both modes were transmitted

through the same linear mode cleaner cavity, they should have the same beam parameters at the point of entry into the cavity. However, comparing the transmitted light power traces for  $LG_{00}$  and  $LG_{33}$  modes over the scans shown in figure 5.5, we see that significantly more power is present in mode orders other than the dominant order for the  $LG_{33}$  case. This is to be expected, since the  $LG_{33}$  is expected to be more sensitive to mode mismatch than the  $LG_{00}$ , as shown in figure 3.7. It should be noted, however, that the degradation of the beam profile due to the effects of passing through the EOM and Faraday isolator may also contribute to the increased presence of modes in orders other than the injected mode for the  $LG_{33}$  case. It is also the case that the beam parameters were not exactly the same for the  $LG_{33}$  and  $LG_{00}$  modes transmitted through the linear mode cleaner.

Figure 5.6 shows close-ups of the dominant mode order peak, for both the  $LG_{00}$  case and the  $LG_{33}$  case. The dominant peak when the cavity was injected with the  $LG_{00}$  mode, shown in the upper part of figure 5.6, follows the expected Lorentzian shape, and definitely consists of just one peak. On the other hand, the dominant peak when the cavity was injected with the  $LG_{33}$  mode has a much more exotic structure, as shown in the lower part of figure 5.6. Figure 5.7 shows 4 of the dominant peaks from a scan of the cavity with the  $LG_{33}$  mode as the input beam. Each of these peaks is separated in the scan by one FSR, and yet we see that the main features are common to each peak. The repetition of this structure across many free spectral ranges of the cavity demonstrates that the structure is not merely a measurement artefact, but is in fact a genuine feature of the cavity response when pumped with the  $LG_{33}$  mode. The multiple, or ‘split’, peak is a feature common to cavities with imperfect mirror surfaces operated with higher-order modes. Similar peak structures were observed in simulations of the  $LG_{33}$  mode in cavities which included astigmatism of the mirror surfaces, as described in section 5.1.

We made high speed recordings of the beam transmitted through the cavity in order to observe the beam shape across the dominant split resonance. We found that each visible mode shape across the scan appeared to have more in common with HG modes than LG modes; little or no circular symmetry was observed, but rectangular symmetries in the intensity patterns were apparent. Figure 5.8 shows some of the observed mode shapes as the cavity was swept over the split resonance. The arrows in figure 5.8 indicate the rough position on the scan to which the different mode images correspond. The rectangular symmetry in each of the three brightest modes is clear. There is also a clear

change in the orientation of the modes across the peak; the bright mode on the left side is more spatially extended along the horizontal axis, similar to a HG<sub>70</sub> mode, whereas the bright mode on the right side is more spatially extended along the vertical axis, similar to a HG<sub>07</sub> mode. This behaviour is exactly what would be expected for a LG mode in an astigmatic cavity, as described in section 5.1; an astigmatic cavity does not have the required circular symmetry to support higher-order LG eigenmodes.

In order to test whether the cavity truly was astigmatic or not, we decided to make independent measurements of the cavity mirror surfaces. The input test mass surface figure was measured using a Wyko optical profiler. This measurement method was suitable for the input mirror due to its small size (1" diameter) and near flat curvature. The results from the Wyko optical profiler measurement gave the radius of curvature along the horizontal axis as 7077 m, and the radius of curvature along the vertical axis as -1997 m. The same method was not suitable for the end test mass, however, due to its much larger size and stronger curvature. Instead, the astigmatism of the end mirror was estimated using the Ronchi method, originally developed for measuring the astigmatism of telescope mirrors [AP29]. The Ronchi test gave the result that the difference between the end mirror radii of curvature in the vertical and horizontal planes was  $5.3 \text{ cm} \pm 0.5 \text{ cm}$ .

We performed FINESSE [FHL<sup>+</sup>04] simulations of the 10 m cavity with these estimates of the astigmatism, to check for similarities with the measured scans. Due to the mode mismatching problem, and our observation that order 7 modes appeared to be dominant in the cavity, we ran the simulation with a range of different input LG modes to see if they matched the data better than the LG<sub>33</sub> mode. Figure 5.9 shows the results of four such simulations, with each of the LG<sub>33</sub>, LG<sub>23</sub>, LG<sub>43</sub> and LG<sub>31</sub> modes injected into the cavity. Only the LG<sub>23</sub> result, and to a lesser extent the LG<sub>33</sub> result, reproduce the main features of the measured peak scan shown in figures 5.6 and 5.7.

The analysis of the performance of the LG<sub>33</sub> mode in the 10 m cavity is still work in progress at the current time, but we expect to be able to conclude the work within the next few months. At this stage however, I don't believe any strong conclusions can be drawn from this experiment which either verify or disprove the results of the simulation studies into the effects of LG mode degeneracy in cavities with larger beam sizes than those used in our table-top experiments. Unfortunately the degradation of the input mode and the poor mode matching of the cavity have so far made it very difficult to

get a precise agreement between observations and the simulations, and there are many degrees of freedom in the experiment which make it hard to pinpoint the effects due to the use of the  $LG_{33}$  mode itself. What we can conclude so far, however, is that the  $LG_{33}$  mode was not resonating in the 10 m cavity with any appreciable mode purity. In the future however, with mirror surface figures improved in line with the requirements stated in [BFC<sup>+</sup>11], and a more dedicated input laser path with extra clearances allowing for the larger spatial extent of the  $LG_{33}$  mode, the picture might look more positive.

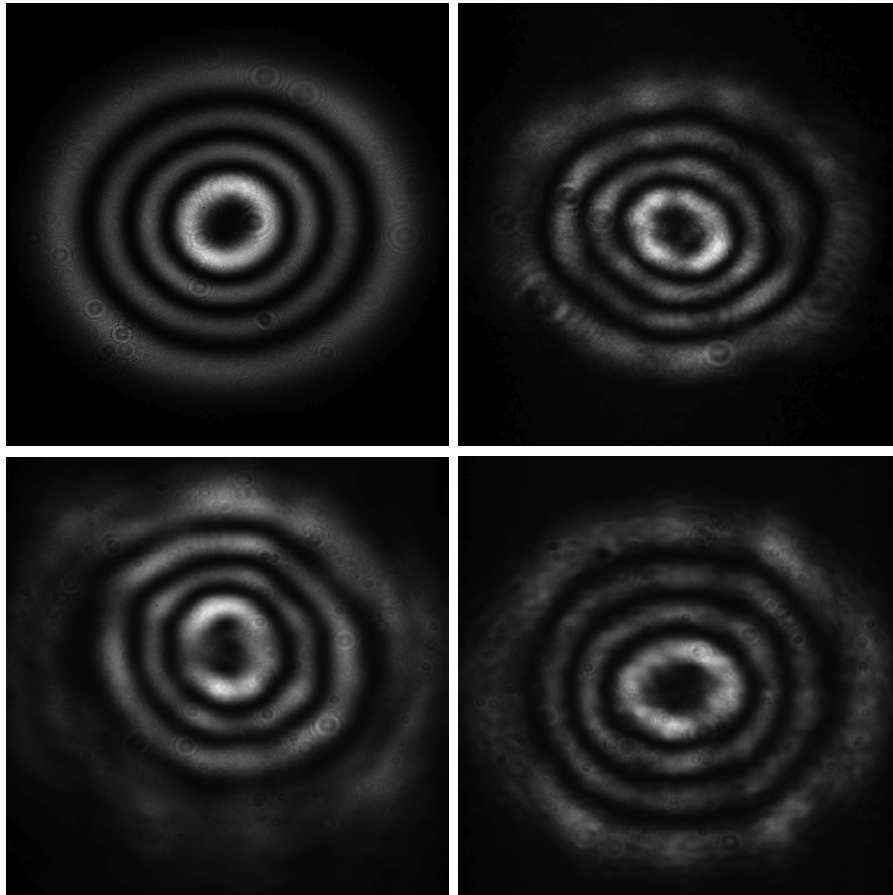


Figure 5.4.: Images of the  $LG_{33}$  beam along the path before entering the 10 m cavity. Clockwise from top left: The beam directly after the linear mode cleaner; the beam after the Faraday Isolator; the beam after the first mode matching lens; the beam just before the 10 m cavity input mirror (after a lens to focus the beam to within the CCD active area). A degradation of the beam purity is observed along the path to the 10 m cavity.

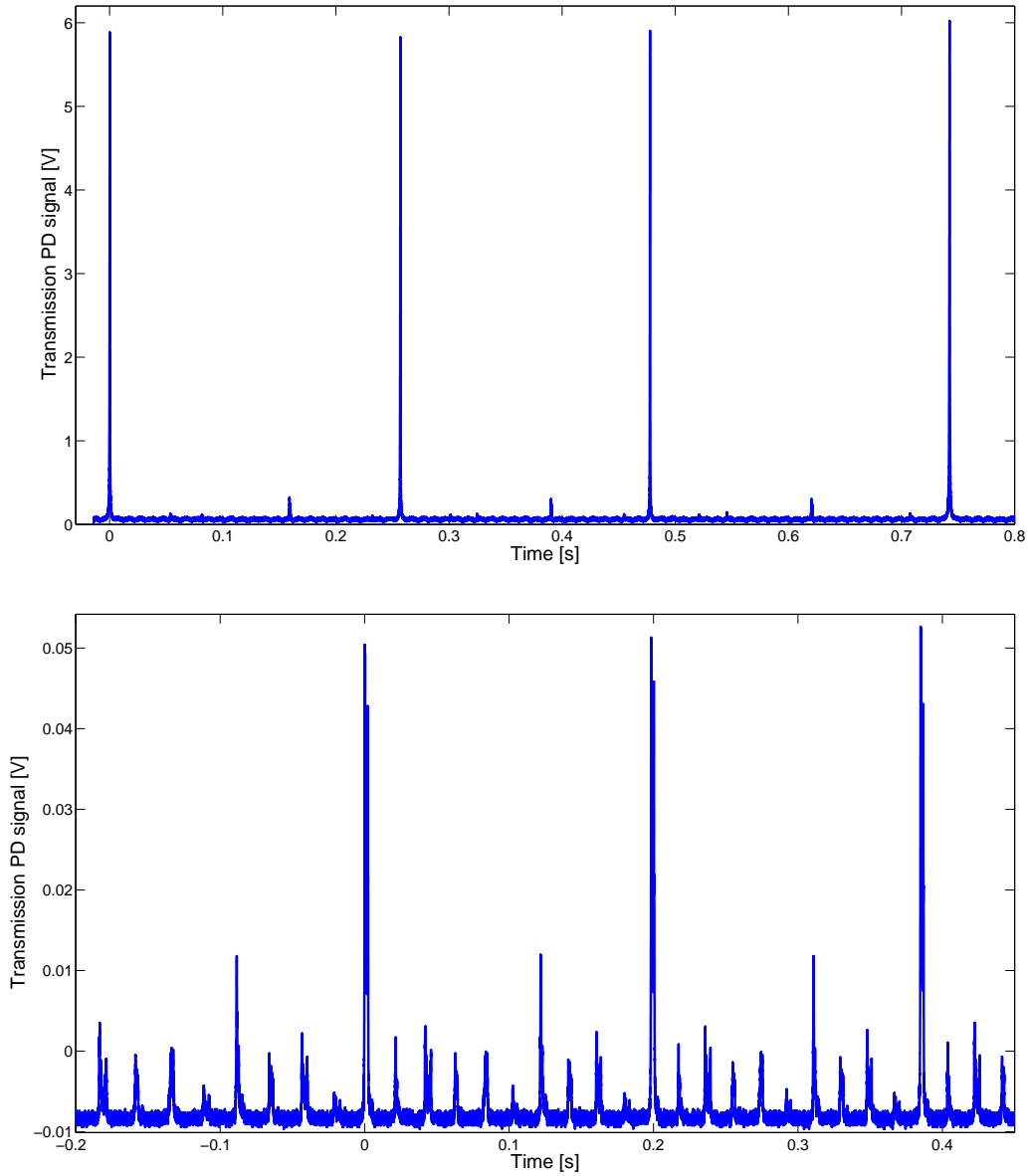


Figure 5.5.: Scans of the 10 m cavity with the  $LG_{00}$  mode (top) and the  $LG_{33}$  mode (bottom), each over roughly 3 free spectral ranges. The cavity was scanned by actuating on the temperature of the laser crystal, thus detuning the frequency of the light passed into the cavity. The top scan shows three visible peaks per free spectral range; the dominant one corresponds the  $LG_{00}$  mode. The lower scan shows considerably more visible peaks, and less contrast between the dominant peak and the other peaks than for the  $LG_{00}$  input case.

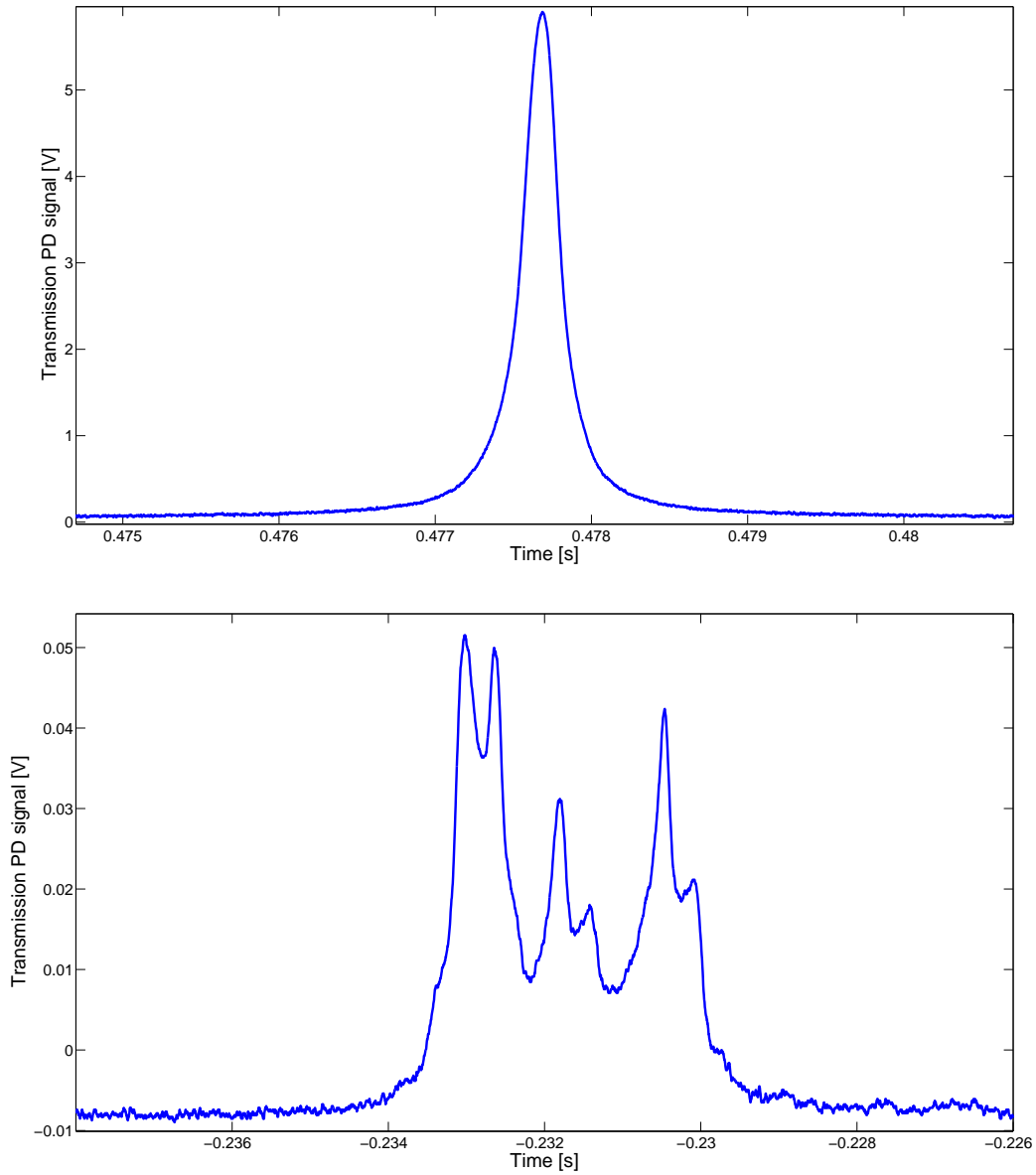


Figure 5.6.: A closer look at the dominant peaks in the cavity scans shown in figure 5.5. The upper plot shows the  $LG_{00}$  peak, which follows the theoretically expected Lorentzian function, and is comprised of just a single visible peak. The lower plot shows the dominant peak when the cavity was scanned with the  $LG_{33}$  mode. Due to difficulties with accurately mode matching the  $LG_{33}$  input, it is believed that the dominant peak is not the order 9 peak.

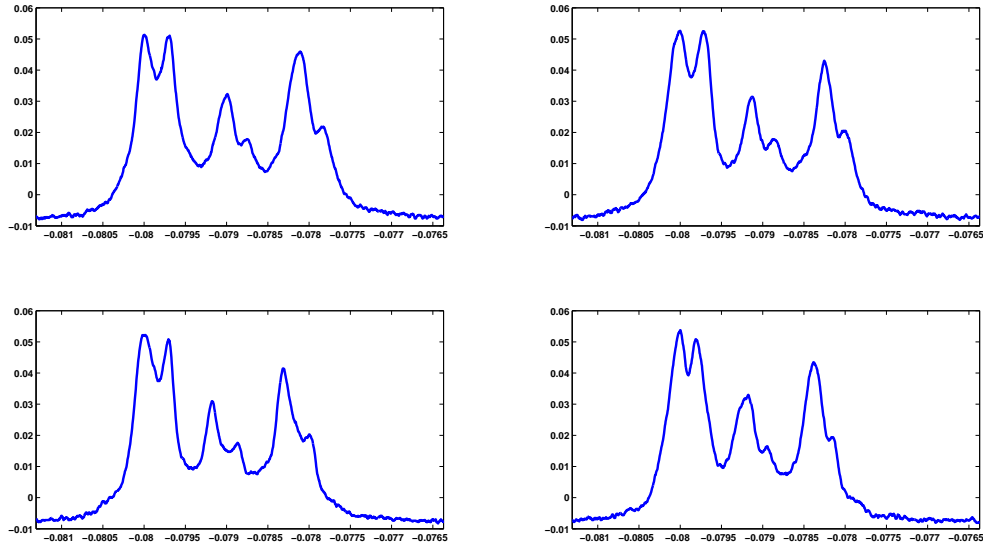


Figure 5.7.: The dominant peaks of four successive FSRs of the 10 m cavity when scanned with the  $LG_{33}$  mode as the input beam. The main features of the split peak are common to each FSR, indicating that the structure is a genuine feature of the cavity response.

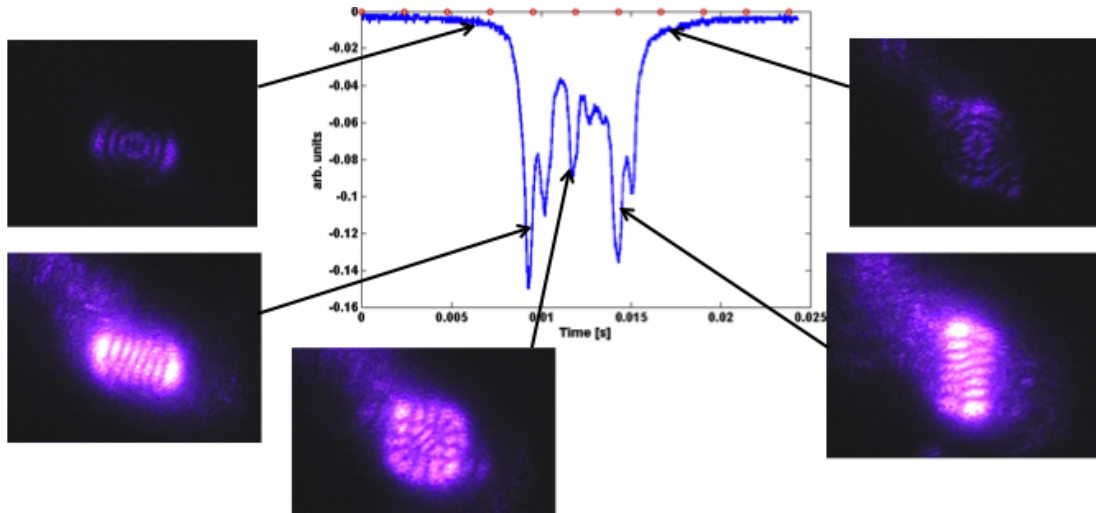


Figure 5.8.: Mode shapes in the beam transmitted through the cavity, recorded with the high-speed camera and overlaid on the split LG mode resonance peak. The red dots on the cavity scan x-axis indicate the frame rate of the camera. Image courtesy of B. Sorazu.

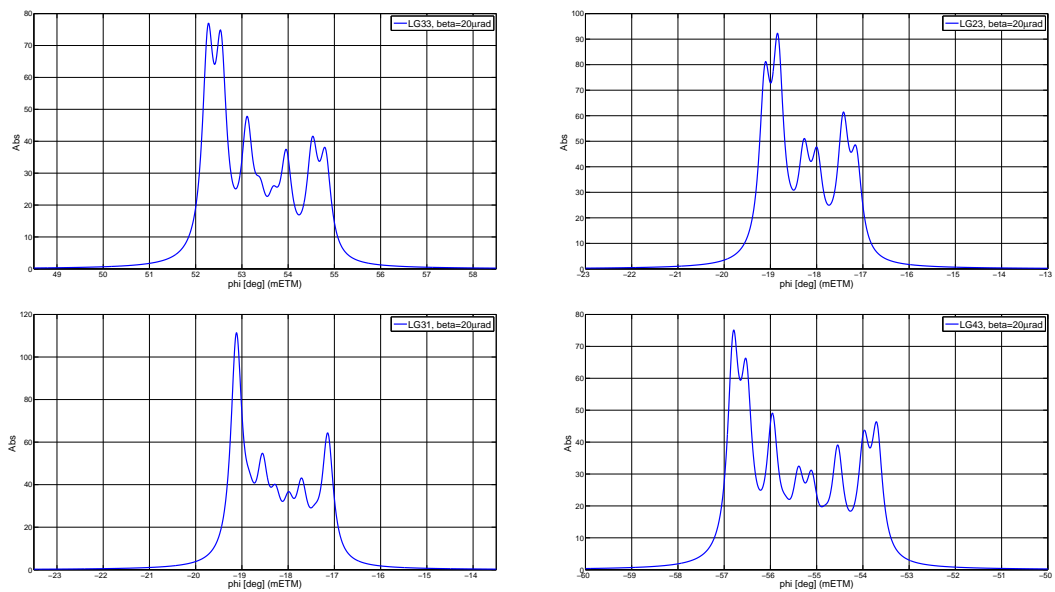


Figure 5.9.: Astigmatic cavity simulations with four different cavity unput modes. The astigmatism used in the simulation was informed by measurements of both cavity mirrors. A small misalignment of  $20\mu\text{rad}$  was applied to the end mirror in order to recreate the measured asymmetry of the dominant peak in the cavity scan. Clockwise from top left:  $LG_{33}$ ,  $LG_{23}$ ,  $LG_{43}$   $LG_{31}$ . The  $LG_{33}$  and  $LG_{23}$  peaks best approximate the measured data shown in figures 5.7 and 5.6.

# Chapter 6.

## Summary and conclusions

### 6.1. Summary

In this thesis I have described the course of my investigations into the use of higher-order LG modes for precision interferometry. The motivation for using higher-order LG modes in place of the currently used  $LG_{00}$  mode comes from their improved test mass thermal noise performance, as described in sections 2.6 and 2.7.

Throughout the course of my PhD studies I have helped to progress higher-order LG mode technology in the context of gravitational wave interferometry from the initial motivation, to a solid foundation based on demonstrated compatibility with some of the key interferometric techniques of the field.

In the initial simulation study into the interferometric performance of the  $LG_{33}$  mode reported in 3.1, it was shown that the  $LG_{33}$  mode is compatible with the PDH longitudinal control scheme and the Ward technique for alignment control. For the Advanced Virgo-like case considered, it was also shown that the  $LG_{33}$  mode performed better in terms of all investigated noise couplings than the  $LG_{00}$  mode with the equivalent clipping loss at the cavity mirrors, as published in [CHF09].

In the table-top experiments with the  $LG_{33}$  mode, I demonstrated the generation of multiple different  $LG_{pl}$  modes of both the helical and sinusoidal form. I have also demonstrated for the first time the locking of an optical cavity to a higher-order  $LG_{33}$  mode using RF modulation/demodulation techniques, as well as demonstrating the increase in mode purity of a  $LG_{33}$  beam upon transmission through a linear mode cleaner cavity to over 99%. I also demonstrated experimentally for the first time the decomposition of

a helical  $LG_{33}$  mode into its constituent sinusoidal modes by means of interaction with a three-mirror optical cavity. These results were published in [FKCF10].

My most recent contributions to LG mode research have been as part of a collaboration between the Birmingham and Glasgow interferometry groups to test LG mode technology on a suspended 10 m cavity. I designed and installed the  $LG_{33}$  mode conversion path on the JIF laser injection bench, and assisted throughout the ongoing investigations into the performance of the  $LG_{33}$  mode in the 10 m cavity. These investigations are still underway currently, but the preliminary results have already raised some interesting issues that should be considered in the future when designing larger scale implementations of LG mode technology.

## 6.2. Conclusions and outlook

The conclusions in terms of the compatibility of LG modes with gravitational wave interferometers are largely positive; one of the most crucial control schemes in the field, the PDH method, has been proven to work with the  $LG_{33}$  mode in both numerical investigations and table-top experiments. The Ward technique for alignment sensing has been shown to work with the  $LG_{33}$  mode in numerical investigations, though it remains for this to be demonstrated experimentally. We have demonstrated a method for producing extremely pure  $LG_{33}$  modes by using a linear mode cleaner cavity to filter out the light in unwanted modes left over from the conversion process. Although I did not report on the work within the main body of the thesis, I have been involved in work towards developing a high-power  $LG_{33}$  laser source in collaboration with colleagues from Birmingham and members of the AEI in Hannover, where over 50 W of light has been produced in the  $LG_{33}$  mode with high purity. This progress suggests that a potential high-power  $LG_{33}$  mode light source for gravitational wave detectors is not too distant a prospect.

On the negative side, the helical  $LG_{33}$  mode has been shown to be incompatible with the triangular mode cleaner design commonly used in gravitational wave interferometers. We have also seen that the  $LG_{33}$  mode is very sensitive to any astigmatic effects. In particular, the degeneracy of higher-order LG modes and the inter-coupling between degenerate modes caused by mirror surface distortions is the biggest problem to be overcome before the technology looks like a truly viable option for inclusion in future

detector designs. Having said that, Bond has calculated the mirror requirements that would be necessary to achieve an acceptable circulating mode purity within the arm cavities of gravitational wave detectors, and so to some extent for the time being the fate of higher-order LG mode technology for gravitational wave interferometers lies in the hands of mirror manufacturers.

In this thesis I have focused on the impact and performance of higher-order LG modes within the field of gravitational wave interferometry, but the thermal noise improvements they offer may also be useful in other areas where thermal noise of optical readouts is a limiting factor, such as for example in the development of ultra-stable optical clocks. In different fields, the degeneracy of LG modes may be less of a problem. For example if the beam sizes are by necessity small, a thermal noise advantage could still be provided over the  $LG_{00}$  mode by exchanging it for a higher-order LG mode.

For future work on LG mode technology, there are still many interferometric performance tests to be done. A demonstration of automatic alignment of a cavity using the Ward technique with the  $LG_{33}$  mode would be an interesting experiment, as would be the operation of a coupled cavity system such as a power recycled Michelson or a Fabry-Perot Michelson with the  $LG_{33}$  mode. There are plenty of interesting advances to be made on the table-top with LG modes before the mirror manufacturers catch up to the requirements for full scale detectors.



## Appendix A.

# Thermal noise scaling factors for higher-order modes

### A.1. Laguerre-Gauss mode thermal noise scaling factors

#### Coating Brownian noise

The coating Brownian noise improvement factors for higher-order LG modes over the LG<sub>00</sub> for a 1 ppm clipping loss are shown in table 2.3. The reduction factors for coating Brownian thermal noise were given precedence in the main part of this thesis because, as shown in figure 2.1, this noise is expected to be the largest of the test-mass thermal noises in Advanced LIGO.

#### Substrate Brownian noise

The substrate Brownian noise power spectral density scales with the beam spot size as  $1/w$ , and is proportional to the numerical values  $g_{0pl}$  which describe the effects of the different mode shape [Vin09]. Table 15 of [Vin09] shows the  $g_{0pl}$  values for modes up to LG<sub>55</sub><sup>1</sup>.

From the beam size scaling factors required to give equal clipping losses in table 2.2, and the substrate Brownian noise power spectral density scaling factors  $g_{0pl}$ , we calculate

---

<sup>1</sup>In [Vin09], the mode indices of higher-order LG modes are notated as  $n$  and  $m$ , as opposed to the notation of  $p$  and  $l$  used in this work. The  $p$  and  $l$  notation is preserved here to provide distinction from the HG mode set.

the substrate Brownian noise power spectral density improvement of  $\text{LG}_{pl}$  modes over the  $\text{LG}_{00}$  mode,  $\Theta_{pl}^{\text{SubBrown}}$ , as

$$\Theta_{pl}^{\text{SubBrown}} = \frac{a_{pl}}{g_{0pl}}. \quad (\text{A.1})$$

The results of for  $\Theta_{pl}^{\text{SubBrown}}$  are summarised in table A.1. From this table it is clear that higher-order LG modes have a substrate Brownian noise power spectral density advantage over the  $\text{LG}_{00}$  mode.

p	0	1	2	3	4	5
0	1.0000	1.3927	1.6102	1.7318	1.8417	1.8944
1	1.3183	1.5704	1.7231	1.8051	1.8940	1.9687
2	1.4906	1.6968	1.8339	1.9034	1.9619	1.9872
3	1.6088	1.7878	1.8706	1.9656	1.9760	2.0152
4	1.6690	1.8618	1.9222	1.9756	2.0714	2.0561
5	1.7143	1.9028	1.9877	2.0632	2.1045	2.1159

Table A.1.: Numerical values of the scaling factors between the substrate Brownian noise power spectral density for  $\text{LG}_{00}$  and  $\text{LG}_{pl}$  modes, where all modes are scaled to give 1 ppm clipping loss on a fixed mirror size.

### Substrate thermoelastic noise

The substrate thermoelastic noise power spectral density scales with the beam spot size as  $1/w^3$ , and is proportional to the numerical values  $g_{2pl}$  which describe the effects of the different mode shape. Table 18 of [Vin09] shows the  $g_{2pl}$  values for modes up to  $\text{LG}_{55}$ . From the beam size scaling factors required to give equal clipping losses in table 2.2, and the thermoelastic noise power spectral density scaling factors  $g_{2pl}$ , we calculate the substrate thermoelastic noise power spectral density improvement of  $\text{LG}_{pl}$  modes over the  $\text{LG}_{00}$  mode,  $\Theta_{pl}^{\text{SubTherm}}$ , as

$$\Theta_{pl}^{\text{SubTherm}} = \frac{a_{pl}^3}{g_{2pl}}. \quad (\text{A.2})$$

The results of for  $\Theta_{nm}^{\text{SubTherm}}$  are summarised in table A.2. From this table it is clear that some higher-order LG modes, including the  $\text{LG}_{33}$  mode have a small substrate

thermoelastic noise power spectral density disadvantage over the  $LG_{00}$  mode. In the context of second generation gravitational wave detectors this is not likely to be a large concern, since the substrate thermoelastic noise is already expected to be significantly lower than the coating Brownian noise.

m	0	1	2	3	4	5
0	1.0000	0.7780	0.6350	0.5405	0.4632	0.4133
1	1.7107	1.2412	0.9794	0.8316	0.7182	0.6203
2	1.8588	1.3424	1.0773	0.9178	0.7842	0.6891
3	1.8590	1.4065	1.1225	0.9426	0.8182	0.7322
4	1.8856	1.4212	1.1601	0.9914	0.8330	0.7639
5	1.8209	1.4066	1.1697	0.9640	0.8622	0.7791

Table A.2.: Numerical values of the scaling factors between the substrate thermoelastic noise power spectral density for  $LG_{00}$  and  $LG_{pl}$  modes, where all modes are scaled to give 1 ppm clipping loss on a fixed mirror size.

### Coating thermoelastic noise

According to [Vin10],[FRC<sup>+</sup>04] and [Lov06], the coating thermoelastic noise power spectral density scales in the exact same manner as the coating Brownian noise, and thus the coating thermoelastic noise power spectral density improvement factors for higher-order LG modes are exactly the same as those shown in table 2.3.

## A.2. Hermite-Gauss mode thermal noise scaling factors

### Coating Brownian noise

The coating Brownian noise improvement factors for higher-order HG modes over the  $HG_{00}$  for a 1 ppm clipping loss are shown in table 2.5.

### Substrate Brownian noise

The substrate Brownian noise power spectral density scales with the beam spot size as  $1/w$ , and is proportional to the numerical values  $g_{0nm}$  which describe the effects of the different mode shape. Table I of [Vin10] shows the  $g_{0nm}$  values for modes up to HG<sub>55</sub>. In the same way as for the LG modes, we calculate the substrate Brownian noise power spectral density improvement of HG<sub>*nm*</sub> modes over the HG<sub>00</sub> mode,  $\Theta_{nm}^{\text{SubBrown}}$ , as

$$\Theta_{nm}^{\text{SubBrown}} = \frac{a_{nm}}{g_{0nm}}. \quad (\text{A.3})$$

The results of for  $\Theta_{nm}^{\text{SubBrown}}$  are summarised in table A.3. From this table we can see that higher-order HG modes have a substrate Brownian noise power spectral density advantage over the HG<sub>00</sub> mode.

m	0	1	2	3	4	5
n						
0	1	1.165	1.232	1.268	1.288	1.300
1	1.165	1.364	1.450	1.496	1.524	1.539
2	1.232	1.450	1.550	1.605	1.638	1.656
3	1.268	1.496	1.605	1.667	1.706	1.729
4	1.288	1.524	1.638	1.706	1.749	1.779
5	1.300	1.539	1.656	1.729	1.779	1.808

Table A.3.: Numerical values of the scaling factors between the substrate Brownian noise power spectral density for HG<sub>00</sub> and HG<sub>*nm*</sub> modes, where all modes are scaled to give 1 ppm clipping loss on a fixed mirror size.

### Substrate thermoelastic noise

The substrate thermoelastic noise power spectral density scales with the beam spot size as  $1/w^3$ , and is proportional to the numerical values  $g_{2nm}$  which describe the effects of the different mode shape. Table III of [Vin10] shows the  $g_{2nm}$  values for modes up to HG<sub>55</sub>. We calculate the substrate thermoelastic noise power spectral density improvement of HG<sub>*nm*</sub> modes over the HG<sub>00</sub> mode,  $\Theta_{nm}^{\text{SubTherm}}$ , as

$$\Theta_{nm}^{\text{SubTherm}} = \frac{a_{nm}^3}{g_{2nm}}. \quad (\text{A.4})$$

The results of for  $\Theta_{nm}^{\text{SubTherm}}$  are summarised in table A.4. From this table it is clear that higher-order HG modes actually have a significant substrate thermoelastic noise power spectral density *disadvantage* over the HG<sub>00</sub> mode.

m	0	1	2	3	4	5
n						
0	1	0.831	0.688	0.583	0.503	0.441
1	0.831	0.776	0.685	0.602	0.535	0.478
2	0.688	0.685	0.629	0.570	0.517	0.470
3	0.583	0.602	0.570	0.528	0.487	0.449
4	0.503	0.535	0.517	0.487	0.454	0.425
5	0.441	0.478	0.470	0.449	0.425	0.399

Table A.4.: Numerical values of the scaling factors between the substrate thermoelastic noise power spectral density for HG<sub>00</sub> and HG<sub>nm</sub> modes, where all modes are scaled to give 1 ppm clipping loss on a fixed mirror size.

### Coating thermoelastic noise scaling factors

As was the case for LG modes, the coating thermoelastic noise power spectral density scales in the exact same manner as the coating Brownian noise. The coating thermoelastic noise power spectral density scaling factors are therefore exactly the same as those shown in table 2.5.



## Appendix B.

# Simulation code for results presented in chapter 3

### B.1. FINESSE input files for simulation study into the interferometric performance of the LG<sub>33</sub> mode

The FINESSE input file below is the master file for the simulations described in section 3.1. The basic optical layout is first described, including the input mode, phase modulations, mirror and cavity parameters and photodetectors. Next the numbered blocks of code can be used to plot the various aspects of the system that were investigated. By uncommenting each block in turn the plots shown in section 3.1 may be reproduced. Blocks are commented out using the syntax `/*` to begin the block comment, and `*/` to end the comment. Individual lines are commented out using the `#` key or `%`. See the [FINESSE web page](#) to download the FINESSE executable, source code, reference manual and examples.

```
# Input laser with power 1W at node n1
laser i1 1 0 n1

# Set FINESSE to use higher order modes up to order 13
maxtem 13

# Create LG33 mode using decomposition into Hermite-Gauss modes.
# See matlab script temsLG.m for the decompositions for other LG modes
```

```
tem i1 0 0 0 0
tem i1 9 0 0.164062 0
tem i1 8 1 0.164062 -90
tem i1 7 2 0 180
tem i1 6 3 0.125 -90
tem i1 5 4 0.046875 180
tem i1 4 5 0.046875 -90
tem i1 3 6 0.125 180
tem i1 2 7 0 0
tem i1 1 8 0.164062 180
tem i1 0 9 0.164062 90

# Add modulation sidebands
mod EOM1 $fEOM1 0.3 2 pm 0 n1 n2

# Define space before REFL beamsplitter
s lx1 $lx1 n2 nIMX1

# IMX - cavity input mirror in the X-arm
bs2 IMXAR $RIMXAR $LIMXAR $IMXARphi 0 nIMX1 nPOX1 nIMXi1 nPOX2
s sIMX $sIMX $nsilica nIMXi1 nIMXi2
m1 IMX $TIMX $LIMX $IMXphi nIMXi2 nIMX2
attr IMX Rc $RCIMX

# Intra-cavity space
s Lx $Lx nIMX2 nEMX1

# EMX cavity end mirror in the X-arm
m1 EMX $TEMX $LEMX $EMXphi nEMX1 nEMXi1
s sEMX $sEMX $nsilica nEMXi1 nEMXi2
m EMXAR $REMXAR $TEMXAR $EMXARphi nEMXi2 nXP1
attr EMX Rc $RCEMX

# Set cavity length to 3km
```

```
const Lx 3000

# Set length of space before REFL beamsplitter
const lx1 6.044

# optical path to quadrant photodetectors
s sPO2 0 $nsilica nPOX2 nPOX3
m mPO2 0 1 0 nPOX3 nPOX4
s sQr1 0 nPOX4 nQr1
bs bsQr .5 .5 0 0 nQr1 nQr2 nQr3 dump
s sQra 0 nQr2 nQra
s sQrb 0 nQr3 nQrb
attr sQr1 g 0
attr sQra g 90
attr sQrb g 0

# Substrates
#-----

const nsilica 1.44963
const sIMX 0.2
const sEMX 0.2

# Corresponding beam sizes
# Mirror      Beam size [cm]
# IMX         3.52
# MPR         3.55
# BS          3.53
#-----

const RCEMX 1910
const RCIMX -1910

### RC=1910 results in
#0: node nIMX2(7); IMX(0), Lx(6); n=1 (IMX --> nIMX2)
```

*Appendix B. Simulation code for results presented in chapter 3*

---

```
# x, y: w0=16.297262mm w=35.17543mm z=-1.5km z_R=784.21936m
# q=(-1500 + 784.219i) gamma=20.78151urad
# g_i-factor = -0.570680628272251309
# g = 0.32567637948521148
# one way Guoy phase = 0.963461860338102914
# mode spacing = 15323.36Hz
# Finesse = 1227
# FSR = 49.9kHz
# FWHM = 40.73Hz

# Transmission, Reflections, etc.
#-----
const TIMX    5m
const LIMX    50u

const TEMX    10u
const LEMX    50u

# AR Coatings
const RIMXAR  100u
const LIMXAR  50u
const REMXAR  0
const TEMXAR  1

# Tunings
#-----
const IMXphi  167.977016839274 # LG55 # pseudo locked with phase 0
const EMXphi  0

const IMXARphi  0
const EMXARphi  0

# Modulation frequencies
#-----
```

```
#const fEOM1 1.5M
const fEOM1 1k

# Demodulation phases
#-----
#const phi_d_EOM1 66.1      # for a modulation frequency of 15M
#const phi_d_EOM1 170.8 # for a modulation frequency of 1.5M
const phi_d_EOM1 182.25 # for 1kHz

# Error signal slope
#-----
const ESS -0.129376831754298956
const FbS 0.129376831754298956

# Arm x
cav armx IMX nIMX2 EMX nEMX1

phase 0

#####
# 1. Find operating point of the LG33 mode in the cavity
/*
pd cav_power nEMX1
showiterate 10
# pseudo lock for cavity
ad ph_m11 0 nIMXi2*
ad ph_m12 0 nIMX2
noplots ph_m11
noplots ph_m12
set ph1 ph_m11 deg
set ph2 ph_m12 deg
func cphase = $ph2-$ph1-90
noplots cphase
lock clock $cphase -1m .1m
```

```
noplot clock
func fb = $clock
#noplot fb
put EMX phi $clock
xaxis* IMX phi lin 0 90 10
*/

# IMX phi =167.977016839274
# power = 763.900517266
#####

#####

# 2. Plot cavity mode
/*
retrace off
beam ccd nXP1
xaxis ccd x lin -12 12 100
x2axis ccd y lin -12 12 100
#trace 8
*/
#####

#####

# 3. Plot transmitted power and error signal in reflection
#/*
#const theta-tilt 0.1u
#attr EMX xbeta $theta-tilt
#attr EMXAR xbeta $theta-tilt
pd power nXP1
pd1 error $fEOM1 $phi_d_EOM1 nIMXi2
xaxis IMX phi lin 157.977 177.977 400
#diff IMX phi
#x2axis EMX xbeta lin 0 1u 10
```

```
#put EMXAR xbeta $x1
#*/
# slope -7.691158828
#####

#####
# 4. Find error signal demodulation phase
/*
pd1 error $fEOM1 $phi_d_EOM1 nIMXi2
diff IMX phi
#xaxis error phi lin 0 180 90 # coarse search
xaxis error phi lin 182 183 4 # fine search
*/
# RESULT
# phi_d_EOM1 = 170.8 for 1.5M
# phi_d_EOM1 = 182.25 for 1k
#####

#####
# 5. lock cavity with error signal
/*
pd cav_power nEMX1
pd1 error $fEOM1 $phi_d_EOM1 nIMXi2
showiterate 10
noplots error
set LES error re
lock clock $LES $FbS .1m
noplots clock
func fb = $clock
put EMX phi $clock
xaxis IMX phi lin 167.977 177.977 10
*/
# Time needed 5m20s
```

```
#####
```

```
#####
```

```
# 6. introducing tilt
/*
const theta-tilt 1u
attr EMX xbeta $theta-tilt
attr EMXAR xbeta $theta-tilt
# look at error signal and transmitted power
pd power nXP1
pd1 error $fEOM1 $phi_d_EOM1 nIMXi2
xaxis IMX phi lin 156 180 2
*/
# RESULT
# longitudinal error signal position changes
#####
```

```
#####
```

```
# 7. cavity lock with longitudinal error signal while changing the tilt of EMX
/*
pd cav_power nEMX1
pd1 error $fEOM1 $phi_d_EOM1 nIMXi2
showiterate 10
noplots error
set LES error re
lock clock $LES -0.1 .1m
noplots clock
func fb = $clock
put EMX phi $clock
xaxis EMX xbeta lin 0 1u 100
put EMXAR xbeta $x1
#const theta-tilt 0
#attr EMX xbeta $theta-tilt
```

---

```

#attr EMXAR xbeta $theta-tilt
*/
# RESULT
# longitudinal error signal position changes
#####

#####

# 8. 2D plot tilt over cavity detuning no FB
/*
pd cav_power nEMX1
pd1 error $fEOM1 $phi_d_EOM1 nIMXi2
noplots error
#showiterate 10
#set LES error re
#lock clock $LES -0.1 .1m
#noplots clock
#func fb = $clock
#put EMX phi $clock
xaxis EMX xbeta lin 0 1u 100
put EMXAR xbeta $x1
#x2axis IMX phi lin 167.807016839274 168.507016839274 100 # 167.977016839274 168.5
x2axis IMX phi lin 167.477016839274 168.477016839274 100 # 167.977016839274 168.5
*/
# RESULT
# longitudinal error signal position changes
#####

#####

# 9. Plot alignment error signal
/*
# Quadrant diodes
#-----
#
const Qra_pphi1 0

```

```
const Qra_qphi1 90
const Qrb_pphi1 0
const Qrb_qphi1 90

pd1 Qrap $fEOM1 $Qra_pphi1 nQra
pdtype Qrap x-split
#pd1 Qraq $fEOM1 $Qra_qphi1 nQra
#pdtype Qraq x-split
#pd1 Qrbp $fEOM1 $Qrb_pphi1 nQrb
#pdtype Qrbp x-split
#pd1 Qrbq $fEOM1 $Qrb_qphi1 nQrb
#pdtype Qrbq x-split

#xaxis EMX xbeta lin -1u 1u 100
#func to = (-1)*$x1
#noplot to
#put IMX xbeta $to

### optimize demodulation phase of rotation error signal
### optimized phase Qra_pphi1 = 0
diff EMX xbeta
xaxis Qrap phi lin 0 180 100
*/
#####

#####
/*

yaxis abs

pd trans n5
#xaxis m1 phi lin 0 80 40
xaxis m1 xbeta lin 0 1u 40
*/
```

```
#####
```

```
# Read out time taken to execute simulation
time
```

## B.2. Matlab scripts for simulation study into LG<sub>33</sub> mode generation

This section includes two top level Matlab scripts for performing some of the simulations reported in section 3.2. The first script `LG33hx_gen_sim_paramfind.m` was used to produce figure 3.13, and the second script `optimum_beam_size_ratio_LG_upto_order9.m` was used to produce the values in table 3.3. Also included here are the functions used within these scripts, including the function `LGfield.m` and its dependencies, for producing helical LG<sub>pl</sub> mode complex amplitude matrices, and `LGhelixplate.m` for producing the helical LG<sub>pl</sub> mode phaseplate profiles.

```
%-----
% LG33hx_gen_sim_paramfind.m
%
% A script to simulate the conversion of a TEM00 beam into a LG33 helical
% beam for 10 different cases. In each case, the phaseplate is the same,
% and the TEM00 spot size at the phsaepate is the same. In each case the
% radius of curvature of the TEM00 beam at the phaseplate is different.
% This script calculates the theoretical value for beam parameters of the
% LG33 mode that is produced in each case. Using these parameters as
% initial guesses the script then performs a best fit, using the convolution
% between the phaseplate generated LG33 mode and an ideal LG33 mode as the
% figure of merit, to find the LG33 beam parameters which best match the
% phaseplate generated beam. The script writes the fitting results to a
% file called 'LG33hx_gen_fit_res.dat', and writes the theoretical values
% to a file called 'LG33hx_gen_ther_res.dat'. One would then compare the
% theoretical values to the fitted values and use the overlap as a figure
% of merit for the suitability of the theory.
%
```

```
% Requires the use of the following functions;
%
% LGfield.m
% LGhelixplate.m
% HGfield.m
% fit_LG_field.m
% FT_conv_fields.m
% propagate.m
%
% Paul Fulda, 17/08/09 pfulda@star.sr.bham.ac.uk
%
%-----

clear all;

%   Define the initial parameters:
%   - for the grid representing the phase plate
%   - for the initial TEM00 mode

tic
lambda=1064e-9; % Wavelength
%z0=0;    % Distance to beam waist
%D=1;    % Distance from TEM00 waist position to the phaseplate
L=0.5;   % Propagation distance from the phaseplate to 'camera' position
p=3;    % Define the radial mode number
l=3;    % Define the azimuthal mode number
plate_beamsize = 6e-4; % Define the image size of the phaseplate
TEM00_wpp=0.0023; % Define the TEM00 spotsize at the phaseplate

% Define the width/height of the simulation space
x_width =14.6e-3;
y_width =x_width;

% Calculate the x and y range
```

```
xrange=x_width/2;
yrange=y_width/2;

% Number of points in the grid, equivalent to number of pixels
xpoints=768;
ypoints=xpoints;

% Pixel sizes in x and y directions
dx=2*xrange/xpoints;
dy=2*yrange/ypoints;

% Vectors to address all x and y values
x=linspace(-xrange+dx/2,xrange-dx/2,xpoints);
y=linspace(-yrange+dy/2,yrange-dy/2,ypoints);

% Generate phaseplate and pixel scale vectors
[plate,x,y]=LGhelixplate(xpoints,ypoints,x_width,y_width,p,l,plate_beamsize);

ffit=fopen('LG33hx_gen_fit_res.dat','w');
for j=0:10

    % Produce the initial TEM00 mode at the phaseplate
    if j~=5
        % Set radius of curvature of input TEM00 at phaseplate
        RCTEM00=j-5;
        % Calculate TEM00 waist size
        TEM00w0=rcw2w0(RCTEM00,TEM00_wpp,lambda);
        % Calculate TEM00 waist position
        TEM00z0=rcw2z(RCTEM00,TEM00_wpp,lambda);
        % Generate TEM00 mode
        TEM00=HGfield(lambda,TEM00w0,TEM00w0,TEM00z0,TEM00z0,0,0,x,y);

        % Interact the TEM00 mode with the phase plate
        LG33lab=TEM00.*plate;
```

```
% Propagate the LG33lab beam to the camera position
LG33lab=propagate(LG33lab,L,1,lambda,2*xrange,2*yrange);

% Generate the LG33theory beam that theory predicts should
% have the same beam parameters as the LG33lab beam

% Calculate waist size of LGtheory beam
w0xtheory=rcw2w0(RCTEM00,plate_beamsize,lambda);
w0ytheory=w0xtheory;
% Calculate distance to waist of LGtheory beam
ztheory=rcw2z(RCTEM00,plate_beamsize,lambda);
paramsin(1)=w0xtheory;
paramsin(2)=ztheory;
paramsin(3)=1.0;
paramsin(4)=0.0;
[paramsout]=fit_LG_field(paramsin,lambda,L,p,l,x,y,LG33lab);
% Generate LG33 beam at camera position
LG33theory=paramsout(3)*exp(i*paramsout(4))*LGfield(lambda,...
    paramsout(1),paramsout(2)+L,p,l,x,y);

% Compute the inner product of LG33lab and LG33theory modes:

% Inner product of the theoretical and phaseplate LG33:
conv6=FT_conv_fields(LG33theory,LG33lab);
% Convert to a percentage:
percentage_2=((abs(conv6))^2)*100;

disp(sprintf('Fit results:'));
disp(sprintf('  started with w0=%g, z0=%g, factor=%g, phi=%g',...
    paramsin(1),paramsin(2),paramsin(3),paramsin(4)));
disp(sprintf('  ended with w0=%g, z0=%g, factor=%g, phi=%g',...
    paramsout(1),paramsout(2),paramsout(3),paramsout(4)));
disp(sprintf('  overlap %g %%',    percentage_2));
```

```

        fprintf(ffit,'%d, %d, %g, %g, %g, %g, %g\n',j,RCTEM00,paramsout(1),...
                paramsout(2),paramsout(3),paramsout(4),percentage_2);
    end
end
fclose(ffit);
toc

```

The script `optimum_beam_size_ratio_LG_upto_order9.m`, used to find the optimum beam size ratios for conversion to higher-order LG modes from a  $LG_{00}$  mode. The results of this script are shown in table 3.3 for  $LG_{pl}$  modes up to the order 9.

```

%-----
% optimum_beam_size_ratio_LG_upto_order9.m
%
% Script to find the mode purity upon conversion from LG00 mode to higher-
% order LG modes using a phaseplate, for different beam size ratios at the
% phaseplate. The optimum size ratio is calculated for each  $LG_{pl}$  mode, up to
% the maximum order specified.
%
% Requires the use of the following functions;
%
% LGfield.m
% LGhelixplate.m
% HGfield.m
% FT_conv_fields.m
% propagate.m
%
%-----

clear all

lambda=1064e-9; % wavelength
wTEM00=5e-3; % set beam spot size at phase plate
maxorder=9; %total number of different modes to try
% calculate total number of modes to be investigated from maxorder
for order=0:maxorder

```

```
totalnummodes=totalnummodes+floor(order/2)+1;
end
nmode=0; % initialise integer to count the successive modes
istep=0.2e-3; % difference between the waist sizes of successive input beamshapes
jmax=60; % number of different fudge factors per input beamshape
jstep=0.1; % step size between subsequent fudge factors
fudgevec=zeros(jmax,1); % initialise vector to store fudge factors
xsize=40e-3; % define xrange of simulation space
ysize=40e-3; % define yrange of simulation space
xelements=600; % number of x elements
yelements=600; % number of y elements
x=linspace(-xsize/2,xsize/2,xelements); % Define vector of x-positions
y=linspace(-ysize/2,ysize/2,yelements); % Define vector of y-positions
% Define size of phaseplate in pixels and physical lengths
platesize=[300,300,20e-3,20e-3];
nrun=1; % initialise nrun variable for progress update
no_of_runs=jmax*totalnummodes; % set total number of runs
ntime=0; % initialise another variable to 0
nave_time=0; % initialise average time to 0
convresults=zeros(totalnummodes,jmax); % Create empty array for storing results
powerratio=zeros(totalnummodes,jmax);

for s=1:jmax
    %pre-allocate fudge values to avoid 'loop growth' problem
    fudgevec(s,1)=3-jmax*jstep/2+(s-1)*jstep;
end
% create the TEM00 field at the phaseplate
TEM00=HGfield(lambda,wTEM00,wTEM00,0,0,0,0,x,y);
for l=0:maxorder
    p=0;
    while 2*p+l<=maxorder;
        nmode=nmode+1;
        for j=1:jmax % loop over 'jmax' different fudge factors
            nrun = nrun + 1; % set current number of runs
```

---

```

tic; % start timer
fudge=fudgevec(j); % set fudge factor for current loop
% calculate size of desired LGlp mode
% (TEM00 spot size divided by fudge factor)
wOLGlp=wTEM00/fudge;
% generate phaseplate array to produce desired LGlp mode
LGplate=LGHelixplate(platesize(1),platesize(2),platesize(3),...
platesize(4),p,l,wOLGlp);
% embed phaseplate in a null grid
LGplate=embedplate(LGplate,xelements,yelements);
LGgen=TEM00.*LGplate; % interact TEM00 field with phaseplate array
% Calculate theoretical Rayleigh range of generated LG mode
zRLGlp=pi*wOLGlp^2/lambda;
% Propagate generated LG mode over 2 Rayleigh lengths
LGgen=propagate(LGgen,2*zRLGlp,1,lambda,xsize,ysize);
%LGgen=LGgen/abs(max(max(LGgen))); % Normalise generated LG mode field
% Create theoretical LG mode with waist position 2 Rayleigh lengths
% further than the phaseplate position
LGideal=LGfield(lambda,wOLGlp,2*zRLGlp,p,l,x,y);
powerratio(nmode,j)=FT_power_in_field(LGgen,x,y)/...
FT_power_in_field(LGideal,x,y);
LGgen=LGgen/powerratio(nmode,j); % Normalise theoretical LG field
% Find convolution between the theoretical and
% phaseplate generated LG fields
convresults(nmode,j)=FT_conv_fields(LGideal,LGgen);
[maxconvresults(nmode),maxfudgeconv(nmode)]=max(convresults(nmode,:));
maxfudgeconv(nmode)=fudgevec(maxfudgeconv(nmode));
[maxpowerratio(nmode),maxfudgepower(nmode)]=max(powerratio(nmode,:));
maxfudgepower(nmode)=fudgevec(maxfudgepower(nmode));

ntime = toc; % readout timer
nave_time = nave_time + ntime;
ave_run_time = nave_time / nrun; % Calculate average loop time
% Calculate estimated remaining time

```

```
        estimated_time = (no_of_runs - nrun) * ave_run_time;
        display(sprintf('Run %g/%g',nrun,no_of_runs)); % display step counter
        % display remaining time for calculation
        display(sprintf('%2.0fh:%2.0fmin:%2.0fsec remaining',...
            fix(estimated_time/3600),fix(mod(estimated_time,3600)/60),...
            fix(mod(mod(estimated_time,3600),60))));
    end
    p=p+1;
end

end
```

The function LGfield.m, used to generate an ideal LG mode amplitude distribution:

```
%-----
% function field=LGfield(lambda,w0,z,p,l,x,y)
% (requires ulp.m)
%
% Matlab/Octave function to fill a 2D grip with complex field
% amplitudes for a Laguerre-Gauss beam.
%
% lambda (real):    wavelength [m]
% w0 (real):       beam radius
% z (real):        distance to beam waist [m]
% p,l (int):       mode indices of LG TEMp,l mode
%                  (p is the radial index)
% x,y (real):      position vectors defining the grid size [m]
%
% field (complex): 2D grid of field amplitudes
%
% Andreas Freise 25.03.2007
%-----

function [field,signflip]=LGfield(lambda,w0,z,p,l,x,y)
```

```

w=sqrt(w0^2+z*lambda/pi);

xpoints=length(x);
ypoints=length(y);

[X,Y] = meshgrid(x,y);
r = sqrt(X.^2+ Y.^2);
sr = sqrt(2)*r/w;
phi = atan2(Y,X);

for i=1:ypoints
    field(i,:)=ulp(lambda,w0,r(i,:),phi(i,:),z,p,l);
    signflip(i,:)=sign(LaguerrePol(p,abs(l),sr(i,:).^2));
end

return

```

The function `ulp.m`, required for `LGfield.m`.

```

% -----
% function field = ulp (lambda,w0, r, phi, z, p, l)
% (required LaguerrePoly.m)
%
% Octave/Matlab function to compute the field of a 2D Laguerre-Gauss
% function u_lp(x,y,z).
%
% lambda = wavelength
% w0 (real):  beam widths [m]
% r (real):   distance to optical axis [m]
% phi (real): position around optical axis [rad]
% z (real):   distance to waist [m]
% l (int):    order of mode (azimuthal index, p>=|l|>=0)
% p (int):    order of mode (radial index, p>=0)
%
% field (complex): field amplitude at (x,y,z)

```

```
%
% Andreas Freise 25.03.2007
% -----

function field = ulp (lambda,w0,r,phi,z,p,l)

    sl=1;
    l=abs(l);

    field=0;

    % changed 04/11/09: the limit |l|<=p is not a requirement
    %if ((l<0) || (p<1))
    % error('Error: p>=|l|>=0');
    % return;
    %end

    k=2*pi/lambda;
    zr=pi*w0^2/lambda;
    wz=w0*sqrt(1+(z/zr)^2);
    sr=sqrt(2)*r/wz;
    qz=z+i*zr;
    psi=atan(z/zr);

    t1=sqrt(2*factorial(p)/(pi*factorial(l+p)))/wz;
    t2=exp(i *(2*p+1+1)*psi);
    t3=sr.^l.*LaguerrePol(p,l,sr.^2);
    t4=exp(-i * k*r.^2./(2*qz)+i*sl*phi);

    field=t1*t2*t3.*t4;

    return
```

The function `LaguerrePol.m`, required for `ulp.m`.

---

```

% -----
% function [L] = LaguerrePol (p,l,x)
%
% Matlab/Octave function to compute the
% associated Laguerre Polynomial  $L_p^l(x)$ .
%
%
% 
$$L_p^l(x) = \sum_{j=0}^p \frac{p!}{j! (p-j)!} (-x)^j$$

%
% p,l (int)
% x (real)
%
% L (real)
%
% Andreas Freise 25.03.2007
%-----

```

```

function [L] = LaguerrePol (p,l,x)

L=0;
for j=0:p
    L=L+bincoeff(l+p,p-j)/factorial(j)*(-x).^j;
end
return

```

The function `LGhelixplate.m`, used to generate a phase profile for conversion from a  $LG_{00}$  mode to a  $LG_{pl}$  mode. The thinking behind the method used is described in section [3.2.2](#).

---

```

%-----
% function [plate,x,y]=LGhelixplate(nxpix,nypix,xsize,ysize,p,l,w)
% (requires LaguerrePol.m)
%
% Matlab function to fill a 2D grid with phase values between 0 and  $2\pi$ ,

```

```
% thus simulating a spatial light phase modulator. The grid is designed
% such as to provide an optimised phaseplate pattern to convert
% from a non-astigmatic TEM00 beam into any higher order LG beam with the
% azimuthal phase dependence 'exp(il*phi)' as opposed to 'cos(il*phi)'. The
% function automatically sets the phaseplate pattern to be optimised for
% equal beam sizes in x and y-directions. If you wish to use square pixels
% you should be careful that the ratios xsize:nxpix and ysize:nypix are
% equal.
%
% nxpix,nypix (int): Number of pixels along x and y-axes
% xsize,ysize (float): Physical size of phaseplate along x and y-axes
% p,l (int):          Mode indices of LG_pl mode to be generated
% w (real):          Spot size of the LG_pl mode to be generated at the
%                   phaseplate [m]
%
% plate (complex):    2D grid of complex numbers representing the phase
% x,y (real):        Vectors containing the x and y-positions of pixels
%
% Paul Fulda 25/05/09
%-----

function [plate,x,y]=LGhelixplate(nxpix,nypix,xsize,ysize,p,l,w)

x=linspace(-xsize/2,xsize/2,nxpix);    % Generate vector of pixel x positions
y=linspace(-ysize/2,ysize/2,nypix);    % Generate vector of pixel y positions

% Generate a blank phaseplate of the required size, and initialise matrices
% that will hold the scaled radial, and azimuthal coordinates for the grid
plate=ones(nypix,nxpix);
sr=zeros(nypix,nxpix)/w;
phi=zeros(nypix,nxpix);

for j=1:nypix
    % Calculate radial coordinates and scale to beam size
```

---

```

    sr(j,:)=sqrt(2)*sqrt(x.^2+y(j)^2)/w;
    % Calculate azimuthal coordinates of each pixel
    phi(j,:)=atan2(y(j),x);
end

% Introduce azimuthal phase dependence
for j=1:nypix
    plate(j,:)=plate(j,.*(1*phi(j,:)));
    plate(j,:)=exp(i*(plate(j,:)));
end

% Introduce radial phase discontinuities
for j=1:nypix
    plate(j,:)=plate(j,).*sign(LaguerrePol(p,l,sr(j,).^2));
end

return

```

The function `fit_LG_field.m`, used to fit an ideal LG mode amplitude distribution to any amplitude distribution.

```

%-----
% fit_LG_field.m
%
% A function to fit a theoretical LG mode amplitude distribution field1 to an
% input amplitude distribution field1.
% Returns the parameters of the best-fit mode.
%
% paramsin - vector containing in this order - beam waist size, waist position,
%           amplitude scaling factor, phase offset
% lambda   - wavelength
% L        - distance from origin on z-axis to the point at which the test is made
% p,l      - radial and azimuthal indices of the LG mode
% x,y      - position vectors defining the grid size
% field1   - input field whose parameters are to be determined

```

*Appendix B. Simulation code for results presented in chapter 3*

---

```
% paramsout - best fit beam parameters
%-----

function [paramsout]=fit_LG_field(paramsin,lambda,L,p,l,x,y,field1)

    options=optimset('Display','iter', 'TolX', 0.01, 'TolFun', 0.01, 'MaxIter', 1000);
    paramsout=fminsearch(@mytestf,paramsin,options,lambda,L,p,l,x,y,field1);

function [diff] = mytestf(params,lambda,L,p,l,x,y,field1)
    field2=params(3)*exp(i*params(4))*LGfield(lambda,params(1),params(2)+L,p,l,x,y);
    diff=1-abs(FT_conv_fields(field1,field2))^2;
```

The function FT\_conv\_fields.m, used to find the inner product between two amplitude distributions.

```
%
%-----
% function [c]=FT_conv_fields(field1, field2)
%
% A function for Matlab that computes the scalar product between two
% complex 2D data arrays (similar to a convolution)
%
% field1: 2D data grid of complex numbers
% field2: 2D data grid of complex numbers
%
% c: value computed as  $c = \text{int}(\text{field1} * \text{field2}) / (|\text{field1}|^2 * |\text{field2}|^2)$ 
%
%
% Andreas Freise 14.08.2009
%-----
%
% Description: Computes the scalar product between two complex 2D data arrays
% Keywords: scalar, dot, product, 2D, conv, fields

function [c]=FT_conv_fields(field1, field2)
```

```
c=sum(sum(field1.*conj(field2)));
cn=sum(sum((field1.*conj(field1))));
cn=cn*sum(sum((field2.*conj(field2))));
c=conj(c/sqrt(cn));
```

The function `propagate.m`, used to perform the FFT propagation of fields.

```
%-----
% function [out] = propagate(psi,dist, nr, lambda, sizex, sizey)
%
% Octave/Matlab function, propagates the field 'psi' over a
% distance 'dist' using an FFT propagation.
%
% psi (complex):      array of field amplitudes
% dist (real):        length [m]
% nr (real):          index of refraction
% lambda (real):      wavelength [m]
% sizex, sizey (real): size of grid in x and y direction [m]
%                    (e.g. with dx = distance between two grid
%                    points, and xpoints the number of
%                    points, xsize=xpoints*dx
%
% This code is based on the Fortran subroutine PROPAGATE by Roland
% Schilling, which again was based on code by Jean-Yves Vinet. You
% can read the theory in Jean-Yves's very good 'VIRGO book of physics'
% (available online at the VIRGO site as a pdf file).
%
% Andreas Freise 30.12.2006 adf@sr.bham.ac.uk
%-----

% Some additional notes:
%
% One needs to take care that the field amplitude is sufficiently
% small at the borders of the grid. Everything reaching the
```

```
% end of the grid will be reflected back in (aliasing effects).  
%  
% The phase change from one grid point to another must be less  
% than Pi in order to have a unique solution for the wavefront.  
% Curved, e.g. spherical, wavefronts show large phasechanges  
% away from the optical axis and thus can require a large number  
% of points.
```

```
function [psi] = propagate(psi,dist, nr, lambda, sizex, sizey)
```

```
    % phi can be used to apply an additional phase to the field,  
    % here set to zero for the time being  
    phi=0;
```

```
    [ny,nx]=size(psi);  
    if(rem(nx,2)|| rem(ny,2))  
        error('Grid length must be a multiple of 2')  
        return;  
    end
```

```
    % compute reduced distance  
    distr=dist/nr;
```

```
    % calculate propagator  
    hx=pi*lambda*distr/sizex^2;  
    hy=pi*lambda*distr/sizey^2;
```

```
    for k=1:nx/2+1  
        ppgx(k)=exp(i*mod(phi/2+hx*(k-1)^2,2*pi));  
    end  
    for k=nx/2+2:nx  
        ppgx(k)=ppgx(nx+2-k);  
    end  
    for k=1:ny/2+1
```

```
    ppgy(k)=exp(i*mod(phi/2+hy*(k-1)^2,2*pi));
end
for k=ny/2+2:ny
    ppgy(k)=ppgy(ny+2-k);
end

% do forward fft transformation
psi=fft2(psi);
% apply propagator
for k=1:nx
    psi(:,k)=ppgy(:).*ppgx(k).*psi(:,k);
end
% do backwards fft transformation
psi=ifft2(psi);

return;
```



## Bibliography

- [AAA<sup>+</sup>04] B. Abbott *et al.* Detector description and performance for the first coincidence observations between LIGO and GEO. *Nuclear Instruments and Methods in Physics Research Section A: Accelerators, Spectrometers, Detectors and Associated Equipment*, 517(1-3):154 – 179, 2004.
- [AAA<sup>+</sup>08] F. Acernese *et al.* Virgo status. *Classical and Quantum Gravity*, 25(18):184001 (9pp), 2008.
- [AAA<sup>+</sup>10] J. Abadie *et al.* Predictions for the rates of compact binary coalescences observable by ground-based gravitational-wave detectors. *Classical and Quantum Gravity*, 27(17):173001, 2010.
- [AAB<sup>+</sup>] R. Abbott *et al.* AdvLIGO interferometer sensing and control conceptual design. Technical Report LIGO-T070247, 2008.
- [AAS08] R. Adhikari, K. Arai, and A. Stochino. Precise measurements on longitudinal and transverse mode spacings of an optical cavity using an auxiliary laser. Technical Report LIGO-G080467-x0, 2008.
- [ABHK08] H. Armandula, G. Billingsley, G. Harry, and W. Kells. Advanced LIGO core optics components preliminary design. Technical report, LIGO-E080033, 2008.
- [ABSW92] L. Allen, M. W. Beijersbergen, R. J. C. Spreeuw, and J. P. Woerdman. Orbital angular momentum of light and the transformation of Laguerre-Gaussian laser modes. *Physical Review A*, 45:8185–8189, June 1992.
- [ADAP98] J. Arlt, K. Dholakia, L. Allen, and M. J. Padgett. The production of multiringed Laguerre-Gaussian modes by computer-generated holograms. *Journal of Modern Optics*, 45:1231–1237, June 1998.

- [AdL07] Advanced LIGO reference design. Technical Report LIGO-M060056, 2007.
- [AFK<sup>+</sup>11] B. Aylott *et al.* Estimating parameters of coalescing compact binaries with a detector network including LIGO Australia. *ArXiv e-prints*, June 2011.
- [AP29] J. A. Anderson and R. W. Porter. Ronchi’s Method of Optical Testing. *Astrophysical Journal*, 70:175, 1929.
- [Bar97] Andreas Barthel. Abstimmbares signal-recycling mit externer modulation. Master’s thesis, Universität Hannover, 1997.
- [BAvW93] M. W. Beijersbergen, L. Allen, H. E. L. O. van der Veen, and J. P. Woerdman. Astigmatic laser mode converters and transfer of orbital angular momentum. *Optics Communications*, 96:123–132, 1993.
- [Bay84] F. Bayer-Helms. Coupling coefficients of an incident wave and the modes of spherical optical resonator in the case of mismatching and misalignment. *Applied Optics*, 23:1369–1380, 1984.
- [BCKW94] M. W. Beijersbergen, R. P. C. Coerwinkel, M. Kristensen, and J. P. Woerdman. Helical-wavefront laser beams produced with a spiral phaseplate. *Optics Communications*, 112:321–327, 1994.
- [BFC<sup>+</sup>11] C. Bond, P. Fulda, L. Carbone, K. Kokeyama, and A. Freise. Higher order Laguerre-Gauss mode degeneracy in realistic, high finesse cavities. *Physical Review D*, 84(10):102002, 2011.
- [BGH<sup>+</sup>12] S. Ballmer, E. Gustafson, S. Hild, R. Adhikari, K. Arai. Report of the 3rd generation LIGO detector strawman workshop. Technical Report LIGO-T1200031-v3, 2012.
- [BHV98] F. Bondu, P. Hello, and J.-Y. Vinet. Thermal noise in mirrors of interferometric gravitational wave antennas. *Physics Letters A*, 246:227–236, 1998.
- [BK08] A.Ya. Bekshaev and A.I. Karamoch. Spatial characteristics of vortex light beams produced by diffraction gratings with embedded phase singularity. *Optics Communications*, 281(6):1366 – 1374, 2008.

- 
- [BM72] D. Bramanti and K. Maischberger. Construction and operation of a Weber-type gravitational-wave detector and of a divided-bar prototype. *Nuovo Cimento Lettere*, 4:1007–1013, 1972.
- [Boy80] Robert W. Boyd. Intuitive explanation of the phase anomaly of focused light beams. *J. Opt. Soc. Am.*, 70(7):877–880, 1980.
- [BV03] V. B. Braginsky and S. P. Vyatchanin. Thermodynamical fluctuations in optical mirror coatings. *Physics Letters A*, 312(3-4):244 – 255, 2003.
- [BW99] B. C. Barish and R. Weiss. LIGO and the detection of gravitational waves. *Physics Today*, 52:44–50, 1999.
- [CACD98] M. A. Clifford, J. Arlt, J. Courtial, and K. Dholakia. High-order Laguerre-Gaussian laser modes for studies of cold atoms. *Optics Communications*, 156:300–306, 1998.
- [Cav80] C. M. Caves. Quantum-mechanical radiation-pressure fluctuations in an interferometer. *Physical Review Letters*, 45:75–79, 1980.
- [Cav81] C.M. Caves. Quantum-mechanical noise in an interferometer. *Physical Review D*, 23:1693–1708, 1981.
- [CBB<sup>+</sup>12] A.V. Cumming *et al.* Design and development of the advanced LIGO monolithic fused silica suspension. *Classical and Quantum Gravity*, 29:035003, 2012.
- [Che07] Simon Chelkowski. *Squeezed Light and Laser Interferometric Gravitational Wave Detectors*. PhD thesis, University of Hannover, 2007.
- [CHF09] Simon Chelkowski, Stefan Hild and Andreas Freise. Prospects of higher-order Laguerre-Gauss modes in future gravitational wave detectors. *Physical Review D*, 79(12):122002, 2009.
- [CP99] J. Courtial and M. J. Padgett. Performance of a cylindrical lens mode converter for producing Laguerre-Gaussian laser modes. *Optics Communications*, 159:13–18, 1999.
- [CT02] C Cutler and K.S. Thorne. An overview of gravitational-wave sources. *arXiv:gr-qc/0204090v1*, 2002.

- [CW51] H. B. Callen and T. A. Welton. Irreversibility and generalized noise. *Physical Review*, 83:34–40, 1951.
- [DHK<sup>+</sup>83] R. W. P. Drever, J. L. Hall, F. V. Kowalski, J. Hough, G. M. Ford, A. J. Munley, and H. Ward. Laser phase and frequency stabilization using an optical resonator. *Applied Physics B: Lasers and Optics*, 31:97–105, 1983.
- [DK12] S.L. Danilishin and F.Ya. Khalili. Quantum measurement theory in gravitational-wave detectors. *Living Reviews in Relativity*, 15(5), 2012.
- [DOS<sup>+</sup>04] E. D’Ambrosio, R. O’Shaughnessy, S. Strigin, K. S. Thorne, and S. Vyatchanin. Reducing thermoelastic noise in gravitational-wave interferometers by flattening the light beams. *ArXiv General Relativity and Quantum Cosmology e-prints*, September 2004.
- [Dre96] R. W. P. Drever. Concepts for extending the ultimate sensitivity of interferometric gravitational wave detectors using non-transmissive optics with diffractive or holographic coupling. In *Proceedings of the Seventh Marcel Grossman Meeting on recent developments in theoretical and experimental general relativity, gravitation, and relativistic field theories*, pages 1401–+, 1996.
- [DZJB04] J. Degallaix, C. Zhao, L. Ju, and D. Blair. Thermal lensing compensation for AIGO high optical power test facility. *Classical and Quantum Gravity*, 21:903–+, 2004.
- [EBF<sup>+</sup>08] M. Evans, S. Ballmer, M. Fejer, P. Fritschel, G. Harry, and G. Ogin. Thermo-optic noise in coated mirrors for high-precision optical measurements. *Physical Review D*, 78(10):102003, 2008.
- [FBB<sup>+</sup>11] D. Friedrich *et al.* Waveguide grating mirror in a fully suspended 10 meter Fabry-Perot cavity. *Opt. Express*, 19(16):14955–14963, 2011.
- [FFG<sup>+</sup>05] R. Flaminio *et al.* Advanced virgo white paper. Technical Report VIR-NOT-DIR-1390-304, Virgo, 2005.
- [FHL<sup>+</sup>04] A. Freise, G. Heinzl, H. Lück, R. Schilling, B. Willke, and K. Danzmann. Frequency-domain interferometer simulation with higher-order spatial modes. *Classical and Quantum Gravity*, 21(5):S1067–S1074, 2004.

- 
- [Fin96] L.S. Finn. Binary inspiral, gravitational radiation, and cosmology. *Physical Review D*, 53(6):2878–2894, 1996.
- [FKCF10] P. Fulda, K. Kokeyama, S. Chelkowski, and A. Freise. Experimental demonstration of higher-order Laguerre-Gauss mode interferometry. *Physical Review D*, 82(1):012002, 2010.
- [FM06] A. Freise and M. Mantovani. Initial set of optical parameters for numerical simulations towards advanced VIRGO. Technical Report VIR-NOT-EGO-1390-330, Virgo, 2006.
- [FRC<sup>+</sup>04] M. M. Fejer *et al.* Thermoelastic dissipation in inhomogeneous media: loss measurements and displacement noise in coated test masses for interferometric gravitational wave detectors. *Physical Review D*, 70(8):082003, 2004.
- [FS10] A. Freise and K. Strain. Interferometer techniques for gravitational-wave detection. *Living Reviews in Relativity*, 13:1–+, 2010.
- [GBB<sup>+</sup>10] S. Goßler *et al.* The AEI 10 m prototype interferometer. *Classical and Quantum Gravity*, 27(8):084023–+, 2010.
- [GCF<sup>+</sup>03] S. Goßler *et al.* Mode-cleaning and injection optics of the gravitational-wave detector GEO600. *Review of Scientific Instruments*, 74:3787–3795, 2003.
- [GLSC08] Hartmut Grote *et al* for the LIGO Scientific Collaboration. The status of GEO 600. *Classical and Quantum Gravity*, 25(11):114043 (9pp), 2008.
- [GMSV10] A. Genin, J. Marque, B. Swinkels, and G. Vajente. Virgo input mode cleaner: Optical characterization. Technical Report VIR-0232A-10, Virgo, 2010.
- [Goß04] Stefan Goßler. The suspension systems of the interferometric gravitational-wave detector GEO600. PhD thesis, Universität Hannover, 2004.
- [GR95] A. Gillespie and F. Raab. Thermally excited vibrations of the mirrors of laser interferometer gravitational-wave detectors. *Phys. Rev. D*, 52:577–585, 1995.

- [GWINC] <http://lhocds.ligo-wa.caltech.edu:8000/advligo/GWINC>.
- [HAA<sup>+</sup>11] S Hild *et al.* Sensitivity studies for third-generation gravitational wave observatories. *Classical and Quantum Gravity*, 28(9):094013, 2011.
- [HABT<sup>+</sup>07] G. Harry *et al.* Titania-doped tantala/silica coatings for gravitational-wave detection. *Classical and Quantum Gravity*, 24(2):405–415, 2007.
- [HCC<sup>+</sup>03] J. Harms, Y. Chen, S. Chelkowski, A. Franzen, H. Vahlbruch, K. Danzmann, and R. Schnabel. Squeezed-input, optical-spring, signal-recycled gravitational-wave detectors. *Physical Review D*, 68(4):042001–+, 2003.
- [HCF<sup>+</sup>09] J. Hallam *et al.* Coupling of lateral grating displacement to the output ports of a diffractive Fabry-Perot cavity. *Journal of Optics A: Pure and Applied Optics*, 11(8):085502–+, 2009.
- [Hei99] Gerhard Heinzel. Advanced optical techniques for laser-interferometric gravitational-wave detectors. PhD thesis, MPI für Quantenoptik, 1999.
- [HF07] S. Hild and A. Freise. A novel concept for increasing the peak sensitivity of LIGO by detuning the arm cavities. *Classical and Quantum Gravity*, 24:5453–5460, 2007.
- [HFHRD95] H. He, M. E. J. Friese, N. R. Heckenberg, and H. Rubinsztein-Dunlop. Direct observation of transfer of angular momentum to absorptive particles from a laser beam with a phase singularity. *Physical Review Letters*, 75(5):826–829, 1995.
- [HGD<sup>+</sup>09] S. Hild *et al.* DC-readout of a signal-recycled gravitational wave detector. *Classical and Quantum Gravity*, 26(5):055012 (10pp), 2009.
- [Hil06] S. Hild *et al* for the LIGO Scientific Collaboration. The status of GEO 600. *Classical and Quantum Gravity*, 23(19):S643–S651, 2006.
- [HMY<sup>+</sup>11] T. Hong, J. Miller, H. Yamamoto, Y. Chen, and R. Adhikari. Effects of mirror aberrations on Laguerre-Gaussian beams in interferometric gravitational-wave detectors. *Physical Review D*, 84:102001, 2011.
- [HT75] R. A. Hulse and J. H. Taylor. Discovery of a pulsar in a binary system. *Astrophysical Journal Letters*, 195:L51–L53, 1975.

- 
- [HLSC10] G. Harry and the LIGO Scientific Collaboration. Advanced LIGO: the next generation of gravitational wave detectors. *Classical and Quantum Gravity*, 27(8):084006, 2010.
- [IWM10] I.W. Martin, *et al.* Effect of heat treatment on mechanical dissipation in Ta<sub>2</sub>O<sub>5</sub> coatings. *Class. Quantum Grav.*, 27:225020, 2010.
- [JT08] L. Janicijevic and S. Topuzoski. Fresnel and Fraunhofer diffraction of a Gaussian laser beam by fork-shaped gratings. *Journal of the Optical Society of America A*, 25(11):2659–2669, 2008.
- [Kha05] F.Ya. Khalili. Reducing the mirrors coating noise in laser gravitational-wave antennae by means of double mirrors. *Physics Letters A*, 334(1):67–72, 2005.
- [KKF<sup>+</sup>95] K. Kuroda and members of TAMA group. TAMA. In F. Ronga E. Coccia, G. Pizella, editor, *First Edoardo Amaldi Conference on Gravitational Wave Experiments*, pages 100–111. World Scientific, 1995.
- [KST<sup>+</sup>02] S. A. Kennedy, M. J. Szabo, H. Teslow, J. Z. Porterfield, and E. R. Abraham. Creation of Laguerre-Gaussian laser modes using diffractive optics. *Physical Review A*, 66(4):043801–+, 2002.
- [KSWD07] P. Kwee, F. Seifert, B. Willke, and K. Danzmann. Laser beam quality and pointing measurement with an optical resonator. *Review of Scientific Instruments*, 78:073103, 2007.
- [KLC06] K.Kuroda and the LCGT Collaboration. The status of LCGT. *Classical and Quantum Gravity*, 23(8):S215–S221, 2006.
- [KVL<sup>+</sup>11] A. Khalaidovski *et al.* Status of the GEO 600 squeezed-light laser. *ArXiv e-prints*, 2011.
- [Lev98] Y. Levin. Internal thermal noise in the LIGO test masses: A direct approach. *Physical Review D*, 57:659–663, 1998.
- [Lov06] G. Lovelace. The dependence of test-mass thermal noises on beam shape in gravitational-wave interferometers. *ArXiv General Relativity and Quantum Cosmology e-prints*, 2006.

- [LT00] Y.T. Liu and K.S. Thorne. Thermoelastic noise and homogeneous thermal noise in finite sized gravitational-wave test masses. *Physical Review D*, 62(12):122002, 2000.
- [LZF<sup>+</sup>02] R. Lawrence, M. Zucker, P. Fritschel, P. Marfuta, and D. Shoemaker. Adaptive thermal compensation of test masses in advanced LIGO. *Classical and Quantum Gravity*, 19:1803–1812, 2002.
- [MAI<sup>+</sup>08] N. Matsumoto, T. Ando, T. Inoue, Y. Ohtake, N. Fukuchi, and T. Hara. Generation of high-quality higher-order Laguerre-Gaussian beams using liquid-crystal-on-silicon spatial light modulators. *Journal of the Optical Society of America A*, 25:1642–+, 2008.
- [MCJV97] E. Martín-Badosa, A. Carnicer, I. Juvells, and S. Vallmitjana. Complex modulation characterization of liquid crystal devices by interferometric data correlation. *Measurement Science and Technology*, 8:764–772, 1997.
- [MDP<sup>+</sup>09] I. Moreno, J. A. Davis, B. M. Pascoguin, M. J. Mitry, and D. M. Cottrell. Vortex sensing diffraction gratings. *Optics Letters*, 34:2927, 2009.
- [MF08] M. Mantovani and A. Freise. Evaluating mirror alignment systems using the optical sensing matrix. *Journal of Physics Conference Series*, 122(1):012026–+, 2008.
- [MM87] A. A. Michelson and E. W. Morley. On the relative motion of the earth and the luminiferous ether. *American Journal of Science (3rd series)*, 34:333–345, 1887.
- [MRWM94a] E. Morrison, D. I. Robertson, H. Ward, and B. J. Meers. Automatic alignment of optical interferometers. *Applied Optics*, 33:5041–5049, 1994.
- [MRWM94b] E. Morrison, D. I. Robertson, H. Ward, and B. J. Meers. Experimental demonstration of an automatic alignment system for optical interferometers. *Applied Optics*, 33:5037–5040, 1994.
- [MTV06] B. Mours, E. Tournefier, and J.-Y. Vinet. Thermal noise reduction in interferometric gravitational wave antennas: using high order TEM modes. *Classical and Quantum Gravity*, 23:5777–5784, 2006.

- 
- [MTW73] C.W. Misner, K.S. Thorne, and J.A. Wheeler. *Gravitation*. W.H. Freeman and comp., 1973.
- [OKS06] S. Osten, S. Krueger, and A. Steinhoff. Spatial light modulators based on reflective micro-displays. *Technisches Messen*, 73, 2006.
- [RHC05] S. Rowan, J. Hough, and D.R.M. Crooks. Thermal noise and material issues for gravitational wave detectors. *Physics Letters A*, 347(1-3):25 – 32, 2005. Einstein Special Issue - Special Issue in celebration of this year’s World of Physics and the centenary of Einstein’s annus mirabilis.
- [RSS<sup>+</sup>81] A. Rüdiger, R. Schilling, L. Schnupp, W. Winkler, H. Billing, and K. Maischberger. A mode selector to suppress fluctuations in laser beam geometry. *Optica Acta*, 28:641–658, 1981.
- [Sau84] P. R. Saulson. Terrestrial gravitational noise on a gravitational wave antenna. *Physical Review D*, 30(4):732–736, 1984.
- [Sau94] P. R. Saulson. *Fundamentals of Interferometric Gravitational Wave Detectors*. World Scientific, 1994.
- [Sch] C. Schild. *Private communication*.
- [SKC11] K. Somiya for the KAGRA Collaboration. Detector configuration of KAGRA - the Japanese cryogenic gravitational-wave detector. *ArXiv e-prints*, 2011.
- [Sie86] A.E. Siegman. *Lasers*. University Science Books, 1986. See also: Errata List for LASERS, [http://www.stanford.edu/~siegman/lasers\\_book\\_errata.pdf](http://www.stanford.edu/~siegman/lasers_book_errata.pdf).
- [Ske05] T. Skettrup. Rectangular laser resonators with astigmatic compensation. *Journal of Optics A: Pure and Applied Optics*, 7(11):645–654, 2005.
- [SM04] R. Sisto and A. Moleti. On the sensitivity of gravitational wave resonant bar detectors. *International Journal of Modern Physics D*, 13:625–639, 2004.
- [SS06] J. A. Sidles and D. Sigg. Optical torques in suspended Fabry Perot interferometers. *Physics Letters A*, 354:167–172, 2006.

- [TRS<sup>+</sup>96] G. A. Turnbull, D. A. Robertson, G. M. Smith, L. Allen, and M. J. Padgett. The generation of free-space Laguerre-Gaussian modes at millimetre-wave frequencies by use of a spiral phaseplate. *Optics Communications*, 127:183–188, 1996.
- [Ueh97] N. Uehara. Ring mode cleaner for the initial LIGO 10 watt laser - internal report. See also UeharaSPIE, 1997.
- [Vin09] J. Y. Vinet. On special optical modes and thermal issues in advanced gravitational wave interferometric detectors. *Living Reviews in Relativity*, 12(5), 2009.
- [Vin10] J. Y. Vinet. Thermal noise in advanced gravitational wave interferometric antennas: A comparison between arbitrary order Hermite and Laguerre-Gaussian modes. *Physical Review D*, 82:042003, 2010.
- [VVC01] J. Y. Vinet and the Virgo Collaboration. *The Virgo Book of Physics: Optics and Related Topics*. Virgo, 2001.
- [WAA<sup>+</sup>04] B. Willke *et al.* Status of GEO 600. *Classical and Quantum Gravity*, 21(5):S417–S423, 2004.
- [WAA<sup>+</sup>06] B. Willke, *et al.* The GEO-HF project. *Classical and Quantum Gravity*, 23(8):S207–S214, 2006.
- [WPK<sup>+</sup>11] L. Winkelmann *et al.* Injection-locked single-frequency laser with an output power of 220 W. *Applied Physics B: Lasers and Optics*, 102:529–538, 2011.
- [YUM<sup>+</sup>08] K. Yamamoto *et al.* Current status of the CLIO project. *Journal of Physics: Conference Series*, 122:012002 (8pp), 2008.
- [ZM97] T. Zwerger and E. Mueller. Dynamics and gravitational wave signature of axisymmetric rotational core collapse. *A&A*, 320:209–227, 1997.

## Acknowledgments

First of all I would like to extend my gratitude towards my supervisor Andreas Freise for all his help throughout my PhD, and for always giving good advice and encouragement. I would also like to thank Andreas for supporting me and finding funds to get me to conferences and meetings, and for giving me so many good opportunities to present my work. I wish Andreas and all the Birmingham group the best success in the future, and I hope they continue to proliferate the good atmosphere and fun attitude that I found so enjoyable during my time there.

Thanks are of course due to all my colleagues at Birmingham with whom I have had the pleasure of working. I can't avoid a special mention to Simon Chelkowski, for giving me a shining example of how to approach lab work; I wish I had had more time to learn from him. A special mention of course also goes to Keiko Kokeyama for making the lab work fun, and for her unwavering support in the latter stages of my PhD even from all the way across the Atlantic.

Thank you to all the people in the Glasgow interferometry group, for making me feel welcome there and for letting me bring LG modes to the JIF lab. Special thanks to Stefan Hild for his kind hospitality in letting me stay at his flat while working on the experiment, and also for always sparing the time to teach me things while he was still in Birmingham. Thanks to Bryan for always being up for a whisky and curry, and for introducing me to the wondrous curiosity that is haggis pakora. Thanks also to Miles Padgett, John Nelson and the optics group at Glasgow for helping us out with the LabView software.

My time at Birmingham was made all the more fun by all the great friends there, so thank you to Mark 'Burke-Hole' Burke, Rory 'Beyond' Smith, Charlotte 'Just one Glass' Bond, Old Ben, New Ben, Daniel 'Not Dan Brown' Brown and Billy 'Hands of Doom' Clough. Thanks also to Sonic Sam and Lord Thrashbey of Deceptor, and Atom, Squash and the Klemponaut of Mutant, for providing the perfect foil to my scientific pursuits throughout my PhD. Many excellent times were had, and are still to be had in the future no doubt.

Finally, a huge thanks to my family for all their support and encouragement over the years. It goes without saying that I couldn't have done it without you, but I've gone and said it now anyway. This one is for you.

If you haven't already done so, try your skill at [Space Time Quest](#) and see if you can make it onto the [high-score hall of fame!](#)

I would like to leave those of you who have made it this far with this stirring thought, paraphrased from the most memorable 2nd year undergraduate physics essay I have ever marked:

*Science is neither good nor bad. It is like a hypodermic needle;  
it can be used to inject life saving medicine. Or heroin.*